UNIVERSIDADE DE SÃO PAULO
FACULDADE DE FILOSOFIA, CIÊNCIAS E LETRAS DE RIBEIRÃO PRETO
PROGRAMA DE PÓS-GRADUAÇÃO EM FÍSICA APLICADA À MEDICINA E BIOLOGIA

“Computational study of thalamocortical interactions: simulating oscillatory activity”.
“Estudo computacional de interações talamocorticais: simulando atividade oscilatória”

Renan Oliveira Shimoura

Tese apresentada à Faculdade de Filosofia, Ciências e Letras de Ribeirão Preto da Universidade de São Paulo, como parte das exigências para obtenção do título de Doutor em Ciências, obtido no Programa de Pós-Graduação em Física Aplicada à Medicina e Biologia.

Ribeirão Preto - SP

(2021)

UNIVERSIDADE DE SÃO PAULO
FACULDADE DE FILOSOFIA, CIÊNCIAS E LETRAS DE RIBEIRÃO PRETO
PROGRAMA DE PÓS-GRADUAÇÃO EM FÍSICA APLICADA À MEDICINA E BIOLOGIA

“Computational study of thalamocortical interactions: simulating oscillatory activity”.
“Estudo computacional de interações talamocorticais: simulando atividade oscilatória”

Renan Oliveira Shimoura

Tese apresentada à Faculdade de Filosofia, Ciências e Letras de Ribeirão Preto da Universidade de São Paulo, como parte das exigências para obtenção do título de Doutor em Ciências, obtido no Programa de Pós-Graduação em Física Aplicada à Medicina e Biologia.

Orientador: Prof. Dr. Antônio Carlos Roque da Silva Filho

Versão corrigida
Versão original disponível na FFCLRP

Ribeirão Preto - SP

(2021)

FICHA CATALOGRÁFICA

Shimoura, Renan Oliveira

Estudo computacional de interações talamocorticais: simulando atividade oscilatória / Renan Oliveira Shimoura; orientador Antônio Carlos Roque da Silva Filho. Ribeirão Preto - SP, 2021.

159 f.:il.

Tese (Doutorado - Programa de Pós-graduação em Física aplicada à Medicina e Biologia) - Faculdade de Filosofia, Ciências e Letras de Ribeirão Preto da Universidade de São Paulo, 2021.

1. Modelo integra-e-dispara. 2. Oscilações talamocorticais. 3. Cortéx visual primário. 4. Neuro-simuladores. 5. Oscilação alfa.

Nome: SHIMOURA, Renan Oliveira
Título: Estudo computacional de interações talamocorticais: simulando atividade oscilatória

Tese apresentada à Faculdade de Filosofia, Ciências e Letras de Ribeirão Preto da Universidade de São Paulo, como parte das exigências para a obtenção do título de Doutor em Ciências.

Aprovado em:____/____/____.

Banca Examinadora

Prof(a). Dr(a). :________________________ Instituição:__________
Julgamento: ________________________ Assinatura:__________

Prof(a). Dr(a). :________________________ Instituição:__________
Julgamento: ________________________ Assinatura:__________

Prof(a). Dr(a). :________________________ Instituição:__________
Julgamento: ________________________ Assinatura:__________

Prof(a). Dr(a). :________________________ Instituição:__________
Julgamento: ________________________ Assinatura:__________

Prof(a). Dr(a). :________________________ Instituição:__________
Julgamento: ________________________ Assinatura:__________

Dedico ao meu pai Tsuguio Shimoura que sempre deu todo suporte e apoio. Foi um pai excepcional e partiu meses antes da finalização desse trabalho. Espero continuar sendo motivo de seu orgulho.

Agradecimentos

Primeiramente à minha família que sempre me apoiou em minhas conquistas e dificuldades. Aos meus pais Maria Emília e Tsuguio Shimoura pela educação e encourajamento sempre presentes. Ambos sempre orgulhosos de qualquer conquista que adquiri até o momento. Infelizmente meu pai não estará presente para a finalização de mais essa etapa de minha vida, que ele esteja descansando em paz.

À minha irmã Suélen e cunhado Elton, por todo apoio e suporte. Aos meus tios e padrinhos Silvia e Hélio que sempre mantiveram o incentivo e a confiança em mim. A minha tia Gláucia, primos e primas, e também aos meus avós Maria Rosa e José. Todos importantíssimos em minha vida. Também à Letícia, minha companheira, que me suportou e me deu apoio na reta final desse trabalho.

Aos meus amigos(as) espalhados pelo Brasil e pelo mundo, sejam eles(as) amigos(as) adquiridos(as) na infância, no ensino médio, na faculdade, no laboratório e nos eventos acadêmicos, ou pelas situações da vida. Sem citar nomes, agradeço a todos, quem ler saberá que está incluído. Já peço desculpas de antemão, mas sou péssimo em listar esse tipo de coisa e para evitar esquecer alguém, prefiro manter assim. Apenas saibam que foram importantíssimos para a conclusão desse trabalho, seja pela ajuda acadêmica ou pelas distrações que me mantiveram mentalmente saudável dentro do possível.

Ao meu orientador, Prof. Dr. Antônio Carlos Roque por todo apoio e orientação dados nesses últimos anos. Agradeço também pela confiança, respeito e, principalmente, pelo incentivo sempre presente nas apresentações/participações em diferentes congressos, cursos e workshops, experiência essa da qual foi grande valia para meu desenvolvimento como pesquisador.

To the Institute of Neuroscience and Medicine - Computational and Systems Neuroscience (INM-6 / IAS-6) from Forschungszentrum Jülich where I did my internship in Germany. My thanks to all people from the institute, specially to my supervisors Prof. Dr. Markus Diesmann and Dr. Sacha J. van Albada for the guidance, encouragement, patience and kindness which they received me.

À **FAPESP (Fundação de Amparo à Pesquisa do Estado de São Paulo)** pelo financiamento de minha pesquisa de Doutorado no país (bolsa de doutorado, **processo nº 2017/07688-9**; e **Bolsa Estágio de Pesquisa no Exterior (BEPE), processo nº 2018/08556-1**).

Ao Departamente de Física e ao Programa de Pós-graduação em Física Aplicada à Medicina e Biologia (FAMB) ambos da Faculdade de Filosofia, Ciências e Letras de Ribeirão Preto.

Esta tese foi produzida como parte das atividades do **Centro de Pesquisa, Inovação e Difusão em Neuromatemática (CEPID NeuroMat), FAPESP 2013/07699-0**.

O presente trabalho foi realizado com apoio da **Coordenação de Aperfeiçoamento de Pessoal de Nível Superior – Brasil (CAPES) – Código de Financiamento 001**.

Resumo

SHIMOURA, R. O. **Estudo computacional de interações talamocorticais: simulando atividade oscilatória**. 2021. 159 f. Tese (Doutorado - Programa de Pós-graduação em Física aplicada à Medicina e Biologia) - Faculdade de Filosofia, Ciências e Letras de Ribeirão Preto, Universidade de São Paulo, Ribeirão Preto - SP, 2021.

O cérebro exibe vários ritmos oscilatórios que estão relacionadas a uma ou várias funções cognitivas. Uma das características mais proeminentes nos eletroencefalogramas em estado vigília de uma variedade de mamíferos, observada principalmente durante repouso com os olhos fechados, é o ritmo alfa ($\sim$ 10 Hz). Embora alfa seja fortemente associado à redução da atenção visual, também está relacionado a outros aspectos funcionais. Entender como e onde esse ritmo é gerado pode elucidar suas funções. Ainda hoje não há uma resposta definitiva para essa pergunta, embora várias hipóteses apresentem o tálamo e o córtex como possíveis protagonistas. Este trabalho objetiva explorar possíveis geradores alfa em um modelo do microcircuito multicamadas do córtex visual primário conectado a uma rede talâmica. A atividade espontânea do microcircuito cortical foi analisada e duas hipóteses de geração de alfa foram estudadas. Mostramos que as oscilações alfa emergem ao adicionar neurônios que disparam intrinsecamente em rajada na camada cortical 5 e ao alterar o atraso tálamo-cortical. As hipóteses apontam para geradores de diferentes origens, um apontando as camadas 5 e 2/3 e o outro apontando as camadas 4 e 6, e elas são comparáveis com trabalhos experimentais.

Palavras-chave: 1. Modelo integra-e-dispara. 2. Oscilações talamocorticais. 3. Cortéx visual primário. 4. Neuro-simuladores. 5. Oscilação alfa.

Abstract

SHIMOURA, R. O. **Computational study of thalamocortical interactions: simulating oscillatory activity**. 2021. 159 f. Thesis (Ph.D. - Postgraduate program in Physics applied to Medicine and Biology) - Faculty of Philosophy, Sciences and Literature, University of São Paulo, Ribeirão Preto - SP, 2021.

The brain displays various oscillatory rhythms across scales that are related to one or multiple cognitive functions. One of the most prominent features in waking electroencephalograms of a variety of mammals, mainly observed at rest with eyes-closed, is the alpha rhythm ($\sim$ 10 Hz). Although alpha is strongly associated with reduced visual attention, it is also related to other roles. Understanding how and where this rhythm is generated can elucidate its functions. Even today there is no definitive answer to this question, though several hypotheses put forward the thalamus and the cortex as possible protagonists. This work aims to explore possible alpha generators in a multilayered microcircuit model of the primary visual cortex connected to a thalamic network. The spontaneous activity of the cortical microcircuit was analyzed and two hypotheses of the generation of alpha were studied. We showed that alpha oscillations emerge by adding intrinsically bursting neurons at cortical layer 5 and by changing the thalamocortical loop delay. These hypotheses pointed to generators from different sources, one pointing layers 5 and 2/3 and the other pointing layers 4 and 6, and they are comparable with experimental works.

Key-words: 1. Integrate-and-fire model. 2. Thalamocortical oscillations. 3. Primary visual cortex. 4. Neuro-simulators. 5. Alpha oscillation.

List of Figures

List of Tables

List of Abbreviations

AdEx	Adaptive Exponential integrate-and-fire. xi, xiv–xvi, xx, xxi, 40, 47–49, 56, 60–63, 67, 68
cGC	Conditional Granger Causality. xvii–xix, 71–74, 78, 80, 83, 88, 90
DTI	Diffusion Tensor Imaging. 20
DWI	Diffusion Weighted Imaging. 20
EEG	Electroencephalogram. 1, 2
EPSP	Excitatory postsynaptic potential. ix, 26
FS	Fast Spiking. xi, xx, 48, 56, 92
GC	Granger Causality. xvi–xix, 70–72, 74, 78–80, 83, 84, 88, 90

IB	Intrinsically Bursting. xvi, xvii, xix, xxi, 2, 3, 9, 10, 67–69, 75–80, 87–89, 93, 94
IF	Integrate-and-Fire. 21

LGN	Lateral Geniculate Nucleus. xi, xii, 8–12, 42, 45, 49, 67, 75

MRI	Magnetic Resonance Imaging. 20

RS	Regular Spiking. xi, xvi, xvii, xx, 9, 10, 12, 48, 56, 60, 61, 75–77, 92

SFA	Spike Frequency Adaptation. 46, 60
STD	Short Term Depression. ix, 26
STDP	Spike Timing Dependent Plasticity. ix, 24–26
STF	Short Term Facilitation. ix, 26

V1	Primary Visual Cortex. xi, xiv, xx, 2, 8–10, 42–44, 56, 61, 67, 75

List of Symbols

C_m Membrane capacitance. 22, 46, 47

E_L Leak reversal potential. 46, 47

E_i Reversal membrane potential of the i_{th} ion. 22

E_{ij}^{syn} Reversal potential of the synaptic current from presynatic neuron j to neuron i. 23

$G_{ij}(t)$ Time-dependent synaptic conductance from presynatic neuron j to neuron i. 23, 24

I_i Ionic current of the i_{th} ion. 22

I_{ext} External current. 47

$I_{ij}^{\mathrm{syn}}(t)$ Electric current generated from presynatic neuron j to neuron i. 23

I_s Synaptic current. 47

I Injected current. 21

$J^{\max}$ Maximum value of synaptic efficacy. 25

$J_{ij}(t)$ Amplitude of the postsynaptic current. 24, 47

R Membrane resistance. 21

V_i Membrane potential of neuron i. 23, 46, 47

V_r Reset membrane potential. 46, 47

V_{th} Threshold membrane potential. 21, 46, 47

V	Membrane potential. 21, 22
Δ_T	Slope factor. 47
$\bar{G}_i$	Maximum membrane conductance to ion i. 22
τ_w	Adaptation time constant. 47
τ_{ref}	Refractory time constant. 47
τ_s	Synaptic time constant. 47
τ	Membrane time constant. 21, 46
a	Adaptation coupling parameter. 47
b	Variable which regulates the adaptation strength. 47
d	Transmission delay. 47
g_L	Leak conductance. 47
h_i	Inactivation variable of the i_{th} ion. 22
m_i	Activation variable of the i_{th} ion. 22
w_i	Adaptation variable. 47
w_{ex}	Excitatory synaptic strength. 47
w_{in}	Inhibitory synaptic strength. 48

Summary

Chapter 1

Introduction

The brain displays various oscillatory rhythms across scales that are related to one or multiple cognitive functions. One of the most prominent features in awake electroencephalograms (EEGs) of a variety of mammals, mainly observed at rest with eyes-closed, is the alpha (α) rhythm (around 7 to 13 Hz). This oscillation is observed in different regions of the cerebral cortex such as the auditory (Leske et al., 2014), sensorimotor (Haegens et al., 2015) and prefrontal areas (Supp et al., 2011), standing out in occipitoparietal regions.

Although alpha is strongly associated with reduced visual attention, it is also related to other functions such as the regulation of the timing and temporal resolution of perception, and transmission facilitation of predictions to visual cortex. Even early research already suggested that, rather than alpha existing as a singular phenomenon, it should be thought of as the product of many alpha rhythms (Walter, 1963). These many possible "characters" of alpha are better reviewed in (Clayton et al., 2017). Understanding how and where the alpha rhythm is generated can elucidate its functions. Even today there is no definitive answer to this question, though several hypotheses suggest the thalamus and the cortex as possible protagonists. The discussion about the generation of alpha includes studies with different animals and experimental techniques. Some evidence indicates a cortical generator (Bastos et al., 2014; van Kerkoerle et al., 2014; Halgren et al., 2019) as the source while other indicate the thalamocortical circuit as the source (Bollimunta et al., 2011; Robinson et al., 2001b).

There are at least three groups of neurons which supposedly could contribute to the cortical alpha rhythm. The first group are cortical layer 5 (L5) intrinsically bursting IB pyramidal neurons (Silva et al., 1991; Steriade et al., 1990; Jones et al., 2000), the second are high-threshold bursting thalamocortical neurons in the lateral geniculate nucleus (LGN) (Hughes et al., 2002, 2004, 2011; Lorincz et al., 2009) and, more recently, it was identified the L4 pyramidal neuron dendritic bursting (Traub et al., 2020) as the third group. Support for the thalamocortical cells alpha generation also comes from laminar recordings which found strong alpha at L4 and L6, the main targets of LGN efferents (Bollimunta et al., 2011).

Although the thalamocortical loop mechanism of alpha rhythm generation is well defined with a solid proposal, the L5 IB mechanism is not so clear. Different subtypes of layer 5 cells are possible candidates to be involved in the generation of alpha.

A subpopulation of layer 5 pyramidal cells that fire rhythmically in the alpha frequency range (Silva et al., 1991; Sun and Dan, 2009) has been suggested to serve as a neuronal pacemaker for the columnar microcircuit (Lopes da Silva, 1991; Jones et al., 2000, 2009; Connors and Amitai, 1997). Laminar recordings in V1 also suggest that the cortex acts as an independent generator of alpha, though it is not clear in what layer the rhythm starts. While experimental findings have identified generators of alpha oscillation in all layers (Bollimunta et al., 2008), there are studies suggesting the generation of alpha either in the corticothalamic way (generators in L6) (Bastos et al., 2014) or in the corticocortical path (generators in L1/2 and L5) (van Kerkoerle et al., 2014).

At the network level, the hypothesis of an origin in the thalamocortical loop has inspired a theoretical mean-field model that accounts not only for alpha rhythms, but also for evoked response potentials and changes in EEG spectra due to arousal, attention and pathology (Robinson et al., 2001b, 2002; Rennie et al., 2002; van Albada and Robinson, 2009; Izhikevich and Edelman, 2008; Hill and Tononi, 2005). The near-harmonic progression of oscillation peaks predicted by the mean-field model has recently been shown to be similar to the empirically observed pattern in resting eyes-closed EEG spectra from a large cohort of healthy individuals (van Albada and Robinson, 2013). The mechanism for alpha activity proposed by the mean-field model is an excitatory feedback loop between cortex and thalamus with a loop delay of the order of 100 ms (Roberts and Robinson, 2008).

We summarize some of the studies mentioned above in Tables 1.1 and 1.2. Even though different hypothesis have been suggested through the last years, some of them contradicting each other, still there is no definitive answer about the generation of alpha. In order to understand the possible mechanisms behind alpha rhythm generation, a thalamocortical model was developed and analyzed. To achieve this aim, as the first step we studied the spontaneous activity of the data-driven primary visual cortex model and the endogenous emergent phenomena of this network when parameters, such as the balance between excitation and inhibition, were varied. Then, the origin of alpha oscillation was explored at two different scales. One at the neuronal level involving (IB) neurons in cortical L5, and the other at the circuit level involving thalamocortical interactions. The model and methods can also be used to study other hypothesis and distinct oscillations in the future.

Reference	Technique	Brain region	Description	Alpha generator
Bollimunta et al. (2008)	LFP and MUA	V2, V4 and IT	Experiments done in macaque monkeys during performance of a sensory discrimination task.	Primary local pacemaking generator in infragranular layer of V2 and V4, and in supragranular layer of IT.
Bollimunta et al. (2011)	LFP and MUA	V1	Experiments done in macaque monkeys during performance of an intermodal selective attention task (visual vs auditory).	Primary local pacemaking generators in Layer 4C and deep layers.
Bastos et al. (2014)	LFP	LGN and V1	Alert macaque monkeys viewing stimuli known to produce strong cortical gamma-band oscillations	Alpha-band frequencies reflecting corticogeniculate feedback interactions (V1 to LGN).
van Kerkoerle et al. (2014)	MUA and LFP	V1 and V4	Experiments done with six adult macaque monkeys using microstimulation and infusing blockers of AMPA and NMDA.	α-waves are initiated in layers 1,2, and 5.
Hughes et al. (2004)	*In vitro* extracellular recordings and current clamp	LGN	Recordings from slices of the cat LGN *in vitro*.	High-threshold (HT) bursting neurons (Hughes et al., 2002), which are synchronized by gap junctions.
Lorincz et al. (2009); Hughes et al. (2011)	Extracellular recordings, multisite extracellular recordings and current-clamp	LGN	*In vitro* experiment under cholinergic input acting via muscarinic receptors.	Induction by cholinergic input acting via muscarinic receptors and shaped by a gap junction-coupled subnetwork of HT bursting TC neurons.

Tabela 1.1: *List of examples of previous works citing alpha generators hypothesis. Part 1.*

Reference	Technique	Brain region	Description	Alpha generator
Silva et al. (1991)	Intracellular recordings	Sensorimotor cortex	Recordings made from neurons in slices of rat sensorimotor cortex maintained *in vitro*. Spontaneous and evoked activity.	Neurons of layer 5 alone have the instrinsic properties to fire rhythmic patterns at 5 to 12 Hz and synaptic connections necessary to generate synchronized oscillations.
Haegens et al. (2015)	LFP and MUA	V1, S1, and A1	Experiments done in macaque during both spontaneous activity (auditory-only stimuli, no anesthesia) and sensory stimulation.	Strong source of alpha found in superficial layers.
Spaak et al. (2012)	Multicontact laminar electrodes. LFP	V1	Spontaneous cortical activity recorded from V1 of two awake monkeys (Macaca mulatta) at rest using a 24-contact laminar electrode. (no anesthesia)	It was found a robust coupling with anticorrelated power between alpha phase in the deeper layers and gamma amplitude in granular and superficial layers.
Saalmann et al. (2012)	Spike train activity and LFP	Pulvinar, V4 and TEO	Laminar profiles were obtained from coronal sections containing primary visual cortex (V1) prepared from brains of adult male Wistar rats.	Alpha rhythm generation dependent on dendritic bursting of L4 pyramidal neurons.
Traub et al. (2020)	LFP, MUA, CSD	V1	Simultaneously recorded neural activity in macaques in the pulvinar, V4, and TEO during visuospatial attention task.	The pulvinar predominantly influenced cortical alpha oscillations.

Tabela 1.2: *List of examples of previous works citing alpha generators hypothesis. Part 2.*

1.1 Structure of the thesis

This thesis is subdivided in six chapters. Chapter 2 provides an introduction to the neurobiology of the thalamocortical system related to alpha wave generation, and Chapter 3 provides a theoretical introduction to the techniques for modeling and analysing neuronal network models. Chapter 4 describes the thalamocortical model developed for this study and the choices of parameters to achieve a coherent spontaneous activity before testing the alpha rhythm hypothesis. Chapter 5 discusses the mechanisms of alpha rhythm generation on the thalamocortical network. Lastly, chapter 6 discusses the outcomes and conclusions of this work.

Chapter 2

Neurobiology of the thalamocortical system

This chapter provides the neurobiology of the thalamocortical system related to the generation of alpha oscilations in the cortex.

2.1 Introduction

The neocortex can be subdivided vertically into up to six cell layers (Uenke et al., 2010; Kandel et al., 2014). Each layer contains different populations of neurons, which vary in amount, shape and function. Variations in the number of layers, cytoarchitecture, and cellular distribution contribute to the functional specialization of different neocortical regions, which play a crucial role in sensory processing, attention, memory, consciousness, thought, and language (Bear et al., 2016).

The synaptic endings that reach the neocortex are mostly from itself. Such richness of cortico-cortical contacts underlies processes of sensory integration, motor command and memory consolidation (Braitenberg, 1974; Nieuwenhuys, 1994). These processes depend, however, on subcortical inputs, which help to organize behavior according to environmental and social demands (Bonelli and Cummings, 2007). One of the main sources of neocortex afferences is the thalamus, and thalamocortical interactions - which are bidirectional - are ultimately responsible for the oscillatory activity patterns under the different states of consciousness and sleep-wake cycle (Llinás and Steriade, 2006). Indeed, although thalamocortical connections was believed to account for less than 10% of the total synapses in the cortex, recent studies in primate visual cortex suggest that this number is two times bigger than was thought (Garcia-Marin et al., 2017). Additionally, other studies considered thalamocortical connections individually more influential than cortico-cortical contacts (Castro-Alamancos and Connors, 1997; Amitai, 2001).

In this study, two areas are modeled to explore the alpha rhythm generation: primary visual cortex (V1) and thalamic lateral geniculate nucleus (LGN). The neurobiology of these two areas are described below.

2.2 Primary visual cortex

The first region of the cortex that receives visual stimuli, the primary visual cortex (V1), plays essential role in the processing of visual information. It is also known as striate cortex or area 17 (accordingly with Brodmann's classification - see Figure 2.1).

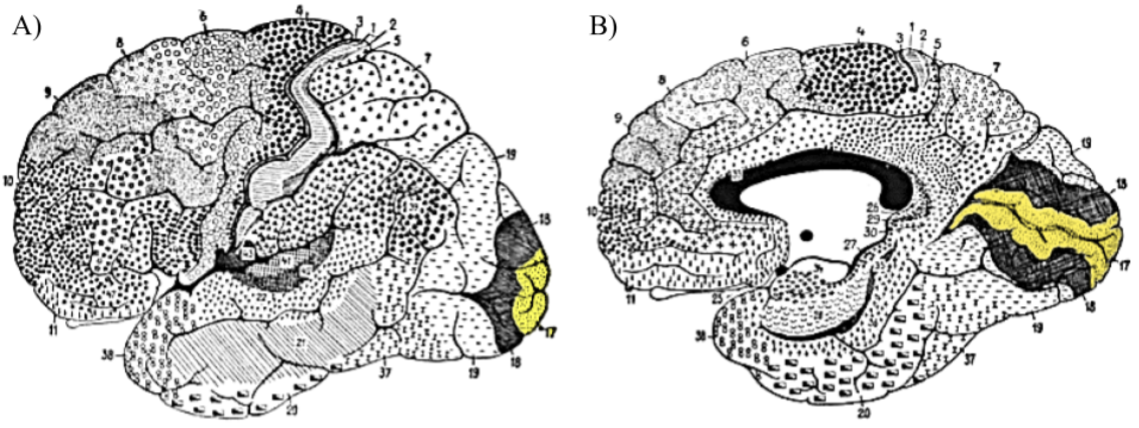

Figura 2.1: ***Cerebral cortex regions numbered and divided accordingly with Brodmann classification***. *A) Lateral view and B) medial view with area 17 indicated by yellow, which indicates the primary visual cortex. Images adapted from Brodmann (1909).*

In addition to the primary visual cortex, there are other regions responsible for processing visual functions, known as extra-striatal areas, given specific names or called V2, V3, V4, V5 and V6.

Similar to other cortical regions, V1 can be divided in six layers, each containing different number and types of neurons. Layer 4 of the V1 area is the main receptor for inputs from other brain regions. It is very thick and is divided by neuroanatomists into four sublayers: 4A, 4B, 4Cα, and 4Cβ. This subdivision is due to the receiving inputs from different regions of the LGN of the thalamus which can be grouped in these different sublayers. For simplicity, the sublayers were not considered in the computational modeling of the network architecture developed in this work. Additionally, LGN not only send projections to L4 but also to L6 as well.

Neurons in V1 present very specific patterns of response to visual stimulation in the retina. One of the most studied properties is the neuronal orientation selectivity response when a light bar is used as a sensory stimulus. V1 neurons are also selective to other different types of stimuli such as ocular dominance, color, spatial frequency, among others.

Besides these specific characteristics, there are some general features that we can use to group cortical neurons. One example is grouping them by their electrophysiological properties or spiking patterns. To understand these electrophysiological classes, we first have to know that synaptic or external currents can generate changes in the membrane potential of a neuron. Changes in the membrane potential of a neuron caused by synaptic currents are called postsynaptic potentials (PSPs). Fluctuations in the neuronal membrane potential caused by PSPs may generate an action potential or spike, ie, an abrupt and transient change in membrane voltage that propagates to other neurons through axons. This abrupt change occurs when the membrane potential reaches a firing threshold value. Considering a current injected as an input, for example in vitro, the pattern with which the action potentials occur varies according to the type of neuron and its location. According to the characteristics of the dynamics of these electrophysiological responses the neurons are grouped into classes. These classes bring together neurons that fire with similar patterns when stimulated by the same current.

There are 5 main electrophysiological classes in V1 (Contreras, 2004; Nowak et al., 2003): regular spiking (RS) neurons, intrinsic bursting (IB) neurons, fast spiking (FS), chattering (CH) and low-threshold spiking (LTS) neurons. Among these classes, in general, the most abundant are RS for excitatory and FS for inhibitory neurons.

The two major excitatory cortical cell types of layer 5 are the RS and IB neurons. IB cells produce bursts of spikes to somatic current injection, project sub-cortically, and have complex apical dendrites that branch deeper in cortex, not just at the pial surface (Connors and Gutnick, 1990; Agmon et al., 1992; McCormick et al., 1985). Other characteristics of IB neurons include the rhythmic bursting around 7 Hz observed by (Silva et al., 1991), which is hypothesized to be related with the generation of alpha oscillations.

2.3 Thalamic lateral geniculate nucleus

The lateral geniculate nucleus (LGN) is considered the thalamic relay of retinal input to the visual cortex. LGN is a "first order"relay (Sherman, 2006; Sherman and Guillery, 2011), which receives ascending visual messages from the retina and sends them to V1. The LGN in catarrhine primates (Old World monkeys, apes, humans) has six layers, except for gibbons (de Sousa et al., 2013; Kaas et al., 1978). These six layers are divided into four dorsal parvocellular layers and two ventral magnocellular layers (de Sousa et al., 2013; Kaas et al., 1978; Malpeli et al., 1996; Livingstone and Hubel, 1988; Hickey and Guillery, 1979).

Thalamocortical relay neurons (TC) from LGN can display two different modes of action potential temporal patterns: tonic and burst. In the tonic mode individual spikes occur when the TC cell is depolarized from its resting potential by a current pulse or activation of synaptic inputs. On the other hand, when the neuron membrane potential is hyperpolarized, a cluster of 2-6 spikes occurs in rapid succession. Although earlier studies suggested a separation between these two spiking modes, some observations have shown a continuum in the prevalence of both modes (Guido et al., 1995, 1992; Wolfart et al., 2005; Mukherjee and Kaplan, 1995).

Thalamic interneurons are inhibitory and represent 25% of the LGN population (LeVay and Ferster, 1979; Fitzpatrick et al., 1984; Arcelli et al., 1997; Çavdar et al., 2014; Madarász et al., 1985). They behave similarly with TC neurons with a higher firing rate when stimulated by the same step current (Pape and McCormick, 1995).

The thalamic reticular nucleus (TRN) is a brain structure which surrounds the anterolateral regions of the dorsal thalamus. It looks like a thin shell located between thalamus and cortex. TRN neurons are GABAergic and receive synaptic input from thalamocortical and corticothalamic neurons. Then, these cells provide inhibitory feedback to thalamic relay nuclei. For this work we are not considering the TRN because its firing rate is significantly reduced during α rhythm and its activity is uncorrelated with α activity (Lorincz et al., 2009).

Thalamocortical and corticothalamic projections

It is known that individual thalamocortical afferents contact both excitatory projection neurons and local inhibitory interneurons. Recently, in experiments done in cats, were found that thalamocortical synapses connecting LGN to V1 induces the same value of EPSP for RS and FS cortical neurons (Sedigh-Sarvestani et al., 2017). By the other hand, other studies showed that thalamocortical synapses onto inhibitory interneurons of somatosensory cortex and primary visual cortex are much stronger than those onto excitatory principal cells (Gabernet et al., 2005; Gibson et al., 1999; Inoue and Imoto, 2006; Kloc and Maffei, 2014).

Experiments done using optogenetic approach in mouse primary visual cortex studied the target-specific properties of thalamocortical synapses onto layer 4. Besides of LGN afferents making monosynaptic connections with pyramidal and fast-spiking (FS) neurons, it was shown that thalamocortical EPSCs on FS neurons were larger and showed steeper short-term depression in response to repetitive stimulation than those on pyramidal neurons (Kloc and Maffei, 2014).

Stronger thalamocortical responses of FS inhibitory L4 cells in comparison with RS response might be due to synaptic mechanisms such as synaptic excitatory conductance and innervation by greater numbers of thalamic cells (Cruikshank et al., 2007). Similar findings were observed for the mouse auditory cortex in vitro experiments (Schiff and Reyes, 2012).

Additionally, the projections in both directions involving thalamus and cortex are dynamical. The synaptic strength between these two areas can change with short-term synaptic plasticity. In vivo experiments done in cat primary visual

System	**Species**	**EPSP(mV)**	**EPSC(pA)**	**References**
V1L6 to LGN	rat	(—)	(5.0 ± 0.7)	(Granseth and Lindström, 2003)
	rat	(2.4 ± 0.1)	(—)	(Gentet and Ulrich, 2004)
LGN to V1L4-L6	cat	(0.42 ± 0.26)	(—)	(Sedigh-Sarvestani et al., 2017)
LGN to V1L4	cat	(1.97 ± 1.45)	(—)	(Stratford et al., 1996)
	mouse	(9.9 ± 0.7)	(—)	(MacLean et al., 2006)

Tabela 2.1: *Thalamocortical excitatory postsynaptic potential/current.*

cortex showed that thalamically driven PSPs depressed only moderately, even during high-frequency (100 Hz) trains. Thalamocortical synapses are tonically depressed by spontaneous activity, limiting the impact of additional evoked activity on synaptic efficacy (Boudreau, 2005). On the other hand, thalamocortical connections may display many forms of synaptic plasticity in the first postnatal week, but not afterwards (Amitai, 2001). LGN afferents make monosynaptic connections with RS and FS neurons. TC EPSCs on FS neurons were larger and showed steeper short-term depression in response to repetitive stimulation than those on RS neurons (Kloc and Maffei, 2014). Moreover, corticothalamic connections present short-term facilitation at cortical synapses to TC neurons and depression at cortical synapses to inhibitory thalamic neurons (Augustinaite et al., 2011). These synapses are dynamical and may change depending on the frequency of the input (Crandall et al., 2015). Some examples of thalamocortical and corticothalamic average EPSP and EPSC are shown in Table 2.1.

The thalamocortical loop delay may vary depending on the species as bigger brains tend to have longer projection paths. In Table 2.2 it is shown some examples of thalamocortical and corticothalamic transmission delays collected from literature for different species.

One of the alpha rhythm generation hypotheses studied in this work is related to the references mentioned in the last row of Table 2.2, for this reason, we used the total thalamocortical loop delay as 80 ms.

System	**Species**	**Conduction time (ms)**		**References**
		(mean range)	**(median)**	
Corticothalamic (L6)	rabbit	(2.0−42.7)	(14.3)	(Swadlow and Weyand, 1987)
	cat	(2.5−45.0)	(—)	(Ferster and Lindström, 1983)
	monkey	(2.0−20.0)	(9.5)	(Briggs and Usrey, 2009)
	ferret	(2.0−8.0)	(4.0 ± 0.6)	(Briggs and Usrey, 2005)
Thalamocortical (LGN)	rabbit	(0.6−3.1)	(1.2)	(Swadlow and Weyand, 1985)
	rabbit	(0.69−0.96)	(—)	(Stoelzel et al., 2008)
	cat	(0.3−9.7)	(0.9)	(Cleland et al., 1976)
	cat	(—)	(2.6 ± 0.64)	(Sedigh-Sarvestani et al., 2017)
	ferret	(1.0−4.0)	(2.9 ± 0.3)	(Briggs and Usrey, 2005)
Thalamus-cortex-thalamus	human	(80.0)	(-)	(Yamaguchi et al., 2018), (van Albada et al., 2010), (Robinson et al., 2001b)

Tabela 2.2: *Axonal transmission delays.*

Chapter 3

Data-driven large-scale brain modeling

Computational modeling in neuroscience has become an increasingly prominent field of research promoting, among other things, dialogue between experimental and theoretical analysis. Due to the accumulation of theoretical predictions based on experimental data, the computational approach has been increasingly useful for the design of new experimental studies and development of new theories. Moreover, it has been motivating the establishment of multidisciplinary research groups dedicated to brain issues. Examples are CEPID-FAPESP NeuroMat (`https://neuromat.numec.prp.usp.br/`), the Human Brain Project (`https://www.humanbrainproject.eu/`) and the Blue Brain Project (`http://bluebrain.epfl.ch/`).

Several models of the neocortex and its layers (Potjans and Diesmann, 2014; Izhikevich and Edelman, 2008), as well as thalamocortical circuits (Bazhenov et al., 2002; Hill and Tononi, 2004; Traub et al., 2004; Destexhe, 2009) have been developed in recent years. Potjans and Diesmann (2014) recently proposed a network model for a local cortical microcircuit that incorporates details of local connectivity between neurons of different layers, and reproduces, even with simplified leaky integrate-and-fire neurons, spontaneous activity consistent with that reported in experiments. This last model was extended into a large scale multi-area model based on macaque data where each area was represented by a modified version of the Potjans and Diesmann (2014) microcircuit (Schmidt et al., 2018a,b).

In addition to the network architecture, it is important that the neuron model used is able to reproduce the firing patterns of cells of the different electrophysiological classes present in both the cortex and the thalamus. Otherwise, network activity is less effective in sustaining biologically plausible population dynamics of the cortex (Tomov et al., 2016b, 2014b; Pena et al., 2018b) and thalamocortical circuits (Destexhe, 2009). Although these approaches are individually well established in the literature, they still need further integration for theoretical predictions on a broader level.

This chapter provides a theoretical introduction to computational neuroscience with a focus on data-driven large-scale brain models. It describes the basic elements to build these models from neurons to network structure. This chapter is an adapted version of the review article published in the European Physical Journal Special Topics: Shimoura, R.O., Lima., V., Pena, R. F. O., Kamiji, N.L., Girard-Schappo, M., Roque, A.C. (2021) Building a model of the brain: from detailed connectivity maps to network organization. *Europ. Phys. J. ST*. doi: https://doi.org/10.1140/epjs/s11734-021-00152-7.

3.1 Building a model of the brain: from detailed connectivity maps to network organization

With 86 billion neurons (Azevedo et al., 2009) and hundreds of trillions of synapses (Braitenberg and Schüz, 1998), the brain is one of the most complex systems in the known universe. Part of this complexity is due to the intricate pattern of connections among brain cells. Arguably, the computations performed by the brain depend heavily on the connections among its cells, but how? In other words, how the structure of the brain is related to its function? Many argue that since the brain is a complex system its functions are more than the sum of its parts (Tononi et al., 1994, 1998; Koch and Laurent, 1999; Bassett and Gazzaniga, 2011). So, knowledge of the individual behavior of the brain components is not enough to explain its emergent properties, e.g. cognition and consciousness. Therefore, the task of modeling the brain connectivity with a reasonable degree of accuracy constitutes an essential step for understanding these emergent phenomena.

Building-block strategies where spatial and temporal scales are individually modeled are the *modus operandi* of computational neuroscience. Ionic currents are modeled and studied in separate, neurons are studied in separate, populations are studied in separate, and the emerging behavior from the interaction of these "blocks" is then studied via mathematical and computational models. However, the step from single to multiple and interconnected cells is not trivial, neither from the point of view of behavior nor from the point of view of data extraction and coding.

But why is coding the structure of neuronal connections and not only the individual cells so important? We may look for hints on this question in different phenomena in nature. Starting with inanimate matter, we find that the crystalline structure of materials directly influences their thermal, electric, magnetic and optic properties (Newman and Barkema, 1999; de Gennes and Prost, 1993). In addition, the dimensionality of the lattice, as expressed by the number of neighboring sites to each node in the network, as well as the reach of interactions, is known to alter significantly the behavior of physical observables in the vicinity of a phase transition (Ódor, 2004). The flow of current and, consequently, the expected behavior of electric circuits, is highly dependent on the spatial configuration of resistors, sources, capacitors and inductors, and on how their branches intertwine between some input and output of electric signal. When conducting nanoparticles are arranged into a percolating structure, complex activity arises in the circuit via bursts of switching conductivity (Mallinson et al., 2019). Due to its intricate cortical-like activity, this condensed matter device could serve as prototype for neuromorphic hardware.

Although the brain is not an ideal and isolated electric circuit, the most accepted model for the neuronal membrane is based on an equivalent circuit made of a capacitor coupled in parallel to resistors and batteries (Johnston and Wu, 1995). Hence, the structure of the brain, reflected on its immense electrical circuitry, works as a complex web that shapes neuronal activity, and ultimately determines brain function as a kind of process that lies in a continuous feedback loop with the embedding environment. Neuroscience is then tasked with relating a set of inputs to the brain (e.g., via sensory systems), to the corresponding generated outputs, also known as functions. Although the intended function is not always clear, we can have a look at the activity of specific brain regions to get clues on whether a particular structure of a computational model makes sense.

Examples of this structure-function interdependence come from experimental and theoretical studies alike (Sporns, 2010; Tomov et al., 2014a; Girardi-Schappo and de Andrade Costa, 2020): spontaneous cortical activity is sometimes observed in the form of bursts of action potentials, known as neuronal avalanches (Hesse and Gross, 2014; Carvalho et al., 2021). Nevertheless, when a group of researchers built a lattice-like network of neurons from the scratch *in vitro*, they did not observe these complex patterns (Tibau et al., 2013). However, adding modular structure to the lattice may do the job (Yamamoto et al., 2018). These modules could then be built on top of each other generating a layered structure that mimics the cortex. These layered networks are known for generating propagating waves (Bortolotto et al., 2016; Muller et al., 2018), long-range correlations (Girardi-Schappo et al., 2016; Arnulfo et al., 2020), and neuronal avalanches (Girardi-Schappo and Tragtenberg, 2018). Rich-club-like modularity destroys bursting synchrony (Lameu et al., 2012), but allows for neuronal avalanches (Kaiser et al., 2007), whereas hierarchical networks of this type optimize the diversity of spiking patterns (Pena et al., 2020). Some types of plasticity lead networks of neurons into a modular topology (Lameu et al., 2019). In fact, evolving techniques of manipulating neuronal activity may give birth to synthetic biological brain structures, also known as connectomes (Rabinowitch, 2019).

3.2 How network models are usually constructed

Neuronal network models can be classified along two different axes with respect to connectivity. The first one refers to the nature of the graph used to implement the network, and the second to the granularity or scale of the connections.

Regarding the nature of the graph, it can be of two basic types:

- **Artificial graph**. The connections among neurons are generated according to some predefined rules with the specific aim of creating a network with desired properties, e.g. random or small-world topologies (Roxin et al., 2004; Lin and Chen, 2005; Sporns, 2010; Borges et al., 2017).

- **Data-driven graph**. The connections among neurons are based on experimental data obtained with different techniques with the aim of replicating as faithfully as possible the circuitry of a particular brain region (Bezaire et al., 2016; Dura-Bernal et al., 2017; Brunton and Beyeler, 2019).

Regarding the granularity of the connectivity, it is tied to the scale at which neural structures are described. There are three basic granularity levels:

- Connections linking **morphologically detailed neurons**. Synaptic contacts occur at specific positions along the neuron, e.g. distal/proximal dendrites or somata. Models that want to take into account the positions of synaptic contacts must be based on morphologically detailed neuron models. These models are composed of several interconnected compartments emulating the branched structure of the neuronal dendritic trees (Segev and Burke, 1998; Herz et al., 2006; Sterratt et al., 2012). Each compartment can have its own set of ionic channels and maximal ionic conductance densities. With this type of neuron model, connections among neurons can be set in a compartment-wise fashion, including compartment-specific values of the synaptic parameters.

- Connections linking **point neurons**. At a coarser grain level, neurons can be described as points without spatial structure. In such cases, to set the connections among neurons one needs only to specify which cells are connected to which (usually according to some probabilistic rules) together with the connection parameters (type and strength) of the cell-to-cell synapses (Brunel, 2000; Gerstner et al., 2014; Potjans and Diesmann, 2014).

- Connections linking **neuronal populations**. At an even coarser spatial granularity level, individual cells are no longer recognized as such and groups of neurons are lumped together into single "average" neuron (Dayan and Abbott, 2001; Liley, 2015; Cowan et al., 2016). In such neuronal population models the connections represent axonal links among neuronal groups or brain regions and the synaptic parameters correspond to effective properties of the existing synapses.

The artificial graph approach has been used to study cortical activity states (Brunel, 2000; Ostojic, 2014; Pena et al., 2018a; Borges et al., 2020), specially transitions between up and down states (Destexhe et al., 2001; Pena et al., 2018a); how basic information processing computations are performed by a population of neurons (Vogels et al., 2005); and to understand low-level operations performed by cell assemblies (Buzsáki, 2010; Papadimitriou et al., 2020).

It is known that the primate cortex is organized in a structured manner (Sporns et al., 2005; Bullmore and Bassett, 2011). Indeed, the connection among cortical regions resemble the structure of small-world networks (Watts and Strogatz, 1998), with clusters sparsely connected among them, as well as with strong interconnections. There is also evidence that the cortex has a hierarchical structure (Mountcastle, 1997; Kaiser and Hilgetag, 2010; Meunier et al., 2010), meaning that the cluster has smaller clusters nested within them. This topology allows different regions to be relatively independent to process information and be specialized in distinct functions (Tomov et al., 2014a, 2016a; Pena et al., 2020). However, the existence of pathways connecting the clusters also allows for information to be integrated among different regions.

The data-driven approach is supported by the massive amount of data that is routinely gathered using different techniques on neuronal microcircuits of different brain regions (Shepherd and Grillner, 2018). They demonstrate how microcircuits in the brain are highly specific in terms of their connectivity and the impact of this specificity on function. For example, there is a high specificity in the vertical pattern of connections among neurons in distinct cortical layers (Thomson et al., 2002; Binzegger, 2004). The pattern of cortical microcircuitry endows the recurrent cortical network with specific computational properties (Li et al., 2013; Lien and Scanziani, 2013).

3.3 Obtaining structural data

In recent years, efforts to characterize the connectivity maps (connectomics) representing the cortical structure have been made (Sporns, 2011; Betzel, 2020). These connectivity maps can span several scales, from the intra- and interlayer connections in a cortical microcircuit to connections linking cortical regions (Paxinos et al., 2000; Sporns et al., 2005; Alivisatos et al., 2013; Stephan, 2013), depending on the techniques used to obtain them. Since these maps track synaptic connections at the neuronal level, and white matter pathways connecting cortical areas at meso/macro-scale level, they are referred to as structural connectivity maps. Usually, the structural connections can be mapped using magnetic resonance imaging (MRI) based techniques such as diffusion tensor (or weighted) imaging (DTI/DWI), and tractography (Basser et al., 1994). The connectivity for local cortical microcircuits can be obtained by means of electrophysiological techniques (Markram et al., 2015), axonal tracing (Kuypers and Ugolini, 1990; Saleeba et al., 2019), and electron- (Denk and Horstmann, 2004) and light- (Shen et al., 2020) microscopy. More details about different ways to extract anatomical information and use them to build neuronal network models are given elsewhere (van Albada et al., 2020).

Similar approaches are employed for other brain areas. Anatomical explorations of the hippocampus date back to the works of Ramon y Cajal with Golgi staining techniques. The highly specific pattern of connections within the limbic system has been revealed through advanced MRI or neuroanatomical tract-tracing techniques (Andersen et al., 2006; Kajiwara et al., 2008; Van Strien et al., 2009; Witter, 2010; Maller et al., 2019).

With the increasing number of data collected, the structural or functional connectivity maps started to be used in modeling studies. Consequently, there are several projects aiming at the construction of realistic brain models, such as the Human Brain Project (Amunts et al., 2019), the Blue Brain Project (Markram, 2006), or the Allen Brain Explorer (Wang et al., 2020). These are examples of projects being funded around the world (Kandel et al., 2013; Landhuis, 2017). Faithful models constructed upon the connectivity data available were built in order to understand how the brain connectivity structure impacts the dynamics of the system, and to which phenomena the information contained in these maps are crucial (Plesser et al., 2007; Potjans and Diesmann, 2014; Kunkel et al., 2014; Schmidt et al., 2018a,b). A major advantage of such models is the construction of canonical models for similar brain areas: all over the neocortex there is a similar six-layered organization whereas for the archicortex and paleocortex there is a three- or four-layered structure (Shepherd and Rowe, 2017). Once a specific microcircuit of such areas is built, it is then used as a building block to enlarge a given network model or to connect it to other areas.

3.4 The neuron model

The choice of the neuron and synaptic models have an impact on the modeling results. So, they will be briefly reviewed in this and the next subsection. In terms of the neuron, the phenomenology of spike-train generation can be implemented without specific modeling of the underlying biophysical mechanisms but only by modeling the lipid bilayer of neurons by an equivalent passive RC circuit. In this simplified case the membrane voltage (V) is described by $\tau dV/dt = -V + RI = f(V)$, where τ is the membrane time constant, R is the membrane resistance, and I the injected current. Since this model cannot generate an action potential by means of its own dynamics, an artificial mechanism of fire-and-reset is usually included where spikes are counted whenever V crosses a certain threshold value V_{th} with a subsequent reset. The function of V on the right-hand side is not restricted to be linear and can be nonlinear as well. These models are referred to as integrate-and-fire (IF) type models (Gerstner et al., 2014).

The integrate-and-fire model can be extended in a variety of ways with the inclusion of elements that capture features of neuronal firing behavior. Two-dimensional integrate-and-fire models include equations to tackle feedback effects from ionic currents. Generally, such models can be expressed by the coupled ODEs: $dV/dt = f(V) - w$, $dw/dt = G(V, w)$. Due to their dynamical properties, two-dimensional integrate-and-fire models posses a richer repertoire of behaviors that can be fitted to experimental *in vivo* and *in vitro* data to reproduce characteristic firing patterns of neurons (Izhikevich, 2003; Brette and Gerstner, 2005a). Effects such as oscillations or subthreshold resonance can be described as well (Pena et al., 2018a). Another class of neurons that can be used are the ones with discrete time, the so-called map-based neurons (Girardi-Schappo et al., 2013). This class of neurons is particularly interesting because they have a rich dynamical repertoire of spiking activity, and allow for relatively easy analytical tractability and efficient simulations (Girardi-Schappo et al., 2017).

Another class of neuron models is the one comprised by so-called conductance-based models, which explicitly describe the activation and inactivation dynamics of the gated ionic channels present in the neuronal membrane. This formalism originates from the seminal work of Hodgkin and Huxley in 1952 (Hodgkin and Huxley, 1952). The generic equations of a conductance-based neuron model is as follow:

$$C_m \frac{dV}{dt} = -\sum_i I_i + I_{\text{inj}} \tag{3.1}$$

where

$$\begin{aligned} I_i &= \bar{G}_i m_i^r h_i^s (V - E_i) \\ \frac{dx_i}{dt} &= \frac{x_{i,\infty}(V) - x_i}{\tau_{x_i}(V)}, \quad (x = m \text{ or } h). \end{aligned} \tag{3.2}$$

In these equations, C_m is the membrane capacitance, V is membrane voltage, I_i is the ionic current of the ith ion, $\bar{G}_i$ is the maximal membrane conductance to ion i, m_i and h_i are, respectively, the activation and inactivation variables of the membrane conductance to the ith ion, r and s are small integers, E_i is the reversal membrane potential of ion i, and $\tau_{x_i}(V)$ and $x_{i,\infty}(V)$ are, respectively, the voltage-dependent activation/inactivation time constant and steady-state value (Sterratt et al., 2012). In Figure 3.1 we show a schematic representation of the simplified (integrate-and-fire) and conductance-based modeling approaches. All these neuron models can be adapted to describe neurons with a specific morphology, by defining discrete compartments (each of which obeys a certain membrane potential) that are electrically coupled to each other.

3.5 The synapse model

Synapses can also be modeled at different levels of biological plausibility and the choice of synaptic model is crucial for the simulation of large-scale networks, since the number of synapses is much higher than the number of neurons. To model a synapse, one could simply define an event-driven model by incrementing the synaptic conductance or the synaptic current by a certain amount; or, on the other hand, consider more complex processes such as those of the conductance-based approach where the synaptic conductance depends on the membrane voltage of the

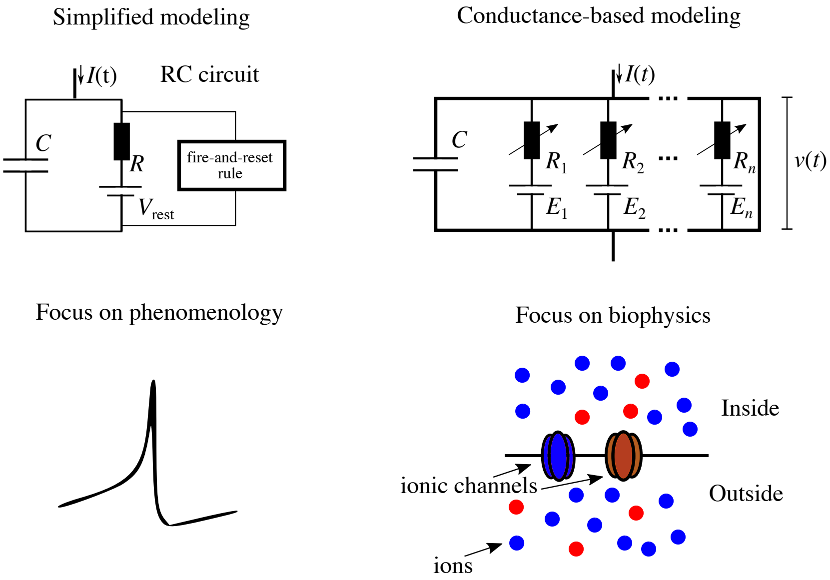

Figura 3.1: *Different types of neuron model*. *Left: The simplified approach taken by integrate-and-fire models uses a fire-and-reset rule set "by hand" to model a spike. Right: The conductance-based approach models ionic currents using the Hodgkin-Huxley formalism.*

postsynaptic neuron (Roth and van Rossum, 2010; Gerstner et al., 2014). Either way, the parameters of the model can be chosen to reproduce the behavior of excitatory synapses mediated by glutamate receptors (AMPA and NMDA), and/or inhibitory synapses mediated by GABAergic receptors ($\mathrm{GABA_A}$ (ionotropic) and/or $\mathrm{GABA_B}$ (metabotropic)) (Roth and van Rossum, 2010). Additionally, the synaptic strengths can be static or dynamic, and the latter case has been the focus of intense research aimed at modeling plastic synapses of both short and long term (Tsodyks et al., 1998; Castellani et al., 2001; Tsodyks, 2005; Clopath et al., 2010).

The electric current $I_{ij}^{\mathrm{syn}}(t)$ generated by a single synapse from a neuron j (presynaptic) to a neuron i (postsynaptic) has the form (Roth and van Rossum, 2010),

$$I_{ij}^{\mathrm{syn}}(t) = G_{ij}(t)\left[V_i(t) - E_{ij}^{\mathrm{syn}}\right], \tag{3.3}$$

where $G_{ij}(t)$ is a time-dependent conductance, V_i is the postsynaptic membrane potential, and E_{ij}^{syn} is the reversal potential of the synaptic current. The value of E_{ij}^{syn} determines whether the synapse $j \to i$ is inhibitory or excitatory (typical values of E_{ij}^{syn} are 0 mV for excitatory synapses and -75 mV for inhibitory ones). For integrate-and-fire type models, a simplification that is often done is to fix V_i (e.g.

at resting voltage) and incorporate the battery term into $G_{ij}(t)$ so that Eq. (3.3) reads $I^{\text{syn}}_{ij}(t) = J_{ij}(t)$. The term $J_{ij}(t)$ is the amplitude of the postsynaptic current (called synaptic strength or efficacy) and its sign determines whether the synapse is inhibitory (negative sign) or excitatory (positive sign).

An example of short-term synaptic plasticity (Tsodyks et al., 1998) is the facilitation-depression dynamics given by Eqs (3.4)–(3.6). This model contains two variables that represent the fraction of presynaptic channels that are open u_{ij}, and the fraction of neurotransmitters that are available to be released x_{ij}. Upon a spike in the presynaptic neuron, the synaptic conductance $G_{ij}(t)$ is increased by a factor $u^{+}_{ij} x_{ij} J_{ij}$, where $J_{ij}(t)$ is the synaptic strength (a parameter) and the superscript $^{+}(^{-})$ indicates the moment after (before) the spike. The interplay of the time constants τ_{fac} and τ_{dep} determines if a synapse will have a temporal depression or facilitation:

$$\frac{du_{ij}}{dt} = -\frac{u_{ij}}{\tau_{\text{fac}}} + U\left(1 - u^{-}_{ij}\right)\delta\left(t - t^{f}\right), \tag{3.4}$$

$$\frac{dx_{ij}}{dt} = \frac{1 - x_{ij}}{\tau_{\text{dep}}} - u^{+}_{ij} x \delta\left(t - t^{f}\right), \tag{3.5}$$

$$G_{ij}(t) = u^{+}_{ij} x_{ij} J_{ij} \delta\left(t - t^{f}\right), \tag{3.6}$$

where t^{f} is the time at which the presynaptic neuron fires a spike, and U is the proportion of new open calcium channels upon a presynaptic event. Examples of both short-term depression and facilitation can be seen in Figure 3.2. The facilitation-depression model can be further simplified to a case without short-term plasticity by making u and x constants.

Alternatively, the synaptic strength can be determined by a spike timing dependent plasticity (STDP) rule, i.e., the increment or decrement of the synaptic efficacy is calculated using the relation between the times of pre- and postsynaptic spikes (Markram et al., 1997; Morrison et al., 2008; Sjöström and Gerstner, 2010). Such rules are based on experimental evidence (Sjöström et al., 2001; Shimoura et al., 2015), and are applicable to both excitatory and inhibitory synapses (Kepecs et al., 2002; Kleberg et al., 2014). Let us assume that the synaptic efficacy of a $j \to i$ synapse can be described by a single variable $J_{ij}(t)$. The STDP rule can be implemented by defining two auxiliary variables, $x_j(t)$ and $y_i(t)$, which must be integrated over time. These variables are used to model the strengthening of the synapse when the presynaptic spike precedes the postsynaptic spike, and the weakening of the synapse when the presynaptic spike follows the postsynaptic spike, respectively. Then, a simplified STDP rule for excitatory synapses ($J_{ij} > 0$) is defined as (Gerstner et al., 2014; Sjöström and Gerstner, 2010)

$$\frac{dx_j}{dt} = -\frac{x_j}{\tau_+} + \sum_f \delta(t - t_j^f)\,, \tag{3.7}$$

$$\frac{dy_i}{dt} = -\frac{y_i}{\tau_-} + \sum_f \delta(t - t_i^f)\,, \tag{3.8}$$

$$\frac{dJ_{ij}}{dt} = x_j(t)\, A_+\, \Theta(J^{\max} - J_{ij}) \sum_f \delta(t - t_i^f) - y_i(t)\, A_-\, \Theta(J_{ij}) \sum_f \delta(t - t_j^f)\,, \tag{3.9}$$

where t_j^f and t_i^f are the spike times of the pre- and postsynaptic neurons, respectively, $\tau_{+,-}$ are the decay time constants of x_j and y_i, respectively, $\Theta(u)$ is the Heaviside function, $A_{+,-} > 0$ are the synaptic strength increment and decrement parameters, and $J^{\max}$ is the maximum value of synaptic efficacy.

Eqs. (3.7) to (3.9) work like this: every time a presynaptic spike occurs, two things happen: first, x_j is instantaneously increased by a unitary amount and then decreases exponentially with time constant τ_+ and, second, while $J_{ij} > 0$ it is instantaneously decreased by $y_i A_-$. On the other hand, every time a postsynaptic firing occurs, another two things happen: first, y_i is instantaneously increased by an unitary amount and then decreases exponentially with time constant τ_- and, second, while $J_{ij} < J^{\max}$ it is instantaneously increased by $x_j A_+$. This is captured by the scheme in Figure 3.2(c): the variable x_j is responsible for the exponential increase on the left-hand side (green part) of the hyperbole, since it only adds to J_{ij} when $T_{\text{post}} > T_{\text{pre}}$ (a postsynaptic spike happens after a presynaptic spike); conversely, y_i is responsible for the exponential decrease on the right-hand side (red part) of the hyperbole, since it is only subtracted from J_{ij} when $T_{\text{post}} < T_{\text{pre}}$ (a postsynaptic spike happens before a presynaptic spike). Note that $T_{\text{post}} = t_i^f$ and $T_{\text{pre}} = t_j^f$ in the figure.

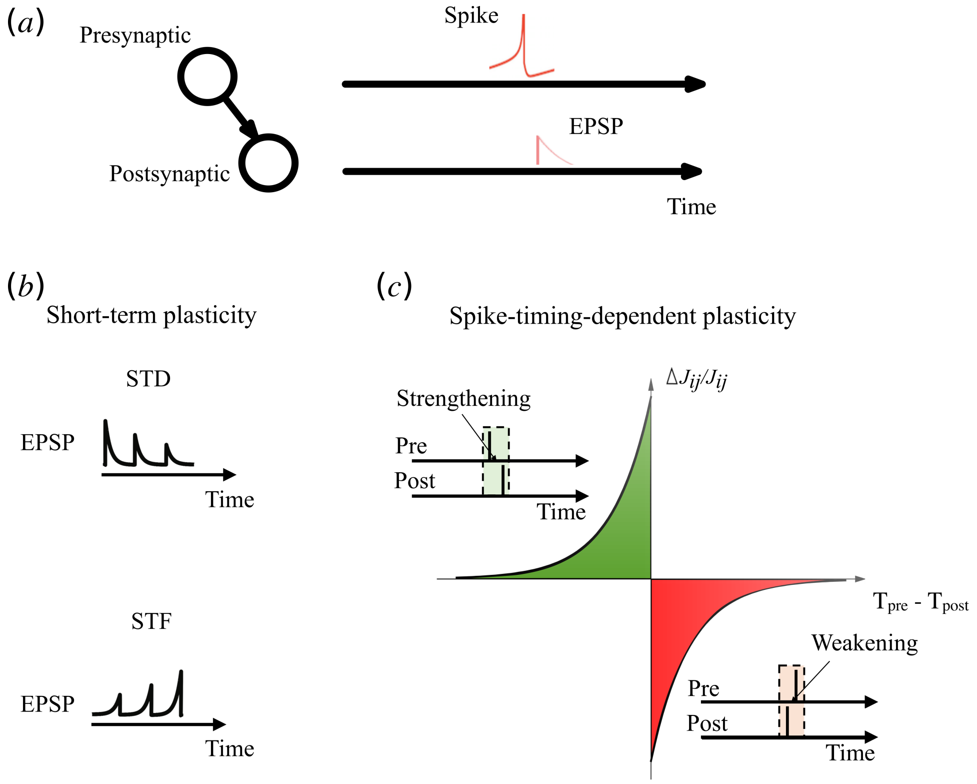

Figura 3.2: ***Different synaptic models.*** *(a) Upon a presynaptic spike, an excitatory postsynaptic potential (EPSP) is created in the postsynaptic neuron after a synaptic time delay (a similar scheme can be implemented for an inhibitory synapse). The amplitude of the postsynaptic potential can change over time depending on some plasticity rule. (b) A short-term plasticity rule decreases or increases the EPSP amplitude over time depending on depression (STD) or facilitation (STF), respectively. (c) A spike-timing-dependent plasticity (STDP) rule changes the synaptic strength depending on the temporal difference between pre- and postsynaptic spikes.*

3.6 How to implement connectivity maps in network models

3.6.1 Connectivity maps for networks of point neurons

The translation into a computational network model from experimental data is not an easy task. Different levels of complexity require distinct ways to organize the extracted information into a connectivity map. Such a map may represent inter- or intra-areal connections, and in both cases the rules to implement the connections are similar. Our focus here is mainly on models at the microcircuit level, where a small piece of the brain as shown in Figure 3.3(a) is zoomed and its structure is represented by a connectivity matrix (Figure 3.3(b)) or ring of connections (Figure 3.3(c)). The same connectivity map can be used to generate networks with different levels of biological structural details as in Figure 3.3(d), where each node can represent a population of neurons or individual neurons. In the latter case, individual neurons can also be modeled by complex structures instead of just a point. Moreover, the information from the connectivity maps can also be expanded to add other features as spatiality (Figure 3.3(e)). In this section we will discuss in a guided manner how to better approach the above tasks.

Usually, connectivity maps are reported as matrices of connection probabilities where the rows/columns refer to the source/target elements (single neurons or neuronal populations) in the network. In a point neurons network with no spatial notion, the matrix gives all the information needed to build the network. The implementation is similar to the simplest case of a random network of the Erdős-Rényi type (Newman, 2010) where there is only one connection probability for all neuron pairs, thus one can draw connections by testing each neuron pair against this connection probability.

The way in which the testing mentioned above is implemented is of utmost importance. Choices such as pair combinations with or without replacement can create far different network graphs. Usually, the synaptic connectivity is established in a network model by attributing to each pair of neurons (or populations) a random number between zero and one drawn from an uniform distribution, and then testing it against the predefined connection probability for the pair. This choice avoids multiple synapses between the same neuron pair, which could be desirable or not. Moreover, data-driven connectivity maps at microcircuit level are usually directed graphs, i.e. pairs of neurons are not necessarily connected in a reciprocal way.

Alternatively, a distinct testing scheme would be to calculate the total number of synapses (N_{syn}) among neurons based on the connection probability, and randomly draw lists containing N_{syn} pre- and post- synaptic indexes. In this method, multiple synapses between the same neuron pair are possible. An important detail is that these two schemes can deliver equivalent results depending on how N_{syn} is calculated.

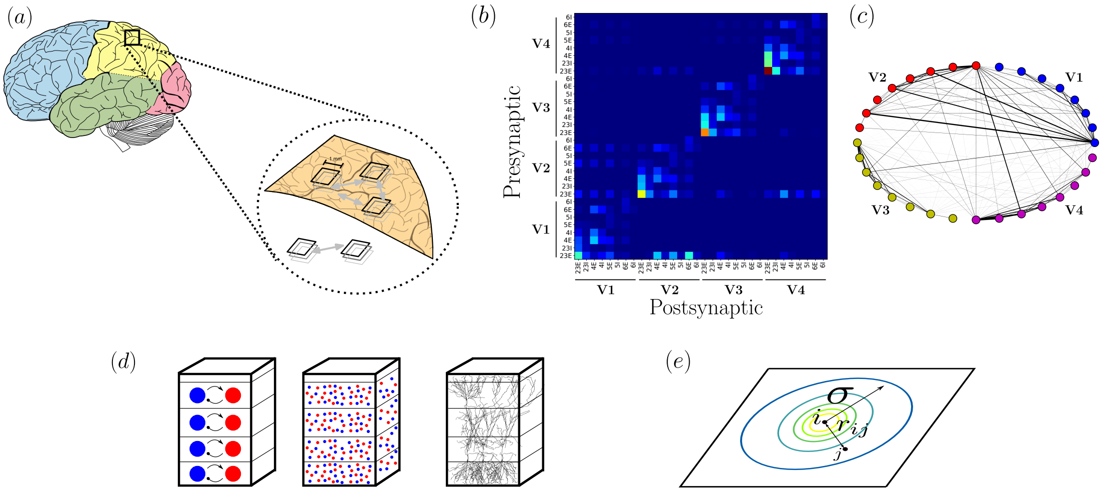

Figura 3.3: ***From structural data to the neuronal network model.*** *Data for this example were taken from a multi-scale model of the macaque visual cortex (Schmidt et al., 2018b,a). In (a) we show a illustrative depiction of the human cortex. The zoom indicates a cortical slice and the black squares represent cortical microcircuits. In (b) we show the structural connectivity matrix. Neurons are of excitatory or inhibitory types (E, I) and belong to four different cortical layers (2/3, 4, 5, and 6) in four different cortical areas ($V1$, $V2$, $V3$, and $V4$). Presynaptic neurons are placed in the x-axis and postsynaptic neurons in the y-axis; Notice that the structural connectivity matrix is asymmetric. In (c) we show a network representation of the structural matrix in (b); neurons are placed along a ring and connections between pairs of them are indicated by lines. In (d) we show the different levels of spatial granularity at which a cortical microcircuit could be simulated: all excitatory/inhibitory neurons in a given layer can be described by a neural population model (left column); each individual cell can be represented by a point neuron model; or each individual cell can be described by a morphologically detailed neuron model (right column). As one goes from the left to the right column the number of equations and parameters of the full model increases dramatically, and, consequently, the computational cost involved in the implementation and simulation. This makes critical the choice of trade-off between the kind of phenomenon studied and the spatial granularity level of the model. In (e) we show how one could connect pairs of neurons using a distance based rule given by a probability density function as the 2D Gaussian function defined in Eq. 3.13. The colored circles indicate the contour lines of the distance based function and the presynaptic neuron is placed at the center of the inner contour line.*

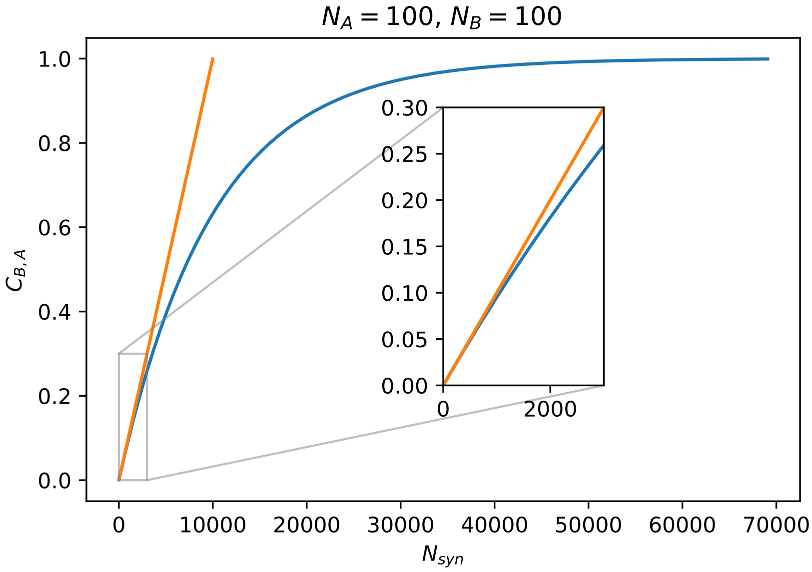

Figura 3.4: ***Connection probability calculated by the exact expression and its first-order approximation.*** *Connection probability between two neuronal populations, A and B, as a function of the number of synapses* N_{syn} *between them when calculated by the exact formula (Eq. 3.10) (blue) and its first-order approximation (Eq. 3.11) (orange). Inset: zoom over small values of* N_{syn} *to highlight the beginning of the difference between the two curves.*

An example of such differences can be found in a recent replication of the Potjans-Diesmann cortical microcircuit model (Potjans and Diesmann, 2014) by us (Shimoura et al., 2018). Depending on the way the connection probability $C_{B,A}$ between a neuron j in source population A of size N_A and a neuron i in the target population B of size N_B is calculated, there are notable differences on the average spiking behavior of Layer 5 neurons. The exact value of $C_{B,A}$ is given by

$$C_{B,A} = 1 - \left(1 - \frac{1}{N_A N_B}\right)^{N_{\text{syn}}}, \tag{3.10}$$

where N_{syn} denotes the total number of synapses between populations A and B. For $N_{syn}/(N_A N_B)$ small, the Taylor expansion of Eq. 3.10 to first order results in the approximate expression for $C_{B,A}$ given by

$$C_{B,A} = \frac{N_{\text{syn}}}{N_A \cdot N_B}. \tag{3.11}$$

Figure 3.4 shows a comparison of the curves of $C_{B,A}$ *versus* N_{syn} calculated by Eqs. 3.10 and 3.11 for fixed numbers of neurons in populations A and B. For a small number of synapses N_{syn} the two equations give equivalent connection probabilities but as N_{syn} becomes larger the exact expression and its approximation diverge significantly. This reflects on the structure of the network and, consequently, on the activity (see (Shimoura et al., 2018) for a more detailed discussion).

Moreover, one has to determine whether connectivity maps indicate incoming or outgoing synapses. In a similar manner, instead of defining the total number of synapses between two populations, a distinction between in-degree and out-degree may be necessary.

Another key point would be for maps that involve connectivity dependent on morphology. In these more complex structures, more elaborate methods involving multiple steps before deciding for the creation of connections may be necessary. Notice that the methods described above do not take into account the neuronal morphology or even the spatial notion while placing neurons on a grid. In order to incorporate these information, the connectivity matrix alone may not be sufficient.

From the point of view of spatial organization, there are limitations with respect to the maximum distance a neuron can send projections or to its target preferences. For the first case, a distance dependent connection probability may be required or, similarly, a fixed connection probability coupled to a distant dependent rule. Regardless of the way, neurons have to be placed on a spatial grid with a chosen dimension so distance dependent synapses can be created. As an example, consider the case of a two-dimensional (2D) grid where space is discretized in (x,y) positional variables and each neuron can assume a position in this (x,y)-grid. One can then define the absolute distance r_{ij} between a presynaptic neuron i and a postsynaptic neuron j,

$$r_{ij} = \sqrt{\Delta x_{ij}^2 + \Delta y_{ij}^2}, \tag{3.12}$$

where $\Delta x_{ij} = \mid x_i - x_j \mid$ and $\Delta y_{ij} = \mid y_i - y_j \mid$. Notice that these distances may have limitations determined by boundary conditions. For example, in a 2D square grid of size $L \times L$ with periodic boundary conditions, Δx_{ij} as defined above is only valid for $\mid x_i - x_j \mid \leq L/2$, otherwise $\Delta x_{ij} = L - \mid x_i - x_j \mid$. The same is valid for Δy_{ij}. Other boundary conditions could also be applied.

Once neuronal distances are handled, network connections can be set up by using the previously stated connectivity matrix as the zero-distance connection probability, and then test for pairs of neurons against a distance dependent connectivity rule. An example is given for a Gaussian probability density distribution,

$$c(r_{ij}) = C_{B,A} e^{-r_{ij}^2/2\sigma_A^2}, \tag{3.13}$$

where σ_A is the standard deviation. This equation is valid for $r_{ij} \leq R$, with R the maximal distance a neuron projection can reach. A similar approach can be applied for a network with 3D spatial notion. Other distributions such as the exponential are often used.

3.6.2 Connectivity maps for networks of neurons with morphology

Other biological features can be implemented together with the distance dependence when creating the connections, an example is the direction tuning dependency for visual systems (Billeh et al., 2020). Nevertheless, in a more general manner, the next step towards adding structural complexity to the network is the implementation of neuronal morphology. For this, as an approximation, it is possible to use the same connection probability rules described above and define which pairs of neurons are connected using as reference their somata positions. Then, an additional procedure is required for creating the connections: the distribution of synapses along the neuronal dendritic tree. Different neurons may receive synaptic inputs with distinct distribution patterns in a cell-type and brain region dependent manner.

Consideration of cell morphology is important when details related to specific locations of synaptic contacts are potentially relevant. An example is the organization of synaptic contacts involving inhibitory interneurons in the cortex. While parvalbumin-expressing (PV) interneurons target preferentially the somata of pyramidal cells, somatostatin-expressing (SOM) cells target their distal dendrites (Kawaguchi and Kubota, 1997; Tremblay et al., 2016). This feature makes the response of a cortical pyramidal neuron to inhibitory input dependent on the type of cell that provides the inhibition. For example, the degree of attenuation of inhibitory postsynaptic potentials depends on where in the soma-dendritic domain of the pyramidal neuron they occur (Safari et al., 2017). Similarly, in the hippocampus the modulatory effects on the spiking activity of pyramidal cells due to inhibitory inputs from oriens lacunosum moleculare (OLM) interneurons depend on the locations of these synaptic inputs (Leão et al., 2012). Brain networks are more than sets of nodes connected together and modellers must be aware that anatomical and morphological information could be key to a fuller understanding of brain functions.

Usually, the data-driven information needed to create the neuronal morphologies and the specific connection rules are given by the authors of the model or can be found on database repositories as `http://www.neuromorpho.org/`. Morphology files can be acquired by many different techniques and software, and it is common that files containing morphological information are in different formats such as Neurolucida (Glaser and Glaser, 1990), SWC (baptized after the researchers who worked on a system to reconstruct the three-dimensional morphology of neurons (Stockley et al., 1993)), and MorphML (Crook et al., 2007). The morphological data available in the neuromorpho repository goes through a process of standardization before being published in order to make the data available uniform and easily readable across platforms. In Fig 3.5(a) we show the content of a SWC file corresponding to a Purkinje cell from the mouse. In each row the file displays the information of a given neuronal segment and the columns contain the following information from left to right: segment index, segment type, the coordinates x, y, z, the radius of the segment (in μm), and the parent segment. While the interpretation of most of those properties is straightforward, the segment type and parent deserve further explanation. The segment type encodes which neuronal structure the segment represents as follows: soma $= 1$, axon $= 2$, (basal) dendrite $= 3$, apical dendrite $= 4$, and custom $= 5+$. The first segment of the SWC file is always a soma. Notice that a given structure can be composed of many segments as the soma in Fig 3.5(a). The parent indicates the segment index i at which the segment j connects from, the first segment of the file must have parent value equal to -1, and for the subsequent segments the parent segment must always have a value smaller than that of the "child" segment.

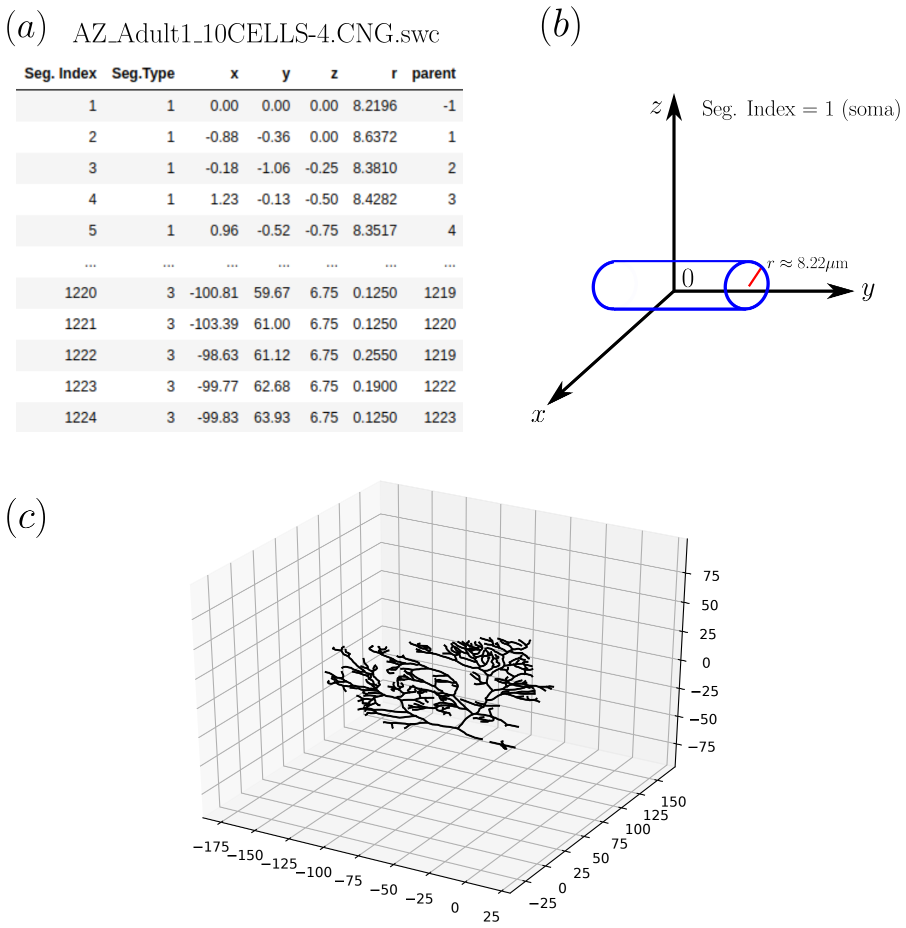

(a) AZ_Adult1_10CELLS-4.CNG.swc

Seg. Index	Seg.Type	x	y	z	r	parent
1	1	0.00	0.00	0.00	8.2196	-1
2	1	-0.88	-0.36	0.00	8.6372	1
3	1	-0.18	-1.06	-0.25	8.3810	2
4	1	1.23	-0.13	-0.50	8.4282	3
5	1	0.96	-0.52	-0.75	8.3517	4
...	...	...	...	...	...	...
1220	3	-100.81	59.67	6.75	0.1250	1219
1221	3	-103.39	61.00	6.75	0.1250	1220
1222	3	-98.63	61.12	6.75	0.2550	1219
1223	3	-99.77	62.68	6.75	0.1900	1222
1224	3	-99.83	63.93	6.75	0.1250	1223

Figura 3.5: ***Morphology using SWC files.*** *In (a) we show the content of the file AZ_Adult1_10CELLS-4.CNG.swc obtained from neuromorpho corresponding to a mouse Purkinje cell. In (b) we depict the geometrical representation of the first segment (soma) from the same SWC file. In (c) we show a plot the cell morphology using the NEURON simulator.*

Once the cell morphologies are implemented and the neurons are positioned in the spatial grid, one possibility for connecting them is to create connections between pairs of neurons according to the spatial intersections among presynaptic axons and postsynaptic dendrites. Additionally, the same distance-dependent connectivity rules discussed for point-neuron networks can be applied using the somata as reference points. It is important to note that processes (axon and dendrites) emanating from different neurons reach distinct distances. Some neurons make mostly local connections while other make both local and long-range contacts, and this can be taken into account in a distance-dependent way by setting distinct zones with predefined radii centered on reference points, e.g. somata, and allowing specific synaptic types to be created exclusively within such zones. After defining the existence of connections between pairs of neurons, the next step is to define the number of synapses and how they are distributed in their allocated zones. When there is not much information about synaptic positions, one strategy is to use a known distribution (e.g. uniform, Gaussian, etc.) and randomly place the synapses within the predefined zone of the postsynaptic dendritic tree until the maximum number of connections is attained. It is also known that specific neuron types tend to concentrate their received synapses on specific regions of their dendritic trees, and this information must be used to create a more biologically faithful connectivity pattern.

Since implementing these characteristics from the scratch in a code is a laborious task, these models are commonly implemented using neurosimulators. For morphologically detailed neuron models, the most used neurosimulator is the NEURON simulator (Hines and Carnevale, 1997). For instance, SWC files can be easily loaded into NEURON. Once imported, each segment is represented as a cylinder as depicted in Fig 3.5(b). The morphology can be visualized by means of the NEURON graphical user interface (GUI) or by calling the PlotShape function in a Python (or HOC, the original NEURON programming language) script. In Fig 3.5(c) we show a plot of the whole morphology of the Purkinje cell loaded from the SWC file. Besides NEURON, there are other tools to load cell morphologies. An example is NeuroConstruct (Gleeson et al., 2007), in which not only it is possible to load different types of morphology files but also to generate scripts compatible with different simulators such as NEURON, GENESIS (Bower and Beeman, 2012; Crone et al., 2019), MOOSE (Bhalla, 2008; Ray et al., 2008), PSICS (Cannon et al., 2010) and PyNN (Davison et al., 2009). NEURON and other simulation environments will be better discussed in the next subsection.

Surely, there is not a unique method for building complex neuronal networks as different biological details may be modeled in distinct ways. In this subsection, we gave examples of general approaches to implement the connectivity map into a neuronal network code. It is important to realize that extracting synapses from a connectivity map derived from data is not a trivial task and may deliver different results depending on the approach. Many of the models that are discussed in the next section were built following the methods discussed in this section.

3.6.3 Choosing a neurosimulator

Coding a model is a task that can be approached by low or high level programming languages. Many computational neuroscientists prefer to develop their own codes in low level languages such as C/C++, or Fortran. In higher level languages the syntax is more human readable and simpler to debug, as is the example of MATLAB (The MathWorks Inc., Natick, USA) which can be used as it is or coupled to packages for neuronal simulation (Heitmann et al., 2018). While low level languages offer the advantage that the commands are closer to the processor instructions, dealing with complex data and complex syntax is not an easy task. Higher level languages ultimately make the models more accessible to the scientific community by using a more unified syntax, which facilitates information sharing and reproducibility (Nordlie et al., 2009; McDougal et al., 2016). In this section, we present some of the most popular neurosimulators, which are high level packages developed with the sole purpose of neural modeling. We also discuss differences among them that should be taken into account when choosing the one to use.

In recent years, Python has become a standard programming language in many research areas due to its high productivity and interpretability. As a consequence, packages for many research fields such as astronomy (Robitaille et al., 2013), network analysis (Hagberg et al., 2008), machine learning (Pedregosa Gael Varoquaux Alexandre Gramfort Vincent Michel Bertrand Thirion et al., 2011; Paszke et al., 2019), and neuroscience (Muller et al., 2015) are available for the scientific community. For computational neuroscience, in particular, many Python packages – henceforth addressed to as neurosimulators – can be used for the *in silico* implementation of network models.

We discuss three neurosimulators which are available in Python: Brian 2 (Stimberg et al., 2019), NEST (Eppler et al., 2009), and NEURON (Hines et al., 2009). As discussed in Section 3.4 the single neuron model can be classified as simplified or conductance-based, and can have morphology or not. When choosing a neurosimulator, one should first define in which of these categories the adopted model fits in.

The neurosimulator Brian 2 was developed to be used in Python (Stimberg et al., 2019). Although its main focus is on point neurons, Brian 2 also offers the possibility of defining cells with morphologies. A useful feature of Brian 2 is that it allows the user to define the ordinary differential equations (ODEs) of the model, so it is possible to describe both simplified or conductance-based models in the package. However, since the number of ODEs increases rapidly with the number of ionic channels modeled, Brian 2 is not very practical for detailed conductance-based models as the computational cost of implementing them increases rapidly.

NEST (Eppler et al., 2009) constitutes another option for modeling large-scale networks of point neurons. Instead of allowing the user to define the ODEs of the model as in Brian 2, NEST has pre-implemented models available and the user only imports them. This is convenient for its practicality, but can be a problem if the model requires some mechanism that is not pre-implemented. For that, the user is either required to work with the NEST source code in C/C++ or use a software called NESTML which implements different models for NEST (Plotnikov et al., 2016). Both Brian 2 and NEST offer support to run the model in parallel, although only NEST offers message parsing interface (MPI) support. Because of that, NEST is more appropriate for large-scale models and is compatible with high-performance computing allowing a simulation to run across many compute nodes (Peyser and Schenck, 2015; Tikidji-Hamburyan et al., 2017).

Finally, the NEURON simulator (Hines et al., 2009) is the alternative of choice for modeling neurons with morphology and networks made of them. In NEURON, a morphology is represented by a series of cylindrical compartments connected to each other, and even a single-compartment neuron with only a soma has a geometric representation with surface area and length. Even though one can adopt a simplified approach to model the compartment dynamics, the NEURON simulator works optimally with biophysical models where several ionic currents can be easily added to a neuron model. The simulator already has many ionic mechanisms implemented, such as the classic fast sodium and delayed rectifier potassium channels of the Hodgkin-Huxley model (Hodgkin and Huxley, 1952) and many others, which can be found in databases such as modelDB (Hines et al., 2004). If a specific ionic mechanism is needed, it can be programmed as a ".mod" file; however, this is a low level language and can be a nuisance for less experienced users. Despite the practicality of implementing morphological models in NEURON, building neuronal networks can be very challenging using this neurosimulator. In this regard, it is possible to use packages that work on top of NEURON such as NetPyne (Dura-Bernal et al., 2019), Brain Modeling Toolkit (BMTK) (Dai et al., 2020), or BioNet (Gratiy et al., 2018) to construct large-scale networks that can be efficiently run in parallel using NEURON.

Many other packages for computational neuroscience are available, some of them, such as PyNN (Davison et al., 2009), even try to integrate Brian 2, NEST, and NEURON. A complete characterization of the different neurosimulators available would be out of the scope of the present review; for this, we recommend the reader to see (Tikidji-Hamburyan et al., 2017; Blundell et al., 2018). Several efforts have also been undertaken in recent years to promote code sharing and reproducibility in computational neuroscience (Nordlie et al., 2009; Gutzen et al., 2018; McDougal et al., 2016; Miłkowski et al., 2018; Crook et al., 2020). We emphasize the existence of repositories such as ModelDB (McDougal et al., 2017) and journals dedicated to the replication of computational work such as the ReScience Journal (Rougier et al., 2017), which are important steps towards transparency in science.

Chapter 4

The thalamocortical microcircuit model

This chapter describes the implementation of the thalamocortical model of spiking neurons and analyzes its spontaneous activity. With this study, we set the free parameters of the model and the possible dynamics presented by the network. This step is crucial to have a valid model behaving similarly to experimental data. Then, in the next chapter, we use this model to analyze the possible alpha rhythm generation mechanisms.

4.1 Spontaneous activity and observed emergent phenomena

The cerebral cortex displays specific patterns of spontaneous activity produced endogenously. These states are characterized with respect to the degree of synchrony of the collective neuronal activity and the level of irregularity of action potential spikes of individual neurons. A problem posed to theoretical neuroscience is how to model the emergence of synchronous and asynchronous spontaneous states from the same network of spiking neurons. In Shimoura et al. (2021), three models that offer solutions to this problem are reviewed by us. The models use spiking neurons of the class known as integrate-and-fire and consider different network structures and synaptic dynamics. Mechanisms adopted by the models, like balance between excitation and inhibition and spiking-dependent adaptation, are discussed and contextualized in the article.

One of the best ways to study the neocortex electrical activity and dynamics is to consider situations where the system is isolated from external stimuli. The activity generated by the neocortex under these conditions is called spontaneous activity. It is measured in (i) *in vitro* preparations of neocortical tissue slices (Sanchez-Vives and McCormick, 2000; Mao et al., 2001; Cossart et al., 2003; Shu et al., 2003); (ii) *in vitro* cultures of neocortical circuits (Plenz and Aertsen, 1996; Wagenaar et al., 2006); and (iii) *in vivo* preparations of cortical plaques (slices) (Timofeev et al., 2000; Lemieux et al., 2014). It is also considered a spontaneous activity that produced by neocortical neurons when the subject is essentially disconnected from the outside world, such as in slow-wave sleep and anesthesia (Steriade et al., 2001).

Until a few years ago, spontaneous cortical activity used to be treated as "noise" by neuroscientists, who were more interested in the so-called activity evoked by external stimuli. However, recent experimental evidence has shown that the activity intrinsically generated by the neocortex has a rich spatiotemporal structure that interacts and modulates the brain's response to environmental stimuli (Ringach, 2009; Berkes et al., 2011; Deco and Jirsa, 2012; Stringer et al., 2019). There is also evidence to suggest that spontaneous cortical activity determines the moment of decision making in non-motivated decision situations (Schurger et al., 2012).

Electrophysiological studies with the different preparations mentioned above reveal that spontaneous neocortical activity has essentially the same basic characteristics (Steriade et al., 1993; Sanchez-Vives and McCormick, 2000; Mao et al., 2001; Cossart et al., 2003; Shu et al., 2003; Steriade et al., 2001): slow and high-amplitude oscillations of collective network activity, consisting of periods of high activity (called "up" states) interspersed with periods of very low activity (called "down" states). During the up states, neurons tend to be "depolarized", that is, the average of their membrane potentials is above the resting value, close to the firing threshold; in the down states, neurons tend to be "hyperpolarized", that is, the average of their membrane potentials is below the resting value (Steriade et al., 1993; Luczak et al., 2007; Jercog et al., 2017). In contrast, in awake states, the collective activity is asynchronous, has low amplitude and the membrane potential of neurons fluctuates irregularly around the equilibrium value (El Boustani et al., 2007). These two modes of operation are often called "synchronous" and "asynchronous" states

(Harris and Thiele, 2011).

It is conjectured that the asynchronous activity characteristic of waking states reflects the availability of a larger and more diversified repertoire of neural patterns, enabling the existence of rich states of consciousness, while the reduced repertoire of neural patterns during regimes of synchronous collective activity restricts consciousness (Tononi et al., 1998; Sitt et al., 2014; Goldman et al., 2019).

This experimental evidence raises, among others, two questions (Latham et al., 2000; Compte et al., 2003; Holcman and Tsodyks, 2006; Parga and Abbott, 2007; Mattia and Sanchez-Vives, 2012; Levenstein et al., 2019): (i) How the same set of neurons can generate an oscillatory population activity pattern (synchronized state) and an activity pattern approximately constant population (out of sync state)? (ii) what are the mechanisms responsible for the depolarized and hyperpolarized states of individual neurons during the synchronized regime?

The most accepted hypothesis to explain the origin of synchronous and asynchronous states in the same neural network is that these states depend on the relative strength between the inhibitory and excitatory synapses of the neurons on the network (Van Vreeswijk and Sompolinsky, 1996; Amit and Brunel, 1997; Van Vreeswijk and Sompolinsky, 1998; Renart et al., 2010; Landau et al., 2016). Network models based on the so-called leaky integrate-and-fire (LIF) neuron show that in the "balanced" state, the strength of the inhibitory synapses is approximately four times greater than that of excitatory synapses (since there are approximately four times more excitatory neurons in the neocortex than inhibitory neurons), the network activity resembles that of the desynchronized cortical state. In the absence of this balance, the behavior of the network is similar to that of the synchronized cortical state (Brunel, 2000; Vogels et al., 2005; Vogels and Abbott, 2005; Kumar et al., 2008; Wang, 2011; Litwin-Kumar and Doiron, 2012; Kriener et al., 2014; Ostojic, 2014; Potjans and Diesmann, 2014).

Models that use, instead of the LIF neuron, nonlinear integrate-and-fire neurons with an adaptive variable, such as the Izhikevich (Izhikevich, 2003, 2007) and AdEx (Gerstner et al., 2014; Brette and Gerstner, 2005a) models, are able to capture the phenomenon of spontaneous alternation between up and down states (Destexhe, 2009; Tomov et al., 2014b, 2016b; Pena et al., 2018a). This suggests that it is not only the balance between excitation and inhibition that is responsible for the emergence of cortical states but also the intrinsic dynamics of the neurons that compose the network.

Since the alpha rhythm occurs during the awake state, the features highlighted here and involved in the cortical spontaneous activity dynamics is the starting point used to validate the computational network model presented in the following sections.

4.2 Network structure

The cortical network is full-scaled and data-driven based focusing mainly on two characteristics: multi-layered structure and one-to-one mapping. The first feature that is needed to test the hypothesis of alpha oscillation which involves the possible generation and transmission from different cortical layers. The second aims to keep second order statistics that may affect the oscillatory dynamics (van Albada et al., 2015). Further details about the cortical and thalamic networks are given in the next subsections.

Figure 4.1 shows a network scheme with the main excitatory and inhibitory connections represented by blue and red arrows respectively and blue triangles representing excitatory populations and red balls the inhibitory ones.

All computational models here described were built using the NEST simulator (Gewaltig and Diesmann, 2007; Peyser et al., 2017) version 2.18.0 (Jordan et al., 2019) and the codes ran with Python using the PyNEST interface.

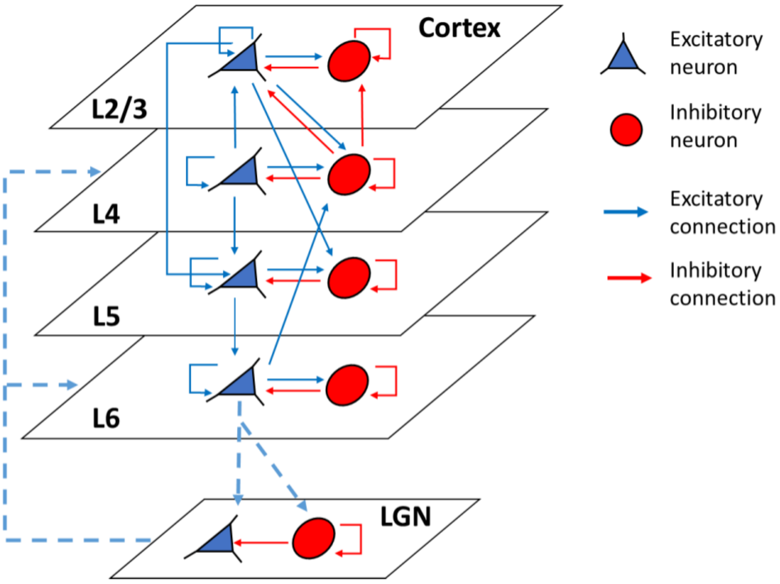

Figura 4.1: ***Thalamocortical circuit schematic draw.*** *Schematic drawing with the main connections present in the thalamocortical model involving the V1 and the LGN. The 4 layers represented by L2/3, L4, L5 and L6 correspond to the cortical layers. In each layer there are two populations of neurons: the excitatory (blue triangles) and the inhibitory (red circles). The excitatory connections are illustrated by blue lines and the inhibitory connections by red lines. The arrows indicate the direction of the synapses. The network at the bottom of the figure represents the thalamus. The connections between the cortex and the thalamus are represented by dashed lines.*

4.2.1 Primary visual cortical microcircuitry

The cortical network structure described here is extracted from the multi-area spiking network model of macaque visual cortex developed at the Institute of Neuroscience and Medicine (INM-6), Research Center Jülich (Schmidt et al., 2018b,a). In fact, each microcircuit of this multi-area model was adapted from Potjans and Diesmann (2014) (here called as PD network), where they were adjusted in terms of number of neurons and connections accordingly with the representing area (e.g. V1, V2, etc).

The PD network, used as starting point, is based mainly on data from primary sensory areas of cat, rat, and mouse. It is a full-density network comprising neurons divided into eight populations: an excitatory and an inhibitory one in each of the four layers 2/3, 4, 5, and 6. Connection probabilities are population-specific, synapses were drawn randomly with replacement (thus allowing multiple connections between any given pair of neurons). The transmission delays are normally distributed with mean 0.75 ms for inhibitory source neurons and 1.5 ms for excitatory source neurons. The neurons each receive an independent excitatory Poisson drive with a population-specific rate reflecting input from surrounding cortex and from other areas. Both delays and Poisson inputs are restricted to the 0.1 ms simulation grid, and the minimum delay is 0.1 ms. See Potjans and Diesmann (2014) for further details and Shimoura et al. (2018) for a reimplementation in Brian2 simulator.

The main characteristics listed above are kept in the V1 microcircuit extracted from the multi-area network (Schmidt et al., 2018b,a). The multi-area model contains 32 different areas where each area is represented by a 1 mm^2 microcircuit and it combines information of connectivity and laminar thickness. For this work we used only the V1 network structure which contains 197,932 neurons divided in eight populations as in the PD network. The number of neurons by population is presented in Table 4.1.

L2/3e	L2/3i	L4e	L4i	L5e	L5i	L6e	L6i
47386	13366	70387	17597	20740	4554	19839	4063

Tabela 4.1: *Layer population sizes (extracted from (Schmidt et al., 2018a)). Neurons were distributed over four different layers (L2/3, L4, L5 and L6), and for each layer they were divided into excitatory (L2/3e, L4e, L5e and L6e) and inhibitory (L2/3i, L4i, L5i and L6i) subpopulations.*

The number of connections between two populations was also extracted from (Schmidt et al., 2018b) and are presented in Table 4.2.

The non-simulated areas were replaced by Poisson spike trains in two different ways: first by using Poisson spike trains with same firing rate and secondly by replacing the non-simulated areas by Poisson spike trains with specific firing rates corresponding to their average resting state activity when connected in the full multi-area model. These last values are also available together with the multi-area code.

The number of extra-cortical inputs coming from other sources are shown in Table 4.3. In the first approximation of the non-simulated areas described above, for each neuron a Poisson spike train was created with the rate defined as the

		Target							
		L23E	L23I	L4E	L4I	L5E	L5I	L6E	L6I
Source	L2/3e	50543166	19305855	5746303	12669824	21895109	2600251	3248691	1507824
	L2/3i	24492370	5530516	1214762	151689	3774955	356393	399610	11666
	L4e	22840238	4664990	38637674	15427501	11617260	1288710	4526037	131562
	L4i	10792756	1909143	26931567	8058448	336172	24572	914706	10956
	L5e	3660142	2458309	1178608	126104	4234192	666398	2754724	274203
	L5i	0	0	11066	0	4712098	854387	209401	17080
	L6e	2692458	379184	22799605	13736225	2958914	291230	5701957	1945265
	L6i	0	0	0	0	0	0	7056641	895354

Tabela 4.2: *Total number of synapses between two populations for the V1 microcircuit network. Rows represent the sources and columns represent the target population.*

	L2/3e	L2/3i	L4e	L4i	L5e	L5i	L6e	L6i
Intercortical inputs	1123	323	604	9	1712	297	757	464
External inputs	1246	1246	1246	1246	1246	1246	1246	1246
Total	2369	1569	1850	1255	2958	1543	2003	1710

Tabela 4.3: *Extra-cortical inputs coming from other cortical areas (Intercortical inputs) and from external sources (External inputs). The columns represent the number of inputs received by neuron in each population.*

background rate (bg_{rate}), which is chosen based on the spontaneous activity analyses in the Results section, times the row of Total in Table 4.3.

On the other hand, the second approximation of non-simulated areas, for each neuron a Poisson spike train was created with the rate defined as the bg_{rate} times the External inputs row in Table 4.3 plus the specific firing rates coming from other cortical areas defined in Table 4.4.

	L2/3e	L2/3i	L4e	L4i	L5e	L5i	L6e	L6i
Specific firing rates	231.40	61.09	114.74	0.24	341.75	56.72	141.24	89.18

Tabela 4.4: *The values represent the multiplication of the specific firing rate at resting state from each non-simulated cortical area times the number of connections between the non-simulated cortical area and V1.*

4.2.2 Thalamic network

For the thalamic part of our model, we started using the same number of thalamocortical neurons (TC) and connectivity as described in (Potjans and Diesmann, 2014). Thus, there are $N_{thal,E}$=902 projecting neurons to cortical layers 4 and 6. There are no intrathalamic connections among TC cells. The connectivity from TC to L6 neurons was kept the same but the connectivity from TC to L4 neurons was updated based on recent studies done on primary visual cortex in primates. These studies estimated the number of thalamocortical connections per L4 cortical neuron and they calculated 8 afferent neurons with 25 synapses/neuron, totalling 200 connections from TC cells to a single neuron in L4 (Garcia-Marin et al., 2017). So, we used this value and for each L4 cell we connected 8 TC neurons with 25 multapses.

Data from the ventral nucleus of medial geniculate body (the primary auditory relay) of cat suggest that thalamic relay neurons each receive around 9100 synapses (Serkov and Gonchar, 1995). In the LGN, about 25% of these are of cortical origin and the same percentage comes from brainstem (Erisir et al., 1997). Considering this information we approximated the number of synapses per thalamic neuron received from cortical L6 as $N_{cth} = 2275$. Thus, we calculated the connection probability from L6e to TC cells $C_{L6e \to TC}$ using values from (Potjans and Diesmann, 2014), resulting in $C_{L6e \to TC} = 0.1461$. Then we use this connection probability to create corticothalamic synapses of our network.

In addition to the projection neurons, the thalamus contains 25% inhibitory interneurons (IN) ($N_{thal,I} = 301$) (LeVay and Ferster, 1979; Fitzpatrick et al., 1984; Arcelli et al., 1997; Çavdar et al., 2014; Madarász et al., 1985). For simplicity, connections from IN to IN and from IN to TC neurons have connectivity probability close to 1.

4.3 Neuron model

4.3.1 Integrate and fire model

The LIF model is described in equation 4.1 and was used only in the initial simulations aiming to test our codes and make a comparison with the reference work

(Schmidt et al., 2018a,b).

$$\frac{dV_i}{dt} = -\frac{(V_i - E_L)}{\tau} + \frac{I_i(t) + I_{ext}}{C_m} \tag{4.1}$$

$$\tau_s \frac{dI_s}{dt} = -I_s + \tau_s \sum_j J_{ij} s_j(t - d), \tag{4.2}$$

where V_i is the membrane potential of neuron i, E_L the resting membrane potential, C_m the membrane capacitance and τ the membrane time constant. A spike occurs when V_i reaches the threshold potential V_{th}. For each occurrence of a spike in neuron i, V_i is set to V_r.

C_m[pF]	E_L[mV]	V_{th} [mV]	τ_m [ms]	τ_{ref} [ms]	V_r[mV]	τ_s [ms]
250.0	-65.0	-50.0	10.0	2.0	-65.0	0.5

Tabela 4.5: *Parameters used in LIF neuron model for cortical neurons. The values were extracted from Potjans and Diesmann (2014).*

Equation 4.2 describes the time evolution of current based synaptic model used, where I_s is the total synaptic current varying in time t, d is the transmission delay (d_e for excitatory and d_i for inhibitory neurons), τ_s is the synaptic time constant, J_{ij} are the amplitudes of the synaptic currents, and $s_j = \sum_k \delta(t - t_k^j)$ are the spike trains sent by neurons j. I_{ext} is the external current, which in this work is set to zero unless specified. The transmission delays were normally distributed with means $d_e = 1.5 \pm 0.75$ ms and $d_i = 0.75 \pm 0.375$ ms for cortico-cortical connections.

4.3.2 Adaptive exponential integrate and fire model

The neuron model choice for this work aimed the electrophysiological properties such as spike frequency adaptation (SFA), inhibitory rebound spikes and intrinsic oscillatory behavior. Therefore, we used point neurons focusing on these phenomenological properties rather than model the neuronal morphological details.

As mentioned in Section 3.4, two-dimensional integrate-and-fire models are capable to reproduce a rich repertoire of neuronal firing patterns including the ones needed for the hypothesis being considered here. Thus, it was chosen the Adaptive

Exponential Integrate-and-Fire (AdEx) model (Naud et al., 2008; Gerstner and Brette, 2009; Brette and Gerstner, 2005b) which is described by equations 4.3-4.4.

$$C_m \frac{dV_i}{dt} = -g_L(V_i - E_L) + g_L \Delta_T \exp(\frac{V_i - V_{th}}{\Delta_T}) - w_i + I_i(t) + I_{ext} \tag{4.3}$$

$$\tau_w \frac{dw}{dt} = a(V_i - E_L) - w \tag{4.4}$$

where V_i is the membrane potential of neuron i, w_i the adaptation variable, C_m the membrane capacitance, g_L the leak conductance, E_L the leak reversal potential and Δ_T the slope factor. When V_i crosses the threshold potential V_{th}, neuron i produces a spike and V_i is clamped to a reset potential V_r for a refractory time τ_{ref}. The adaptation variable w_i decays with a adaptation time constant τ_w, and the adaptation coupling parameter is represented by a. For each occurrence of a spike in neuron i, w_i is incremented by b, which represents the variable regulating the adaptation strength. I_{ext} is the external current, which in this work is set to zero unless specified. The time evolution of the current based synaptic model used I_s is defined by

$$\frac{dI_s}{dt} = -I_s + \tau_s \sum_j J_{ij} s_j(t - d) \tag{4.5}$$

where I_s is the total synaptic current varying in time t, d is the transmission delay (d_e for excitatory and d_i for inhibitory neurons), τ_s ($\tau_{se} = 1.0$ for excitatory and $\tau_{si} = 2.0$ for inhibitory synapses) is the synaptic time constant, $J_{ij}(t)$ are the amplitudes of the synaptic currents, and $s_j = \sum_k \delta(t - t_k^j)$ are the spike trains sent by neurons j. The transmission delays were normally distributed with means $d_e = 1.0 \pm 0.75$ ms and $d_i = 0.75 \pm 0.375$ ms for corticocortical connections.

It is important to note that neurons with different capacitance values receiving same presynaptic current or a current pulse with same amplitude will have different postsynaptic potentials. In other words, to have similar excitatory/inhibitory postsynaptic potentials the capacitance value of the postsynaptic neuron must be taken into account. In that way, the excitatory synaptic strength (w_{ex}) was defined to induce an excitatory postsynaptic potencial

(EPSP) around 0.15 mV (Fetz et al., 1991). Inhibitory synaptic strength is defined as $w_{in}= g.w_{ex}$, where g represents the balance between excitation and inhibition. The value of g was varied and its effect analysed in the Results section.

The AdEx parameters values used for the cortical network are shown in Table 5.1. The values chosen for RS and FS neurons were adapted from (Destexhe, 2009), where they represent qualitatively two main excitatory (RS) and inhibitory (FS) electrophysiological classes present in cortex. FS parameters are the same as in the source, but RS was adapted in a way that the curve of firing rate evoked by constant current input is more biological fashion as can be seen in Figure 4.2c.

	C_m[pF]	g_L[nS]	E_L[mV]	Δ_T[mV]	V_{th}[mV]	τ_{ref}[ms]	τ_w[ms]	V_r[mV]	a[nS]	b[pA]
RS	200.0	10.0	-60.0	2.5	-56.0	2.5	600.0	-60.0	1.0	20.0
FS	200.0	10.0	-60.0	2.5	-50.0	2.5	600.0	-60.0	1.0	0.0

Tabela 4.6: *Parameters used in AdEx neuron model for cortical neurons. The values of RS and FS were adapted from (Destexhe, 2009).*

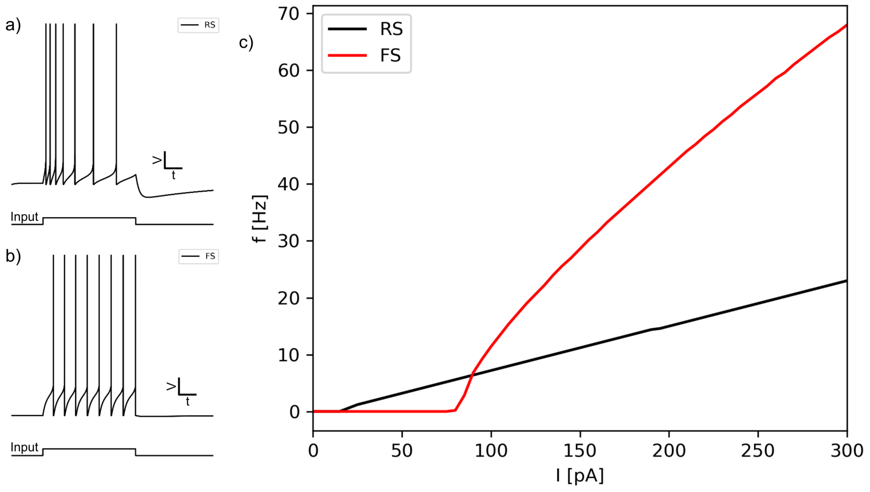

Figura 4.2: ***Firing patterns of the main cortical neurons simulated by AdEx model****. a) and b) are representative membrane voltage responses in time for RS and FS neurons respectively when stimulated by the same square pulse. In c) are the curves of firing rate versus current amplitude for RS (black line) FS (red line) neurons.*

For thalamic AdEx parameters (Table 4.7 we used the same reference as mentioned for cortical neurons (Destexhe, 2009). The parameters were kept as in

(Destexhe, 2009), for the excitatory thalamocortical (TC) neurons and, based on this set, we adapted them to simulate the inhibitory ones. Thalamic inhibitory interneurons (IN) present fewer rebound spikes when stimulated by hyperpolarizing input (see Figure 4.3).

	C_m[pF]	g_L[nS]	E_L[mV]	Δ_T[mV]	V_{th}[mV]	τ_{ref}[ms]	τ_w[ms]	V_r[mV]	a[nS]	b[pA]
TC	200.0	5.0	-60.0	2.5	-50.0	2.5	600.0	-60.0	5.0	0.0
IN	300.0	5.0	-60.0	2.5	-50.0	2.5	600.0	-60.0	5.0	0.0

Tabela 4.7: *Parameters used in AdEx neuron model for thalamic neurons. TC parameters were copied from (Destexhe, 2009) and the IN parameters were adjusted to be qualitatively similar with experimental electrophysiologic records.*

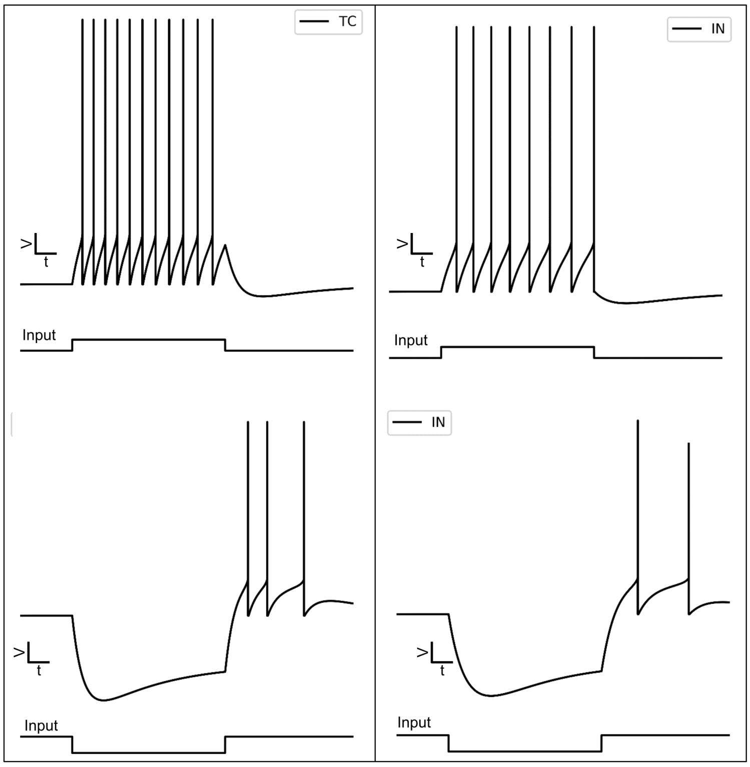

Figura 4.3: ***Thalamic neurons responses***. *Membrane potential response of LGN neurons when stimulated by a depolarizing (top) and hyperpolarizing (bottom) square current input. Left: thalamocortical (TC) cells. Right: thalamic inhibitory (IN) cells.*

Besides the neuron parameters, thalamocortical and corticothalamical EPSPs were set to 0.4 mV. The transmission delays within LGN connections were kept the same as defined for the cortical network. Further, thalamocortical and corticothalamic transmission delays (d_{thc} and d_{cth}) sum was kept in 80 ms with both values varying accordingly with the protocol described in the next section.

4.4 Simulation protocols

Spontaneous activity of the cortical microcircuit

The first step used in this work to validate the cortical model dynamics was looking into its spontaneous activity and comparing with experimental data. For this purpose the microcircuit described in Section 4.2 was evaluated for different combinations of two parameters: the balance between excitatory and inhibitory synaptic strength (g) and the background rate (bg_{rate}).

The criteria adopted to check if the network activity was comparable with in vitro and in vivo experiments were those described in (Maksimov et al., 2018).

4.5 Measures and analysis

To analyse the network activity, the spike trains were stored from simulations. From these data we characterized and investigate the emergent dynamics.

The analyses were performed using Python packages.

4.5.1 Spike count and irregularity

Some very common metrics used to characterize neuronal activity are firing rate (ν), interspike interval (ISI), coefficient of variation (CV) and local variation (LV).

The firing rate (ν) is the number of spikes counted in a window of time for a single spike train or averaged for a group of spike trains.

The ISI is simply the time between two consecutive action potential of a neuron (T_i). From the distribution of ISIs ($T_1, T_2, ..., T_n$) of a spike train it is possible to know how regular a neuron is spiking by estimating its CV and LV. The $CV(ISI)$ is obtained by equation 4.6.

$$CV = \frac{\sigma_T}{\langle T \rangle} \tag{4.6}$$

where σ_T is the ISI standard deviation and $\langle T \rangle$ the average of ISI distribution.

Poisson processes result in $CV = 1$, while $CV > 1$ indicates that the neuron spike train is less regular than a Poisson process and $CV < 1$ indicates more regularity. Models like the leaky integrate-and-fire (LIF) model fire periodically when driven by a constant input resulting in $CV = 0$. On the other hand, intrinsically bursting neurons can have $CV > 1$ (Gerstner et al., 2014). The CV is also referred in this work as the irregularity measure.

The local variation LV, introduced by (Shinomoto et al., 2003), is defined as

$$LV = \frac{1}{n-1} \sum_{i=1}^{n-1} \frac{3(T_i - T_{i+1})^2}{(T_i + T_{i+1})^2} \tag{4.7}$$

Both CV and LV result in 1 for a sufficiently long Poisson ISI sequence and go to zero when the ISI is regular. Nonetheless, whereas CV detects a global variability of the ISI sequence and is sensitive to firing rate fluctuations, LV detects local stepwise variability of ISIs and extracts firing characteristics intrinsic to individual neurons even for cases with modulations in firing rates (Shinomoto et al., 2003, 2005).

4.5.2 Multitaper spectral analysis

In order to estimate the spectral analysis of a given output we have to address two main issues: 1) to describe a system in the frequency domain, in principle, it is necessary to have an infinite length sample of the output of the system; 2) to capture intrinsic stochastic properties of the system, many realizations of the output are required. However, in many cases, it is only possible to have a small number of realizations with finite length. A nonparametric method capable of addressing bias and variance issues simultaneously is the multitaper spectral estimation technique introduced by (Thomson, 1982).

To estimate the average power spectrum and cross-spectrum using this method the time series from each trial have to be first multiplied by orthogonal tapers, then Fourier-transformed and the resulting transforms are cross-multiplied and averaged over individual tapers (Mitra and Pesaran, 1999; Percival and Walden, 1993). If we consider two time series $X_1(t)$ and $X_2(t)$, the multitaper cross-spectrum estimator between them $S_{12}(f)$ at frequency f is given by:

$$S_{12}(f) = X_1(f)X_2^*(f) = \frac{\Delta}{K}\Sigma_{k=1}^{K}\left((\Sigma_{s=1}^{N} w_s(k)x_{1s}e^{-i2\pi fs\Delta})(\Sigma_{t=1}^{N} w_t(k)x_{2t}e^{i2\pi ft\Delta})\right) \tag{4.8}$$

where $w(k)(k = 1, 2, ..., K)$ are K orthogonal tapers of length N given by discrete prolate spheroidal sequences (DPSS), also known as Slepian sequences (Slepian and Pollak, 1961; Slepian, 1978) and Δ is the sampling interval. Another important parameter is the product between N and the bandwidth W, the NW is the time-bandwidth product which regulates the trade-off between variance and bias of the spectral estimates. Increasing NW produces a decrease in variance, but also an increase in spectral leakage and bias of the spectral estimate; the opposite happens when NW is decreased.

The spiking activity in time used to estimate the power spectra were calculated in this work by summing the number of spikes that occurred in time windows of 1 ms as the default unless otherwise mentioned. These analysis were done in Python language and the multitaper spectral estimation was calculated using the MNE-Python package (Gramfort et al., 2013).

4.6 Results

4.6.1 Fast oscillations in cortical neuronal activity

The PD network exhibits extremely fast oscillations at around 300 Hz visible in the spike raster plot as vertical stripes and present as a peak in the power spectrum (Figure 1E showed in Bos et al. (2016)). However, while there are observed data of transient oscillations at 300 Hz (e.g. spontaneous neocortical ripples, pathological activity) (Buzsáki et al., 2012; Kandel and Buzsáki, 1997; Bragin et al., 1999; Staba and Bragin, 2011; Worrell and Gotman, 2011), there is little evidence for such sustained oscillatory behavior of the neural activity at this same range (Whittington et al., 2000; Kopell et al., 2000; Buzsaki and Draguhn, 2004). To figure out if the extremely fast oscillations result of an overlook in experimental data or if they only exist due to specific properties of the network model a study is being done by Helin et al. (2019); Essink et al. (2020). To contribute with this study we analysed if the same happened to the isolated V1 described in section 4.2.1.

We analyzed the model with LIF neurons as in the original work (Schmidt et al., 2018a,b) to assure that the effect is due to the change in how the non-simulated areas were replaced rather the influence by using neurons with distinct firing patterns.

Figures 4.4 and 4.5 show the raster plot, firing rate and power spectra calculated from network spiking activity for the isolated V1 with non-simulated areas replaced by homogeneous Poisson spike trains and with non-simulated areas replaced by Poisson spike trains with specific firing rates respectively. All the other neuron and network parameters are the same as used by (Schmidt et al., 2018a,b).

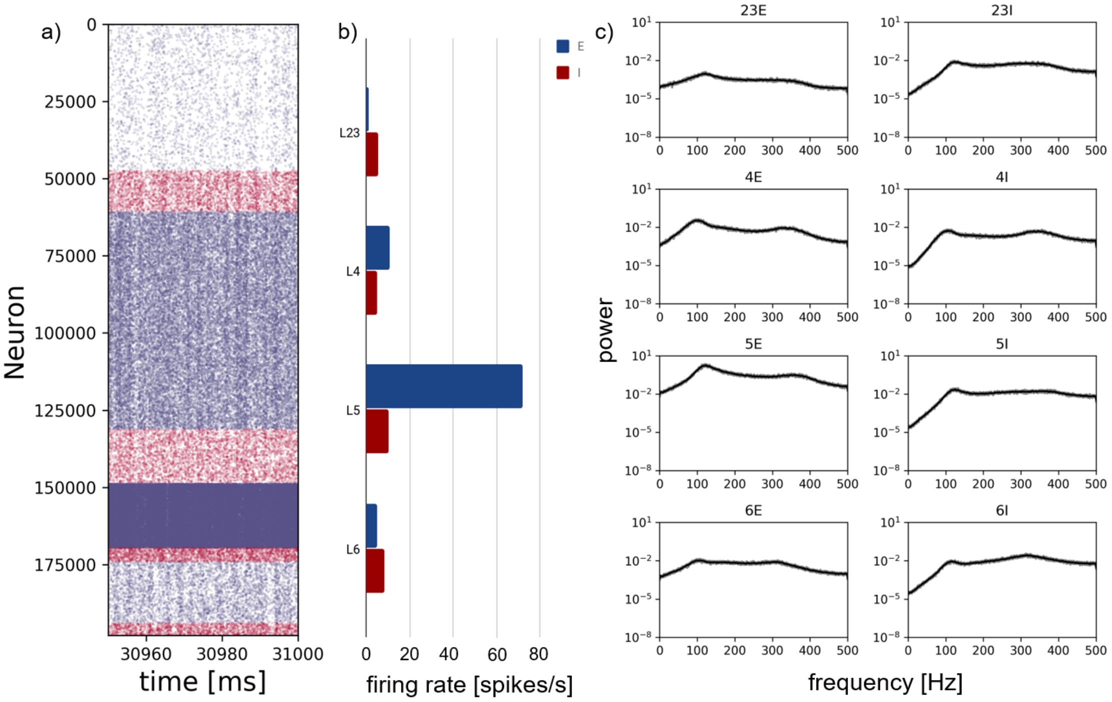

Figura 4.4: ***Spontaneous activity of the isolated V1 network when replacing the non-simulated areas by homogeneous Poisson spike train.*** *a) Raster plot of the full cortical network (all 197.932 neurons) with dots indicating spiking times for each neuron represented in rows. Blue dots refer to excitatory neurons and red to inhibitory ones. From top to bottom layers L2/3 to L6 are shown in sequence. b) Averaged firing rate per population. The colors mirror the same pattern in a). c) Power spectra estimated from population spiking activity.*

It is possible to observe in Figure 4.4 that there are peaks at the very high frequency, but they are much smaller than in the PD network (Bos et al., 2016; Helin et al., 2019; Essink et al., 2020). This fact is indicated by the absence of prominent vertical stripes in the raster plot. Nevertheless, the distribution of firing rates by layer became less biologically plausible with L5e firing more than 60 spikes/s.

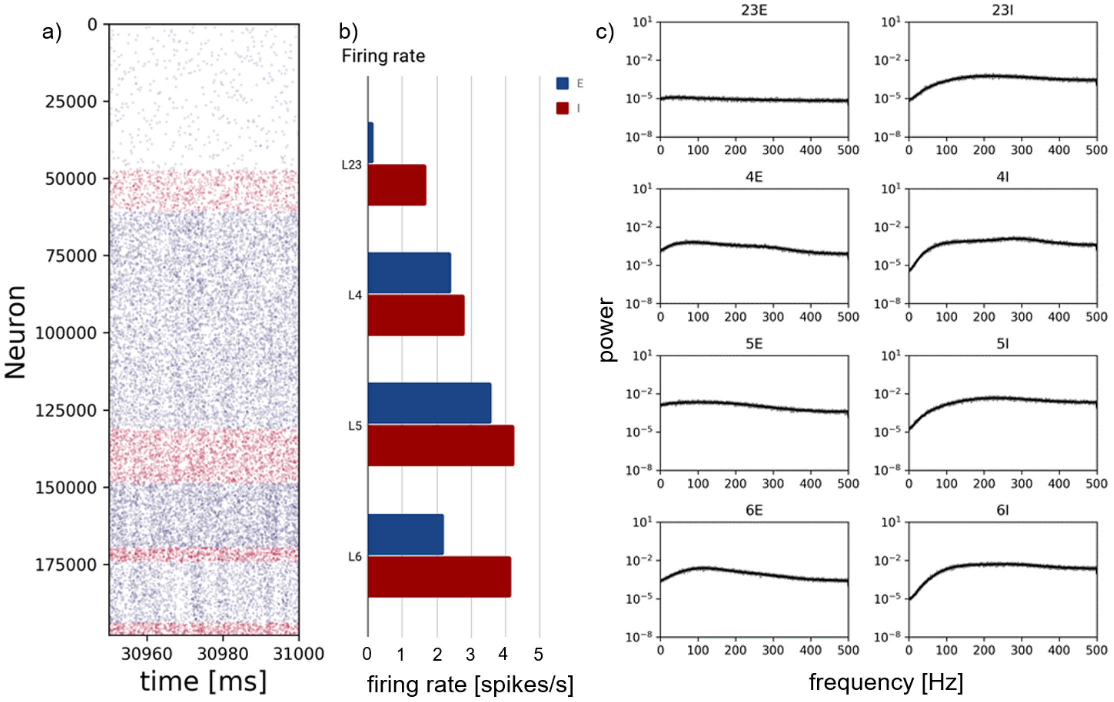

Figura 4.5: ***Spontaneous activity of the isolated V1 network when replacing the non-simulated areas by Poisson spike trains with specific firing rate.*** *a) Raster plot of the full cortical network (all 197.932 neurons) with dots indicating spiking times for each neuron represented in rows. Blue dots refer to excitatory neurons and red to inhibitory ones. From top to bottom layers L2/3 to L6 are shown in sequence. b) Averaged firing rate per population. The colors mirror the same pattern in a). c) Power spectra estimated from population spiking activity.*

On the other hand, Figure 4.5a shows a sparse activity with no visible vertical stripes. Moreover, the firing rates (4.5b) are very low in comparison with figure 4.4b and there are no visible peaks at any specific frequency in the power spectra in Figure 4.5c.

These results are reliable and were qualitatively replicated in next section using different neurons, showing the independence of these effects by the neuron model.

4.6.2 Spontaneous activity

After looking the original models in last section and analysing the reduction of the fast oscillations, we studied how changes, such as the excitatory and inhibitory balance, would affect the spontaneous activity.

First we built the multi-layered V1 microcircuit model based on previous studies (Schmidt et al., 2018b,a; Potjans and Diesmann, 2014). The network is divided in four layers, each layer contains an excitatory and an inhibitory population of adaptive exponential integrate-and-fire neurons (AdEx) (Brette and Gerstner, 2005b; Gerstner and Brette, 2009). The AdEx parameters were adjusted such that the neurons present firing patterns similar to the two major electrophysiological classes present in the cortex: the regular spiking (RS) for the excitatory neurons; and the fast spiking (FS) for the inhibitory neurons (Castro-Alamancos and Connors, 1997; Naud et al., 2008).

Besides that, the network model has two free parameters crucial for its dynamics: the balance between excitation and inhibition represented here by the ratio between the inhibitory synaptic weight and the excitatory synaptic weight (g); and the background activity simulated by Poisson spike trains with rate bg_{rate}. The latter represents the non-simulated areas including corticocortical connections and other external sources of input. To account for the different number of inputs coming from the other cortical areas we tested two possibilities: the first one by considering specific number of inputs by population with the same bg_{rate}, and the second one by keeping the same bg_{rate} for the external inputs plus considering the specific mean firing rates of each non-simulated cortical area at the resting state according to (Schmidt et al., 2018b).

Initially we analyzed what combinations of parameters g and bg_{rate} of the isolated V1 microcircuit resulted in a biological plausible network behavior. In the first case the external inputs and corticocortical connections coming from different regions were replaced by Poisson spike trains with the same bg_{rate}. The result of this parameter scan is shown in Figure 4.6.

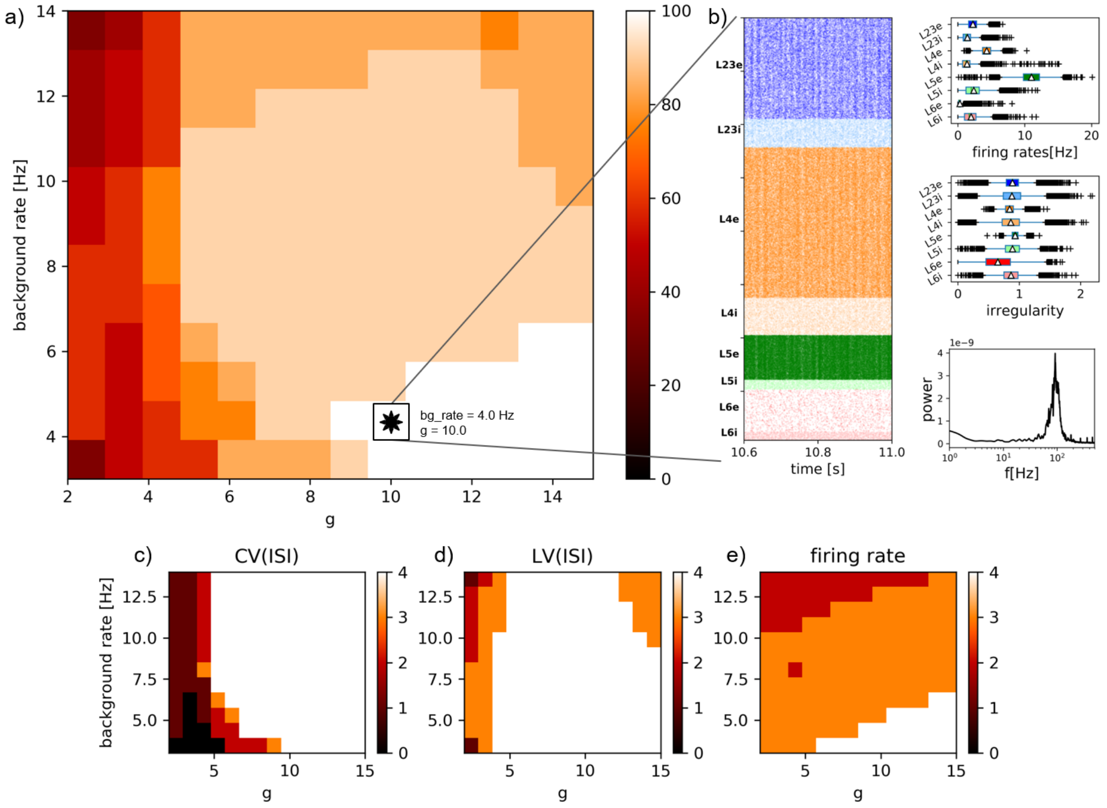

Figura 4.6: ***Dependence of network activity on the relative inhibitory synaptic strength*** g ***and the external Poisson background rate*** bg_{rate}. *The non-simulated areas were replaced by Poisson spike trains with the same firing rate. a) Colors represent the fraction out of the four populations of excitatory neurons (L2/3e, L4e, L5e and L6e) that have average coefficient of variation* $CV(ISI)$ *between 0.76 and 1.44, average local variation* $LV(ISI)$ *between 0.54 and 1.44 and average firing rate* $\nu \leq 12$ *spikes/second. b) Characterization of network activity for the set of parameters highlighted in a). The plots shown are the raster plot of spiking activity with dots indicating spike times; the boxplots of average firing rate per population; the boxplots of average irregularity per population; and the power spectrum calculated from average full network activity in time windows of 1 ms. The maps in c), d) and e) show the fraction out of the four excitatory populations that have, respectively, average* $CV(ISI)$*, average* $LV(ISI)$ *and average firing rate within the ranges given above.*

Figure 4.6a shows a color map where the color white represents the parameter configurations for which the four populations of excitatory neurons (L2/3e, L4e, L5e and L6e) have average values of $CV(ISI)$, $LV(ISI)$ and ν within experimental data ranges (Maksimov et al., 2018). The information contained in Figure 4.6a is a combination of maps in Figures 4.6c, 4.6d and 4.6e. These maps only show information extracted from excitatory populations (L2/3e, L4e, L5e and L6e) and the color indicates the fraction out of these four populations which have the corresponding average measure inside an experimentally determined range. These ranges were defined in (Maksimov et al., 2018) as $CV(ISI)$ between 0.76 and 1.44, $LV(ISI)$ between 0.54 and 1.44 and $\nu \leq 12$ spikes/second. Combining these three maps in one, it is possible to observe in Figure 4.6a the region of parameter space (in white) which displays characteristics in agreement with experiments.

From this region we extracted a point shown in Figure 4.6a with $g = 10.0$ and $bg_{rate} = 4.0$ Hz. The characteristics of the spontaneous activity of the corresponding network are shown in Figure 4.6b. One can see that the neurons spike at low frequency (below 10 Hz) and have irregularly around 1. However, one can also see stripes in the raster plot and a peak in the power spectrum. Since this network does not receive any external input, a more realistic situation would be with absence of a high frequency peak.

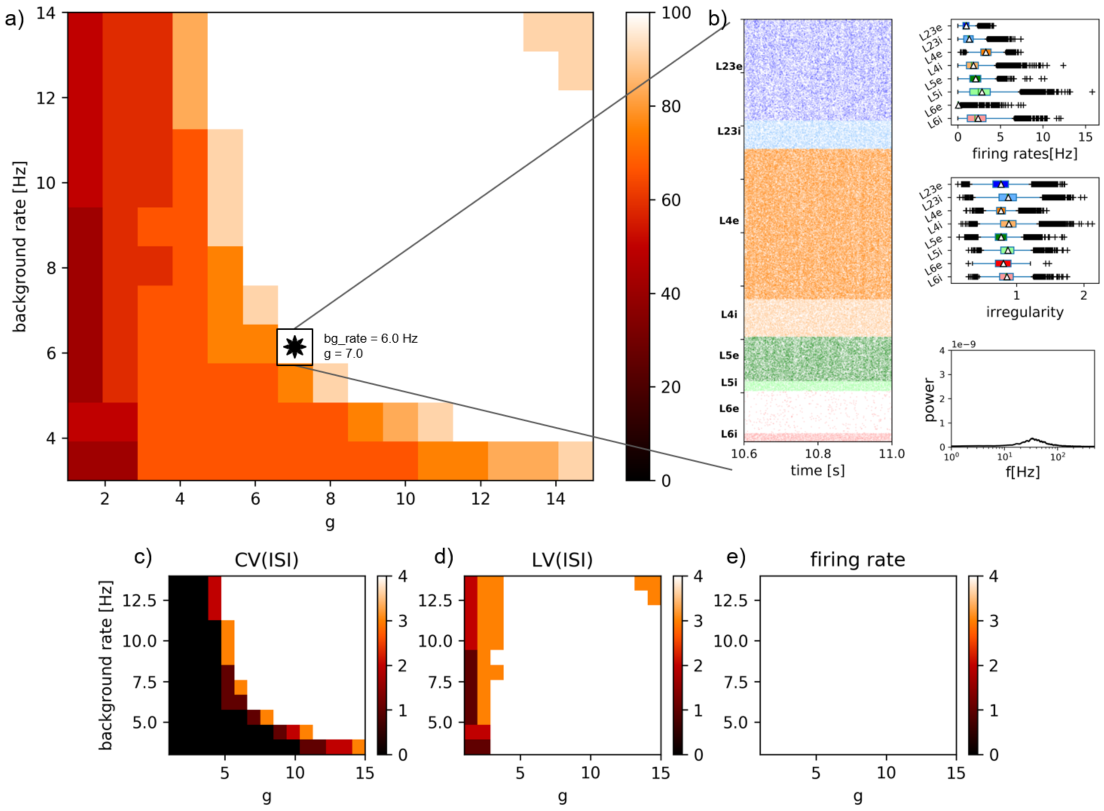

Figura 4.7: ***Dependence of network activity on the relative inhibitory synaptic strength*** g ***and the external Poisson background rate*** bg_{rate}. *The non-simulated areas were replaced by Poisson spike trains with specific firing rates related to the steady state activity of these areas. a) Colors represent the fraction out of the four populations of excitatory neurons (L2/3e, L4e, L5e and L6e) that have average coefficient of variation* $CV(ISI)$ *between 0.76 and 1.44, average local variation* $LV(ISI)$ *between 0.54 and 1.44 and average firing rate* $\nu \leq 12$ *spikes/second. b) Characterization of network activity for the set of parameters highlighted in a). The plots shown are the raster plot of spiking activity with dots indicating spike times; the boxplots of average firing rate per population; the boxplots of average irregularity per population; and the power spectrum calculated from average full network activity in time windows of 1 ms. The maps in c), d) and e) show the fraction out of the four excitatory populations that have, respectively, average* $CV(ISI)$, *average* $LV(ISI)$ *and average firing rate within the ranges given above.*

Lets consider now the case where the inputs representing corticocortical connections between different areas are represented by Poisson spike trains with specific firing rates extracted from a multi-area model (Schmidt et al., 2018b,a). Other inputs coming from areas non-simulated by the multi-area model were replaced by Poisson spike trains with same firing rate defined by bg_{rate}. Using this configuration it is possible to obtain a better result as can be seen in Figure 4.7. The region in parameter space which agrees with experimental data is bigger than in Figure 4.6. Moreover, in general, and as presented by the example chosen ($g = 7$ and $bg_{rate} = 6$ Hz), the network activity has lower population firing rates, shows less synchrony and displays a smaller peak in the power spectrum in comparison to the previous case.

The pair of parameters highlighted in the example in 4.7 ($g = 7$ and $bg_{rate} = 6$ Hz) was set as default for the following experiments.

4.6.3 Effect of spike frequency adaptation on cortical dynamics

The transition between the states of wakefulness and sleep of slow waves is related, among other factors, to changes in the levels of the neurotransmitter acetylcholine (ACh) (Steriade et al., 1993; Baghdoyan and Lydic, 1999). At the neuronal level, ACh regulates the excitability of neurons and can reduce their spike frequency adaptation (SFA) (Aiken et al., 1995; Tsuno et al., 2013). In addition, in the neocortex, neurons with cholinergic receptors are distributed with high density throughout all layers (Eckenstein et al., 1988; Henny and Jones, 2008; Kalmbach et al., 2012), and may have different effects depending on the type of cell and the layer in question (Radnikow and Feldmeyer, 2018).

One of the variables in the AdEx model described in Equations 4.3 and 4.4 which can control the SFA is the variable b. Thus, one phenomenological way of mimicking the ACh level is by changing b of the excitatory neurons. The default value of b used in all simulations, except when mentioned, is presented in Table 5.1. Figure 4.8 shows the membrane potential in time of excitatory RS neurons when the variable b is defined as a)5, b)20, c)40 and d)100 pA, respectively. The increase of b increases the SFA, which in its turn represents the decrease of ACh.

To assess the network dynamics for different values of parameter b, we fixed $g = 7.0$ and $bg_{rate} = 6.0$ Hz and run the simulations varying the b value of the RS neurons.

Experimental data on cortical activity show that increases in ACh levels also induce the appearance of oscillations in the gamma range for the primary visual

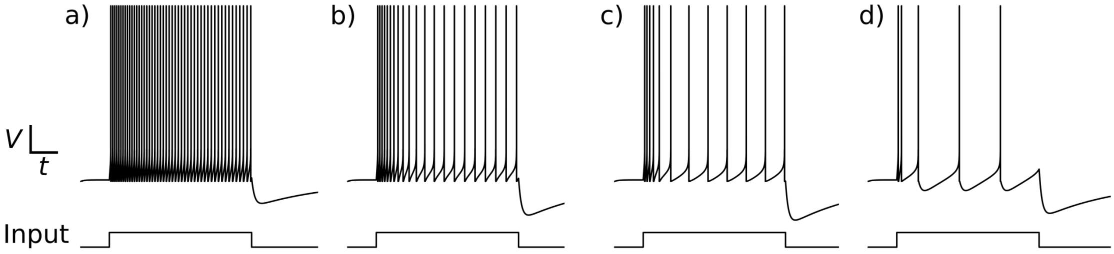

Figura 4.8: ***Spike frequency adaptation on excitatory neurons***. *Membrane potential response of V1 excitatory neurons when stimulated by a depolarizing square current input under four different levels of spike frequency adaptation (which is controlled in AdEx model by variable b): a) $b = 5$ pA, b) $b = 20$ pA, c) $b = 40$ pA and d) $b = 100$ pA.*

cortex (Rodriguez et al., 2004) and PFC (Howe et al., 2017). This same effect can be seen in the results of Figure 4.9, where lower values of b (low SFA) indicate an increase in ACh levels.

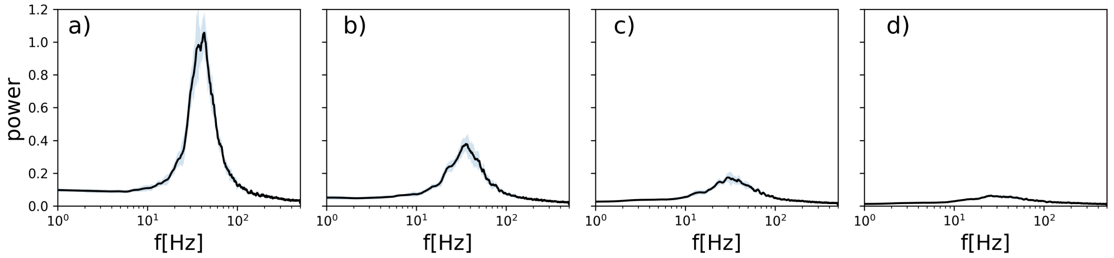

Figura 4.9: ***V1 network activity power spectra under different spike frequency adaptation levels***. *Power spectra estimated from the network spiking activity of four different levels of spike frequency adaptation when setting the b parameter of the AdEx model used for the excitatory neurons as a) 5 pA, b) 20 pA, c) 40 pA and d) 100 pA. In gray is presented the standard deviation through ten simulation.*

For V1 microcircuit the variation of SFA was not enough to generate slow waves but was able to reduce the rapid oscillation when reducing the ACh (increasing the AdEx parameter b of RS neurons).

Furthermore, to explore the SFA effect in the network, it was also checked its effect for different combinations of parameters g and bg_{rate} as presented in Figure 4.7. The results are presented in Figures 4.10 and 4.11.

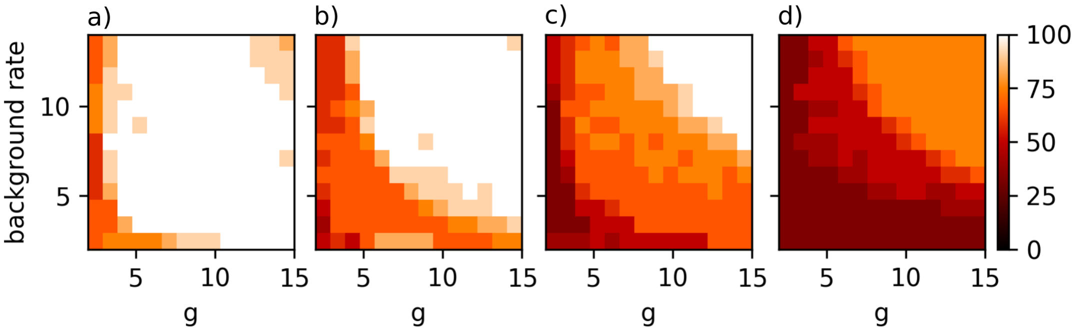

Figura 4.10: ***Parameter scan under different spike frequency adaptation levels***. *Dependence of network activity on the relative inhibitory synaptic strength* g *and the external Poisson background rate* bg_{rate} *under four different spike frequency adaptation levels of excitatory neurons when setting the* b *parameter of the AdEx model as a) 5 pA, b) 20 pA, c) 40 pA and d) 100 pA. The colors in the maps represent the fraction out of the four populations of excitatory neurons (L2/3e, L4e, L5e and L6e) that have average coefficient of variation* $CV(ISI)$ *between 0.76 and 1.44, average local variation* $LV(ISI)$ *between 0.54 and 1.44 and average firing rate* $\nu \leq 12$ *spikes/second.*

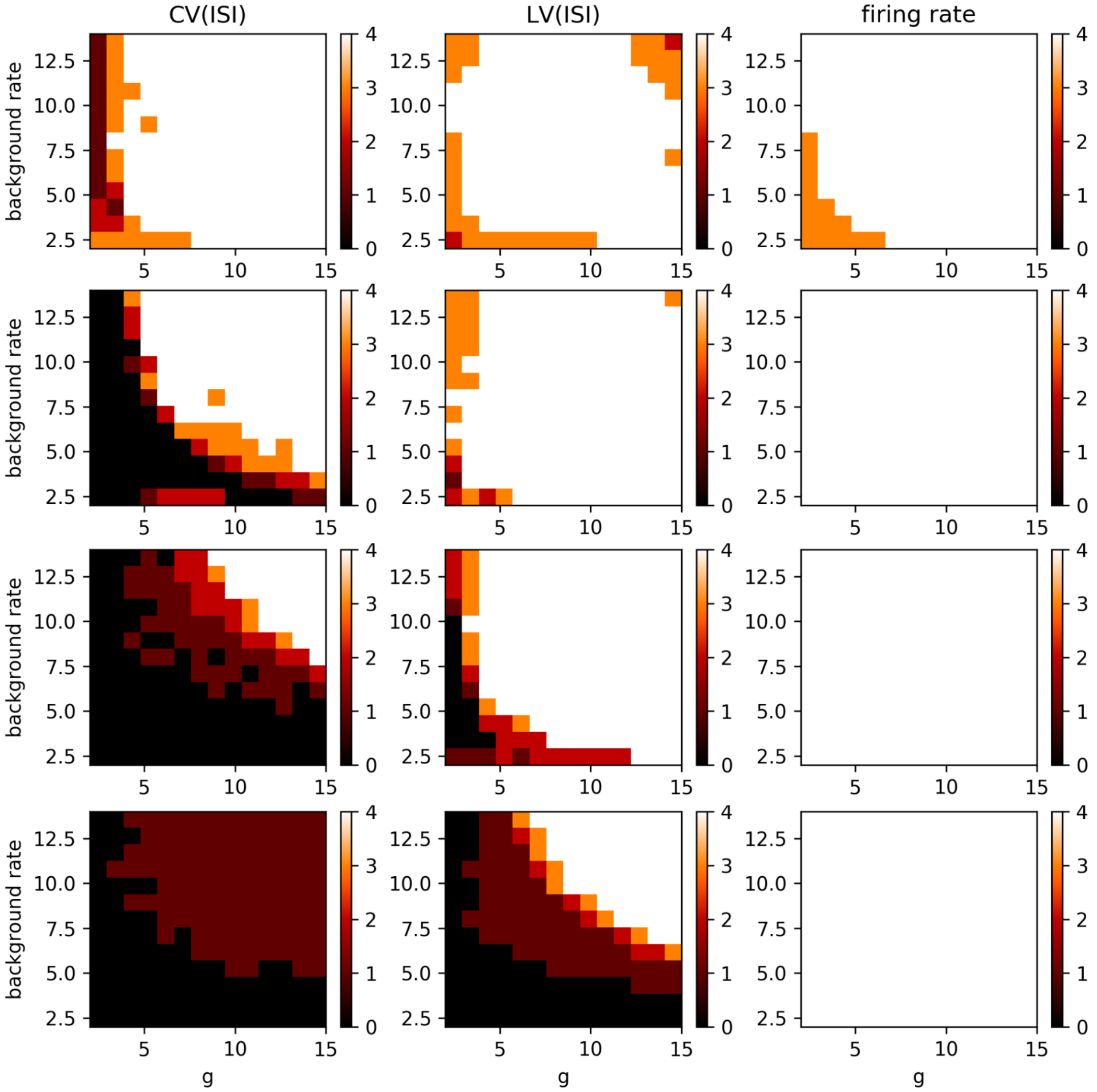

Figura 4.11: ***Network regularity and firing rate under different spike frequency adaptation levels***. *Dependence of network activity on the relative inhibitory synaptic strength g and the external Poisson background rate* bg_{rate} *under four different spike frequency adaptation levels of excitatory neurons when setting the b parameter of the AdEx model as 5 pA (first row), 20 pA (second row), 40 pA (third row) and 100 pA (fourth row). The colors in the maps represent the number among the four populations of excitatory neurons (L2/3e, L4e, L5e and L6e) that have average coefficient of variation* $CV(ISI)$ *between 0.76 and 1.44 in the first column, average local variation* $LV(ISI)$ *between 0.54 and 1.44 in the second column and average firing rate* $\nu \leq 12$ *spikes/second in the third column.*

Although the fast oscillations are reduced as exemplified in Figure 4.9, the region of parameters displayed by the white color in Figure 4.10 presenting a healthy spontaneous activity is reduced by increasing the SFA on the excitatory neurons. To differentiate what measure leads the network to a “non-healthy” activity, we plotted the Figure 4.11 which shows that the increase of SFA increases mainly the neuronal spiking regularity, represented by the CV when it is close to zero.

4.6.4 Thalamocortical spontaneous activity

The spontaneous activity when connecting the V1 microcircuit to the LGN network is presented in Figures 4.12 and 4.13. For this example, we set the $d_{thc} = d_{cth} = 40.0$ ms (Equation 4.5) and ran ten simulations for a time duration of 11.0 s. When comparing Figures 4.12 a), b), c) and d) with Figure 4.7 b) it is possible to observe the emergence in the thalamocortical network of oscillatory behavior through the stripes in the raster plot and the peaks at the power spectrum. Nevertheless, the firing rate was kept the same and a disturbance occurred in the irregularity measure but still keeping it close to $CV = 1$.

Besides the thalamic neuronal intrinsic characteristics included in the model, the network parameters were set to keep a low activity in the LGN with firing rates similar to the ones observed in the cortical network, as can be seen in Figure 4.13 b). Figure 4.13 a) shows a sparse network activity and Figures 4.13 c) and d) show the their power spectra. There are slow and fast oscillations, but we focused on how these oscillatory behavior reflected in the V1 activity. The next chapter explores these features in more detail.

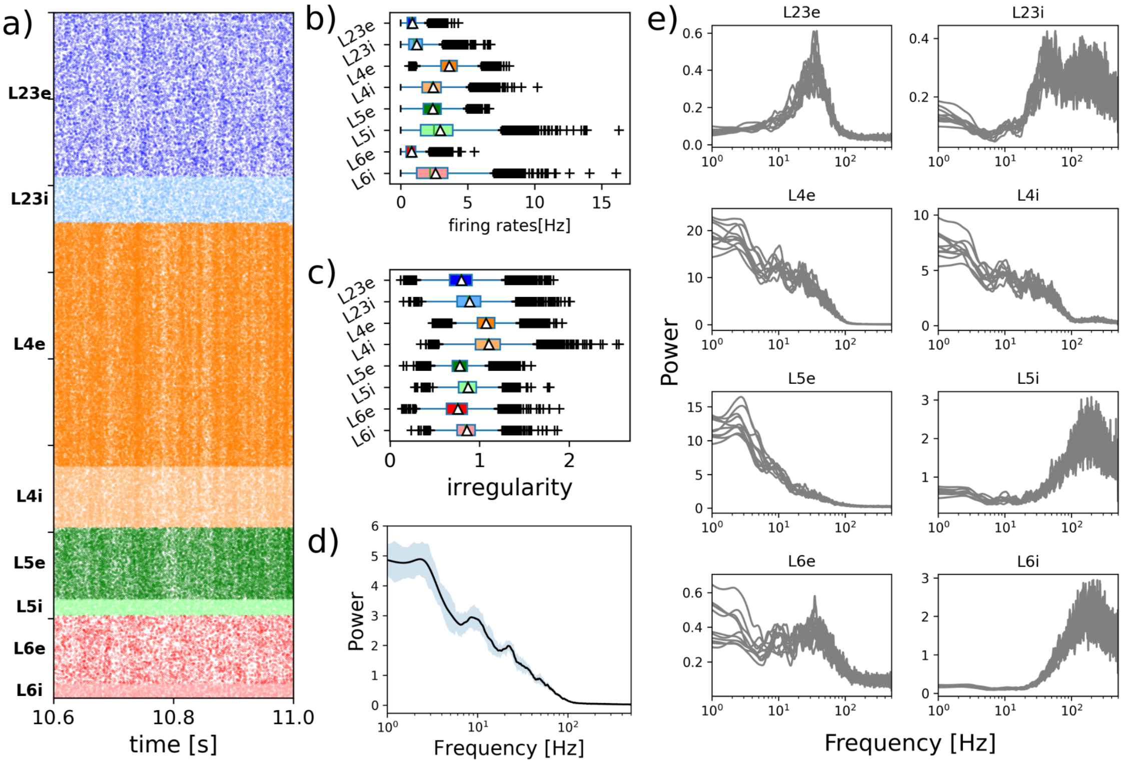

Figura 4.12: ***V1 microcircuit activity when connected to the LGN.*** *The plots shown are the a) raster plot showing the spiking activity of the full cortical network (all 197.932 neurons) with dots indicating spike times where each population indicated on the y-axis is represented by a different color; b) the boxplots of average firing rate per population; c) the boxplots of average irregularity per population; d) and the power spectrum calculated from average full network activity in time windows of 1 ms. Additionally, in e) the power spectrum estimated by each population's activity is given.*

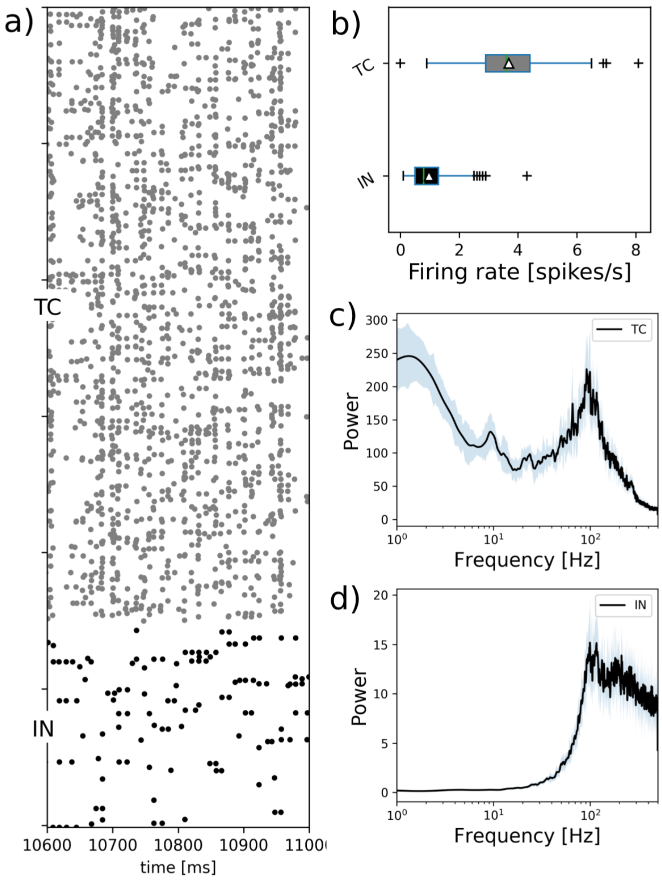

Figura 4.13: ***LGN activity from the thalamocortical circuit****. The plots shown are a) the raster plot of spiking activity with dots indicating spike times; b) the boxplots of average firing rate per population; c) and d) their power spectra calculated from average LGN excitatory (TC cells) and inhibitory (IN cells) activity in time windows of 1 ms, respectively.*

Chapter 5

Visual alpha generators in a spiking thalamocortical microcircuit model

This chapter explores different hypothetical mechanisms of alpha generation in a thalamocortical model of spiking neurons and shed light on the conditions under which this oscillation may emerge.

More specifically, two hypothesis involving the primary visual cortex (V1) and the lateral geniculate nucleus (LGN) were studied:

- Hypothesis 1 (L5 IB neurons): Alpha oscillations can be generated by the presence of intrinsically bursting (IB) neurons in cortical layer five (L5). These neurons can rhythmically oscillate around 10 Hz and L5 is the only layer which can display alpha oscillations when isolated from the other layers (Silva et al., 1991);

- Hypothesis 2 (thalamocortical loop delay): The alpha oscillations can be generated by a thalamocortical loop delay around 100 ms (Roberts and Robinson, 2008).

5.1 Simulation protocols

5.1.1 Generation of alpha rhythm with L5 excitatory Intrinsic Bursting neurons

The AdEx parameters for IB neurons presented in Table 5.1 were chosen based on the spiking behaviour cited in (Silva et al., 1991). Two main features were qualitatively kept: the bursting behaviour when stimulated by constant current (Figure 5.1a) and spontaneous bursts triggered by a current pulse (Figure 5.1d).

	C_m[pF]	g_L[nS]	E_L[mV]	Δ_T[mV]	V_{th}[mV]	τ_{ref}[ms]	τ_w[ms]	V_r[mV]	a[nS]	b[pA]
IB	200.0	3.0	-58.0	2.5	-58.0	2.0	40.0	-50.0	20.0	100.0

Tabela 5.1: *Parameters used in AdEx neuron model for cortical IB neurons. The IB parameters were adjusted to behave similarly to experimental data presented in (Silva et al., 1991).*

To achieve this neuronal dynamics we analysed the phase space of the AdEx model (example in Figure 5.1c, which corresponds to spikes shown in 5.1d) and searched a set of parameters capable of reproducing these two behaviours.

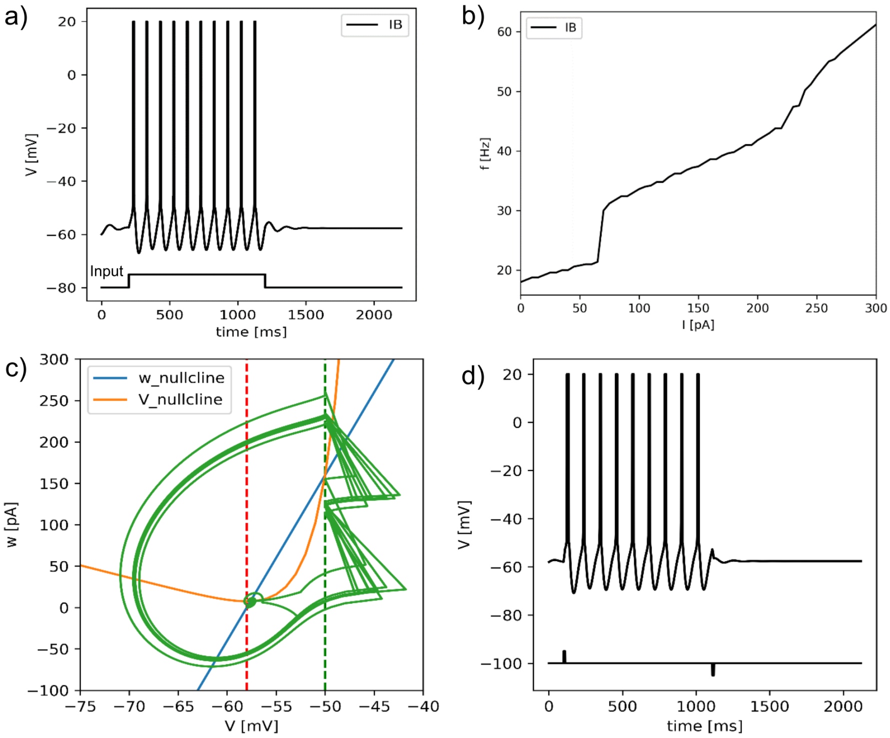

Figura 5.1: ***IB neuron dynamics simulated by AdEx model.*** *a) Membrane voltage response in time for IB neuron when stimulated by a square pulse. b) The curve of firing rate versus current amplitude. c) Phase space of the AdEx model where the blue line is the nullcline of w and orange the nullcline of V. In green is the trajectory of the system in the phase plane $w - V$ corresponding to the simulation shown in d).*

With the AdEx parameters set, the former hypothesis mentioned was tested in the V1 microcircuit. This hypothesis consists in the generation of alpha rhythm due to the intrinsic properties of cortical L5 intrinsic bursting (IB) neurons. For this purpose, first we varied the percentage of IB neurons replacing excitatory neurons from L5e (from 10% to 60%). The range reported experimentally of the proportion of IB neurons at L5e is around 50% (Silva et al., 1991).

Before analyzing the influence of IB neurons on the V1 microcircuit, the activity of the isolated L5 with and without adding IB neurons in the network was analyzed. Subsequently, the same comparison was done for the full cortical network.

5.1.2 Relation between thalamocortical loop delay and generation of alpha oscillation

Here the influence of the corticothalamic transmission delay in the generation of alpha rhythm in the thalamocortical network model described in Section 2.3 was analyzed. For this study, the thalamocortical and the corticothalamic transmission delay were varied following ranges found in the literature for human data and related with hypothesis 2 (around 100 ms) (Robinson et al., 2001a; van Albada et al., 2010; Yamaguchi et al., 2018).

Another mechanism analyzed in this context was the synaptic strength ratio between thalamocortical connections onto excitatory and inhibitory L4 cortical neurons.

The protocol described in this section was repeated including the IB neurons in cortical L5 aiming to explore the interplay between these two possible mechanisms of alpha generation.

5.2 Measures and analysis

In addition to the measures described in 4.5, here we describe the Pairwise and Conditional Granger Causality measures used to identify spectral influences at the alpha range among different neuronal populations.

5.2.1 Pairwise Granger Causality in the frequency domain

These next sections about Granger Causality are adaptations of the educational article published by me and colleagues (Lima et al., 2020) entitled “Granger causality in the frequency domain: derivation and applications".

To delineate the patterns of interaction among different alpha current generators the Granger Causality (GC) in the frequency domain was measured. The general idea of GC can be understood if we consider two simultaneously measured time series $X_1(t)$ and $X_2(t)$, in this context the variable $X_1(t)$ can be called causal to $X_2(t)$ if information in the past of $X_1(t)$ helps to predict $X_2(t)$ (Granger, 1969; Seth, 2007).

The GC in the frequency domain was estimated using the method described in Dhamala et al. (2008). In this method the GC is estimated through the non-parametric decomposition of a spectral matrix containing the power spectrum of each signal and the cross power spectrum between them.

The key advantage of utilizing the non-parametric technique instead of parametric ones to calculate GC is that it eliminates the need to determine the model order for the autoregressive model. The right model order can be difficult to determine because it varies based on the subject, experimental task, data quality and complexity, and model estimating approach used (Kamiński and Liang, 2005; Barnett and Seth, 2011).

As described in the last section, we can estimate the power spectrum with good balance between frequency resolution and variance with the multitaper method. Let us denote the power spectrum of $X_1(t)$ and $X_2(t)$ as $S_{11}(f)$ and $S_{22}(f)$ respectively. Then, the cross spectra will be called $S_{12}(f)$ and $S_{21}(f)$. So, the spectral matrix is:

$$S(f) = \begin{bmatrix} S_{11}(f) & S_{12}(f) \\ S_{21}(f) & S_{22}(f) \end{bmatrix}. \tag{5.1}$$

Using Wilson’s algorithm (Wilson, 1972, 1978) is possible to decompose equation 5.1 in:

$$S(f) = H(f)\Sigma(f)H^{\dagger}(f) \tag{5.2}$$

where $H(f)$ is called the transfer matrix and † denotes the transpose conjugate of the matrix $S(f)$.

From $H(f)$ and $\Sigma(f)$ it is possible to calculate the GC from signal 1 to 2 ($I_{1\to2}$) and 2 to 1 ($I_{1\to2}$) with the following equations (Geweke, 1982; Ding et al., 2006; Dhamala et al., 2008).

$$I_{1\to2}(f) = \ln\left(\frac{S_{22}(f)}{S_{22}(f) - (\Sigma_{11} - \frac{\Sigma_{21}^2}{\Sigma_{22}})|H_{21}(f)|^2}\right) \tag{5.3}$$

and

$$I_{2\to1}(f) = \ln\left(\frac{S_{11}(f)}{S_{11}(f) - (\Sigma_{22} - \frac{\Sigma_{12}^2}{\Sigma_{11}})|H_{12}(f)|^2}\right) \tag{5.4}$$

The algorithm and codes used to measure the GC defined above were described in Lima et al. (2020) and the code is available at `https://github.com/ViniciusLima94/pyGC.git`.

5.2.2 Conditional Granger Causality in the frequency domain

The concepts developed so far may be applied to a case with m variables. In this case, in order to try and infer the directionality[1] of the interaction between two signals, in a system with m signals, we may use the so-called conditional Granger causality (cGC) (Geweke, 1984; Chen et al., 2006; Ding et al., 2006; Malekpour and Sethares, 2015). The idea is to infer the GC between signals i and j given the knowledge of all the other $m-2$ signals of the system. This is done by comparing the variances obtained considering only i and j to the variances obtained considering all the other signals in the system.

---

[1] Whether i Granger-causes j or *vice-versa*.

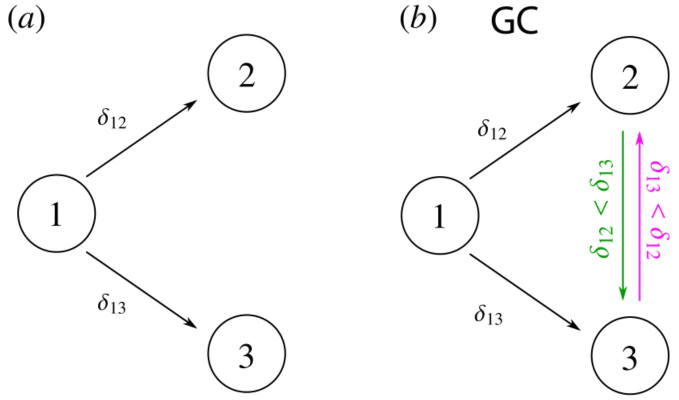

Figura 5.2: ***A system that pairwise GC fails to describe. a.*** *Node 1 ($X_1(t)$) sends input to node 2 ($X_2(t)$) with delay δ_{12} and to node 3 ($X_3(t)$) with delay δ_{13}.* ***b.*** *A simple GC calculation wrongly infer a link from $X_2(t)$ to $X_3(t)$ if $\delta_{12} < \delta_{13}$, or from $X_3(t)$ to $X_2(t)$ if $\delta_{13} < \delta_{12}$. These links are not physically present in the system and appear only due to the cross-correlation between $X_2(t)$ and $X_3(t)$ caused by the common input $X_1(t)$.*

But one may ask: "isn't it simpler to just calculate the standard GC between every pair of signals in the system, always reducing the problem to a two-variable case?" To answer that question, consider the case depicted in Figure 5.2a: node 1 ($X_1(t)$) sends input to node 2 ($X_2(t)$) with a delay δ_{12} and sends input to node 3 ($X_3(t)$) with a delay δ_{13}. Measuring the pairwise GC between $X_2(t)$ and $X_3(t)$ suggests the existence of a coupling between them even if it does not physically exist (as in Figure 5.2b). This occurs because signals $X_2(t)$ and $X_3(t)$ are correlated due to their common input from $X_1(t)$, and the simple pairwise GC between $X_2(t)$ and $X_3(t)$ fails to represent the correct relationship between the three nodes of Figure 5.2a. The cGC solves this issue by considering the contribution of a third signal ($X_1(t)$ on this example) onto the analyzed pair ($X_2(t)$ and $X_3(t)$), as described below.

The following equation describe the system presented in Figure 5.2:

$$\begin{pmatrix} X_1(\omega) \\ X_2(\omega) \\ X_3(\omega) \end{pmatrix} = \begin{pmatrix} H_{11}(\omega) & H_{12}(\omega) & H_{13}(\omega) \\ H_{21}(\omega) & H_{22}(\omega) & H_{23}(\omega) \\ H_{31}(\omega) & H_{32}(\omega) & H_{33}(\omega) \end{pmatrix} \begin{pmatrix} \epsilon_1^*(\omega) \\ \epsilon_2^*(\omega) \\ \epsilon_3^*(\omega) \end{pmatrix}, \tag{5.5}$$

where $X_3(t)$ has the noise term $\epsilon_3(t)$ with variance Σ_{33}. The corresponding spectral matrix $\boldsymbol{S}(\omega)$ is

$$\boldsymbol{S}(\omega) = \begin{bmatrix} S_{11}(\omega) & S_{12}(\omega) & S_{13}(\omega) \\ S_{21}(\omega) & S_{22}(\omega) & S_{23}(\omega) \\ S_{31}(\omega) & S_{32}(\omega) & S_{33}(\omega) \end{bmatrix}, \tag{5.6}$$

and the noise covariance matrix is

$$\boldsymbol{\Sigma} = \begin{bmatrix} \Sigma_{11} & \Sigma_{12} & \Sigma_{13} \\ \Sigma_{21} & \Sigma_{22} & \Sigma_{23} \\ \Sigma_{31} & \Sigma_{32} & \Sigma_{33} \end{bmatrix}. \tag{5.7}$$

We want to calculate the cGC from $X_2(t)$ to $X_3(t)$ given $X_1(t)$, *i.e.* $F_{2\to 3|1}$ in the time domain and $I_{2\to 3|1}(\omega)$ in the frequency domain. The first step is to build a partial system from equation (5.5) ignoring the coefficients related to the probe signal $X_2(t)$, resulting in the partial spectral matrix $\boldsymbol{S}^p(\omega)$:

$$\boldsymbol{S}^p(\omega) = \begin{bmatrix} S_{11}(\omega) & S_{13}(\omega) \\ S_{31}(\omega) & S_{33}(\omega) \end{bmatrix}. \tag{5.8}$$

From this partial system, we can calculate $\boldsymbol{S}^p(\omega)$ and $\boldsymbol{S}(\omega)$ using the nonparametric methods already discussed above. Suppose that for $\boldsymbol{S}(\omega)$, we obtain the transfer matrix $\boldsymbol{H}(\omega)$ and the covariance matrix $\boldsymbol{\Sigma}$ (equation (5.7)), whereas for $\boldsymbol{S}^p(\omega)$ we obtain the transfer matrix $\boldsymbol{G}(\omega)$ and the covariance matrix $\boldsymbol{\rho}$:

$$\boldsymbol{\rho} = \begin{bmatrix} \rho_{11} & \rho_{13} \\ \rho_{31} & \rho_{33} \end{bmatrix}. \tag{5.9}$$

The matrices $\boldsymbol{H}(\omega)$ and $\boldsymbol{\Sigma}$ are 3×3. The matrices $\boldsymbol{G}(\omega)$ and $\boldsymbol{\rho}$ are always one dimension less than the original ones, because they are built from the leftover rows and columns of the original system without the coefficients of the probe signal.

In the time domain, $F_{2\to 3|1}$ is defined as

$$F_{2\to 3|1} = \log\left(\frac{\rho_{33}}{\Sigma_{33}}\right), \tag{5.10}$$

or, in general,

$$F_{i\to j|k} = \log\left(\frac{\rho_{jj}}{\Sigma_{jj}}\right), \tag{5.11}$$

which is used to calculate the cGC from i to j given k, in time domain. Note that if the link between i and j is totally mediated by k, $\rho_{jj} = \Sigma_{jj}$, yielding $F_{i\to j|k} = 0$. However, the standard GC between i and j would result in a link between these variables. For our example in Figure 5.2, we obtain $F_{2\to 3|1} \gtrsim 0$, meaning that the influence of $X_2(t)$ to $X_3(t)$ is conditioned on signal $X_1(t)$, and hence is almost null.

In the frequency domain, we first must define the transfer matrix $\boldsymbol{Q}(\omega) = \boldsymbol{G}(\omega)^{-1}\boldsymbol{H}(\omega)$. However, the dimensions of matrix $\boldsymbol{G}(\omega)$ do not match the dimensions of matrix $\boldsymbol{H}(\omega)$. To fix that, we add rows and columns from an identity matrix to the rows and columns that were removed from the total system in equation (5.5) when we built the partial system (*i.e.* we add the identity rows and columns to the rows and columns corresponding to signal $X_2(t)$ that was removed for generating $\boldsymbol{S}^p(\omega)$), such that:

$$\mathbf{G}(\omega) = \begin{bmatrix} G_{11}(\omega) & G_{13}(\omega) \\ G_{31}(\omega) & G_{33}(\omega) \end{bmatrix} \Rightarrow \begin{bmatrix} G_{11}(\omega) & 0 & G_{13}(\omega) \\ 0 & 1 & 0 \\ G_{31}(\omega) & 0 & G_{33}(\omega) \end{bmatrix}. \tag{5.12}$$

We can now safely calculate $\boldsymbol{Q}(\omega) = \boldsymbol{G}(\omega)^{-1}\boldsymbol{H}(\omega)$, from where we obtain $I_{2\to 3|1}(\omega)$:

$$I_{2\to 3|1}(\omega) = \log\left(\frac{\rho_{11}}{|Q_{11}(\omega)\Sigma_{11}Q^{\dagger}_{11}(\omega)|}\right), \tag{5.13}$$

or, in general,

$$I_{i\to j|k}(\omega) = \log\left(\frac{\rho_{jj}}{|Q_{jj}(\omega)\Sigma_{jj}Q^{\dagger}_{jj}(\omega)|}\right). \tag{5.14}$$

It is important to note that the cGC connectivity not always reflects the underlying physical (or structural) connectivity between elements (Seth, 2007). Real-world applications, such as inferring neuronal connectivity from brain signals, result in a cGC matrix that is very noisy due to multiple incoming signals and multiple delays. Thus, cGC is most generally referred to as giving “functional” connectivity, instead of structural connectivity.

5.3 Results

Our approach to study the alpha generation hypotheses was a step-like process which initially considered each area (V1 and LGN) separately and characterized its spontaneous activity. Then we analyzed each hypothesis separately (L5 IB neurons and thalamocortical loop delay) and, finally, we put everything together.

5.3.1 Generation of alpha rhythm with L5 excitatory Intrinsic Bursting neurons

To evaluate the first hypothesis (layer 5 intrinsically bursting (IB) neurons) in the V1 microcircuit, we replaced 50% of excitatory RS neurons in L5 by IB neurons. Initially, we analysed the influence of IB neurons in the isolated L5. Comparing Figures 5.3a and 5.3b it is possible to observe the generation of alpha activity by looking the emergence of a big peak in the alpha range.

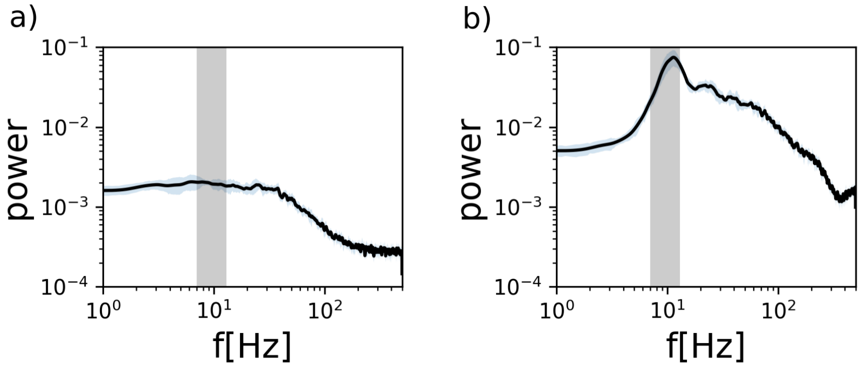

Figura 5.3: ***Power spectra of the excitatory spiking activity for the isolated L5***. *Left: default case is represented by the L5 with all excitatory neurons spiking as RS. Right: 50% of RS neurons were replaced by IB neurons. In both cases the inhibitory populations remains the same.*

Since it was shown that IB neurons can generated alpha in isolated L5, the next step is connect the full V1 microcircuit to study how it spreads through the network.

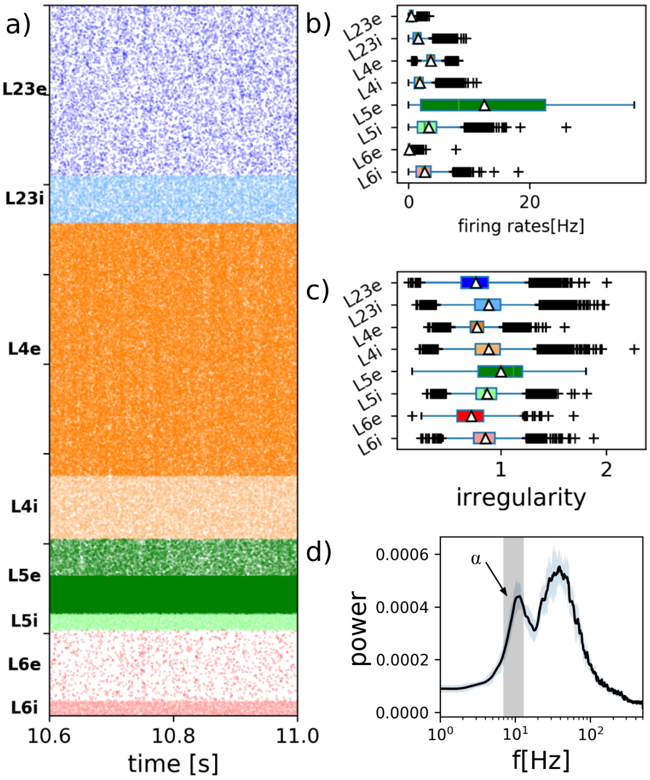

Figura 5.4: ***Activity of the V1 microcircuit when 50% of L5 excitatory neurons were replaced by IB neurons.*** *a) Raster plot with dots indicating spike times for each neuron represented in rows. Darker colors refer to excitatory neurons and lighter to inhibitory ones. From top to bottom it is shown in sequence layers L2/3 to L6. The IB neurons in L5 are represented in dark green and are possible to be differentiated from RS neurons by the higher firing rate. b) Boxplot of the average firing rate per population. c) Boxplot of the average $CV(ISI)$ per population. d) Power spectrum calculated from the averaged full network activity in time windows of 1 ms.*

In the raster plot in Figure 5.4a and firing rate boxplots in Figure 5.4b it is possible to see an increase in the activity of L5 excitatory neurons, which is caused by the IB neurons as expected. Moreover, the average CV of L5e in Figure 5.4c increased as a consequence of the bursts induced by IB cells. Notably, the power spectrum now shows a prominent and clearly identifiable peak in the alpha band (Figure 5.4d).

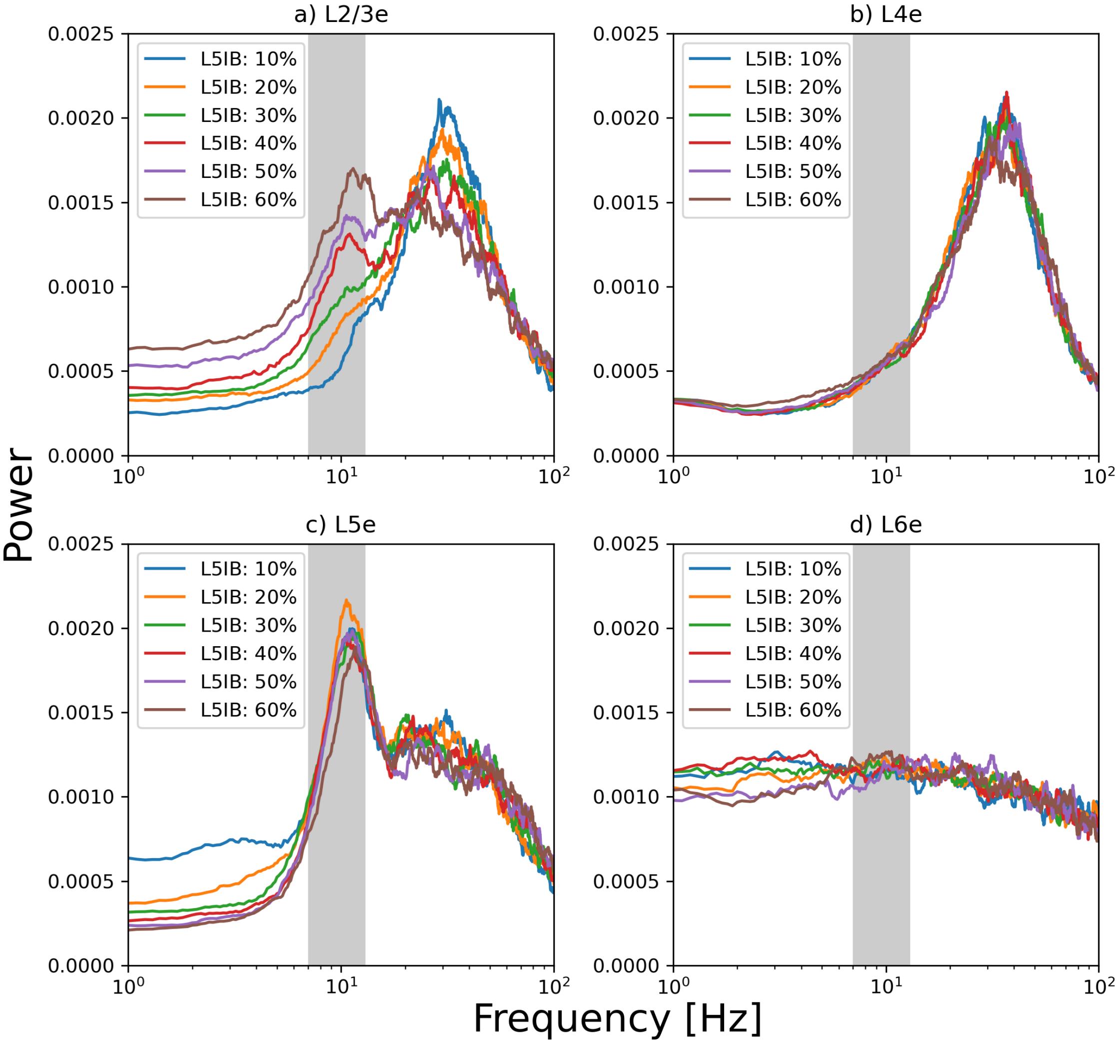

Figura 5.5: *Population activity power spectra under different percentages of L5 IB neurons*. *The power spectra were estimated from excitatory spiking activity by layer for different proportions of IB neurons at L5 (10 to 60% of the total L5 excitatory neurons). The shadowed area represents the alpha range.*

To systematically explore the effect of introducing L5 IB neurons in the network we varied the proportion between IB and RS neurons. Figure 5.5 shows the power spectrum estimated from the excitatory activity by each layer when varying the ratio between RS and IB neurons at L5. It is possible to observe the emergence of alpha oscillations at L5 even with only 10% of RS replaced by the IB neurons. Additionally, when increasing the percentage of IB at L5 an alpha peak appear at L2/3, becoming more apparent above the ratio of 40%.

Although 5.5 shows the emergence of an alpha peak in networks activity, it does not discriminate how this oscillation spreads through the other layers. To analyze that, we kept the proportion of 50% of IB neurons in L5e and we calculated the Granger causality (GC) in the frequency domain as described in Sections 5.2.1 and 5.2.2.

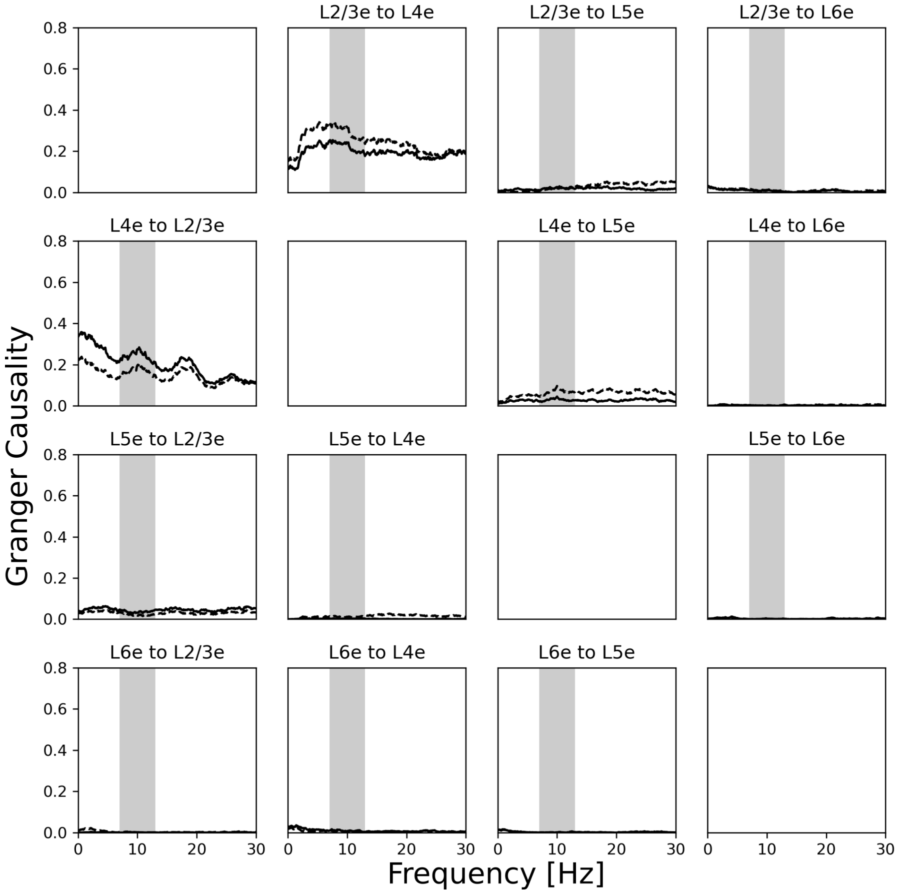

Figura 5.6: ***Granger causality analysis of V1 microcircuit.*** *Granger causality (y-axis) in the frequency domain (x-axis) for the default V1 cortical network. Pairwise GC are represented with dashed lines and cGC with solid lines.*

The GC estimated for the default network, V1 microcircuit without IB neurons, is presented in Figure 5.6 where each graph is related to a pair of excitatory populations. As expected, since the power spectrum in Figure 4.7 does not show prominent oscillations, the GC did not display a clear peak for any population pair. The only suggestive indication of causality of one layer in another was between L2/3e and L4e, but still, there is no well-defined peak.

This situation changes when including IB neurons on L5. Figure 5.7 shows the GC when alpha is generated by IB cells.

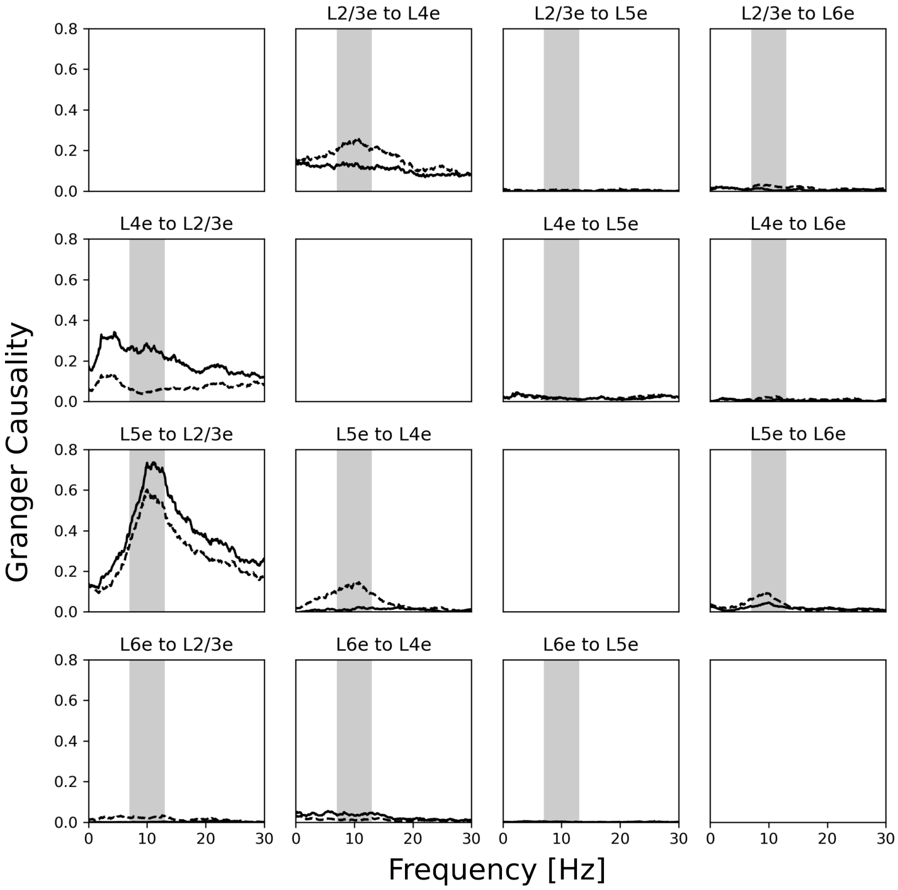

Figura 5.7: ***Granger causality analysis of V1 microcircuit with L5 IB neurons***. *Granger causality (y-axis) in the frequency domain (x-axis) for the default V1 cortical network with the replacement of 50% of layer 5 excitatory cells by IB neurons. Pairwise G-causalities are represented with dashed lines and conditional G-causalities with solid lines.*

It is possible to observe in 5.7 that there is GC (dashed lines) between L5 and all other layers, with the strongest effect being from L5e to L2/3e followed by L5e to L4e and then L5e to L6e. Interestingly, the other pronounced GC peak was from L2/3e to L4e, which matches with some references that suggest layers 2 and 5 as the locations of primary local pacemaking generators of alpha (Bastos et al., 2014; van Kerkoerle et al., 2014). Another relevant consideration is about the Conditional GC (solid lines), looking through it the only strong peak that remains is the one from L5e to L2/3e, which means that this is the only path where the oscillation is directed influencing one layer to another.

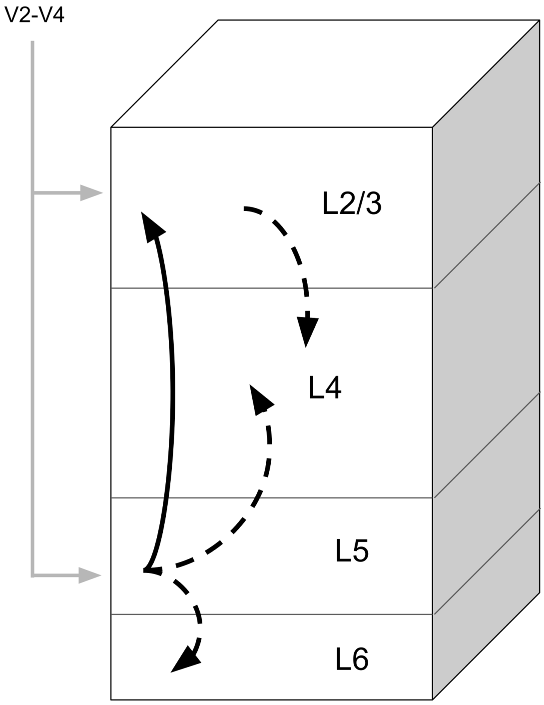

Figura 5.8: ***Schematic draw of the GC analysis of V1 network with L5 IB neurons included***. *Scheme representing the direction of the propagation of alpha rhythm through the cortical layers based on the GC measures. Pairwise GC are represented with dashed arrows while cGC with solid lines. The V2 and V4 inputs (in gray) are merely representative. These inputs show the main pathways coming from cortico-cortical connections into V1 which could be considered as possible alpha generators in experimental data.*

Figure 5.8 summarizes the alpha rhythm propagation direction estimated by the GC measure. We show here that L5 IB neurons is enough to generate alpha oscillations in a V1 microcircuit and although L2/3 does not have a specific alpha generator in there, the oscillatory activity transmitted from L5 to L2/3 may explain experimental findings only by the network dynamics and not necessarily by having a pacemaker in L2.

5.3.2 Relation between thalamocortical loop delay and generation of alpha oscillation

The second hypothesis was tested in a recurrent thalamocortical network with the thalamic network representing LGN connected to V1. The LGN model consists in a network of AdEx neurons divided in 902 excitatory thalamocortical cells (TC) and 301 inhibitory interneurons (IN).

The power spectra estimated from the full network spiking activity when varying the combination of the thalamocortical delay (d_{thc}) and the corticothalamic delay (d_{cth}) are shown in Figure 5.9. These corticothalamic delays were tested to better comprise different intervals suggested in literature (Robinson et al., 2001a; van Albada et al., 2010; Yamaguchi et al., 2018).

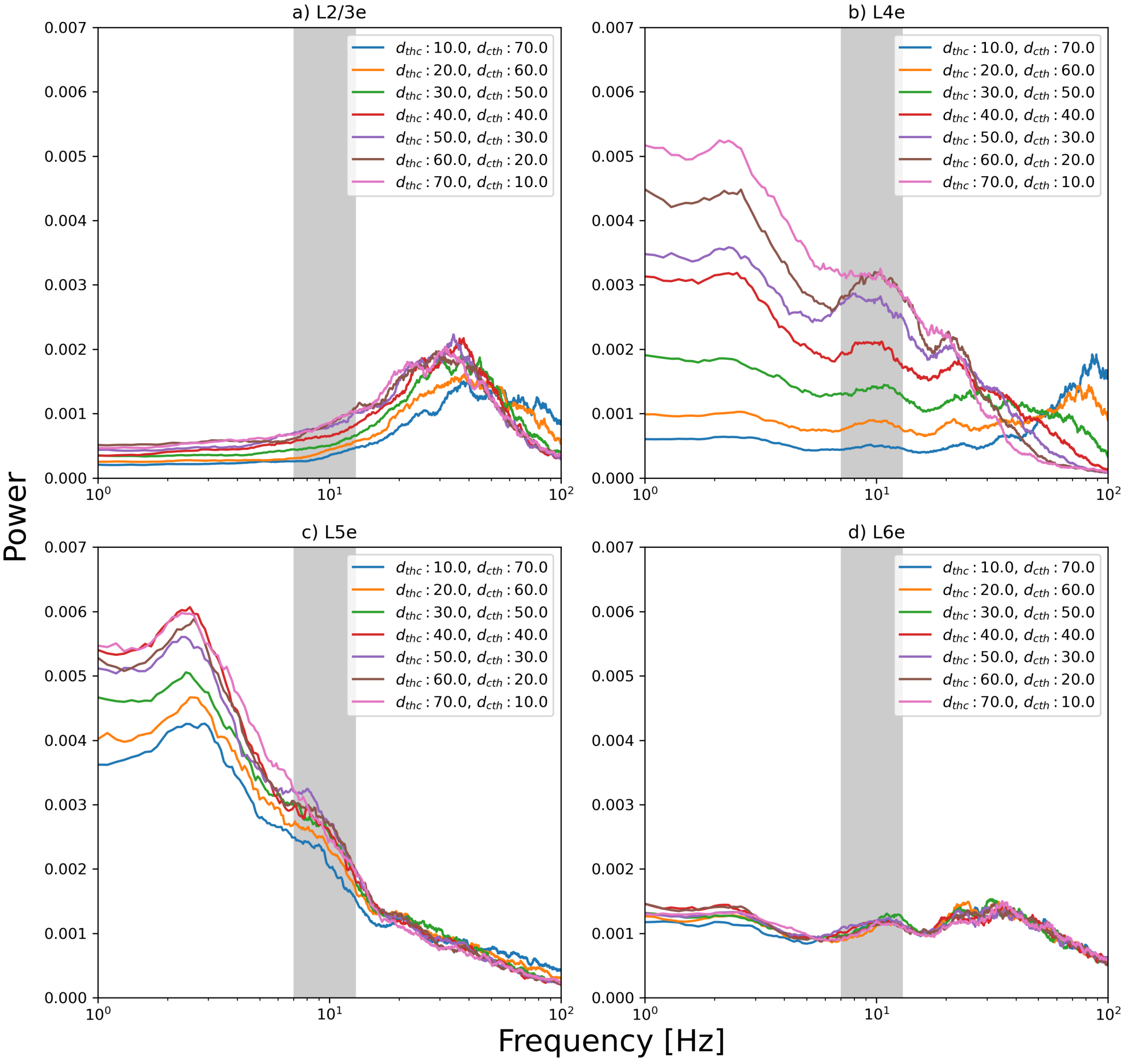

Figura 5.9: ***Population activity power spectra under different thalamocortical loop delays.*** *The power spectra was estimated from the averaged cortical spiking activity of the excitatory neurons by layer for different combinations of thalamocortical and corticothalamic transmission delays.*

Differently on what was shown in the last section, we did not observe a very clear peak at the alpha range at any layer. Still, small peaks which was not present in the isolated V1 network can be observed in layers 4e, 5e and 6e. These peaks are become bigger when increasing the thalamocortical delays. These differences are clear when looking the L4e spiking activity power spectrum (Figure 5.9b). In this case, keeping the total thalamocortical loop delay in 80 ms, when increasing the thalamocortical delay above 30 ms it is possible to observe the emergence of a peak in the alpha range. Moreover, following the latter comparison, another peak emerges between 1 to 2 Hz (also present in L5e - Figure 5.9c) and, by the other hand, fast oscillations are reduced.

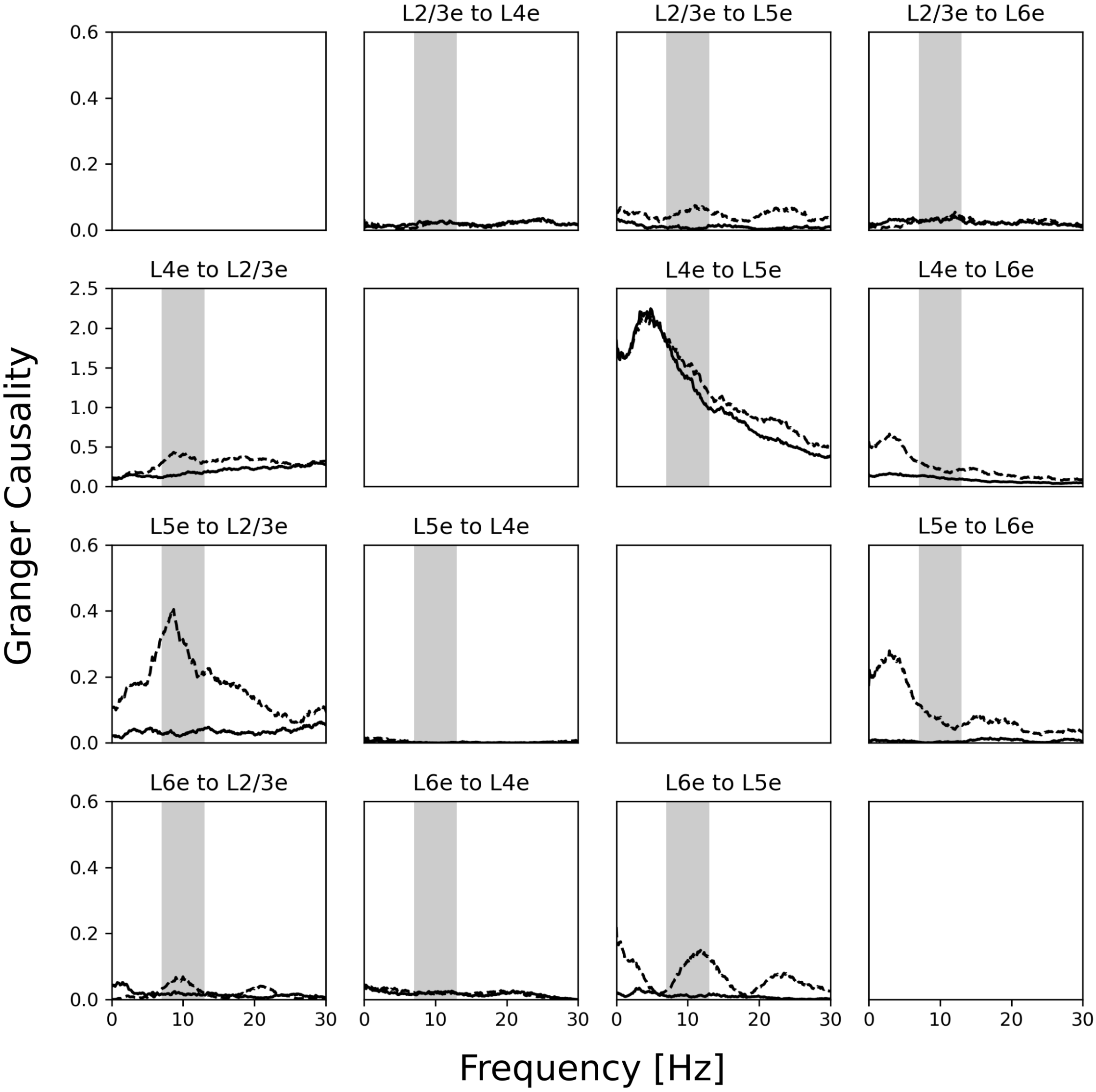

Figura 5.10: ***Granger causality analysis of V1 microcircuit when connected to LGN***. *Granger causality (y-axis) in the frequency domain (x-axis) for the thalamocortical network. Pairwise G-causalities are represented with dashed lines and conditional G-causalities with solid lines.*

We measured the GC and the cGC in Figure 5.10. The main pathway of the alpha rhythm propagation estimated is summarized in Figure 5.11. Similarly with what is reported in experimental findings (Bollimunta et al., 2011), we can observe the alpha propagation coming from the layers which are the main thalamic inputs (L4 and L6). In that way, suggesting the thalamus as a possible alpha generator. Additionally, there is also alpha coming from L5 to L2/3. Nevertheless, the alpha propagation disappears when calculated by the Conditional GC, which could mean that what we got with the pairwise measure was reflect of some correlation between layers activity or the transmission signal was not strong enough to influence and spread the oscillatory behaviour.

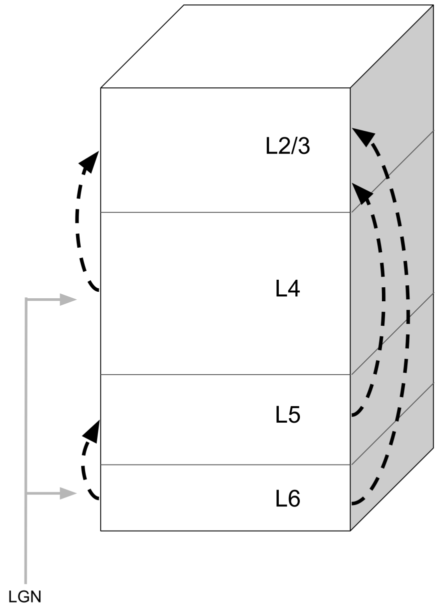

Figura 5.11: ***Schematic draw of the GC analysis of V1 network when connected to LGN***. *Scheme representing the direction of the propagation of alpha rhythm through the cortical layers based on the GC measures. Pairwise G-causalities are represented with dashed arrows while conditional G-causalities with solid lines.*

As we described in the Methods sections we estimated the synaptic strength using the same value of PSP from thalamic neurons to excitatory and inhibitory L4 neurons as experimentally observed for the cat V1 (Sedigh-Sarvestani et al., 2017). Nevertheless, there are other experimental evidence for somatosensory and primary visual cortices which show that the thalamocortical connections into inhibitory L4 neuron are stronger than the ones into excitatory neurons (Gabernet et al., 2005; Gibson et al., 1999; Inoue and Imoto, 2006; Kloc and Maffei, 2014). This information was taken into account and we kept the synaptic weight from TC to L4E cells (w_{ee}) and varied the weight from TC to L4i (w_{ei}). These results are shown in Figures 5.12 and 5.13.

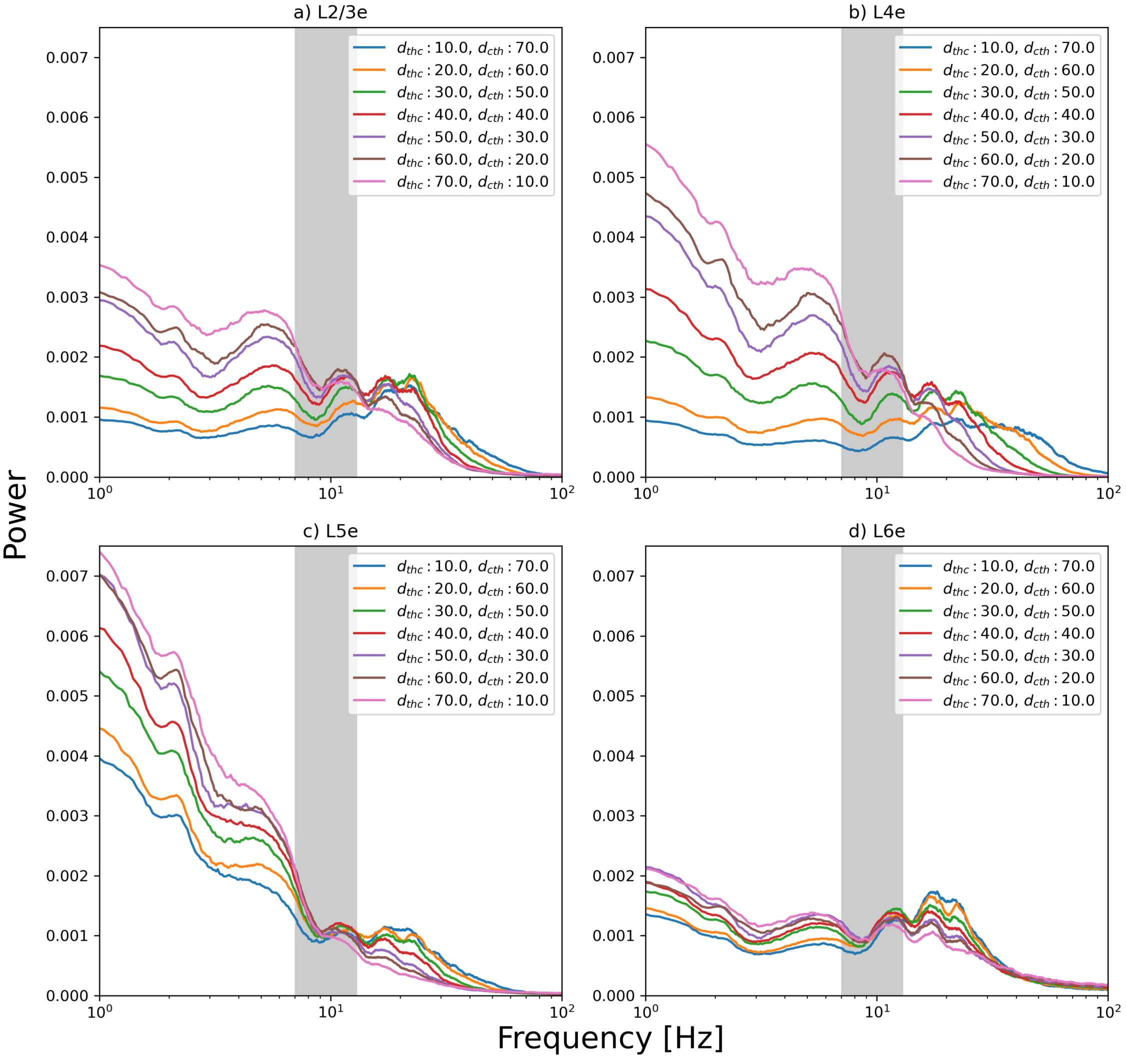

Figura 5.12: ***Cortical population activity power spectra when thalamocortical input is stronger in the excitatory neurons.*** *Power spectra of the averaged cortical activity by layer when synaptic weights from thalamus to cortical inhibitory neurons are half the value of synaptic weight to cortical excitatory ones.*

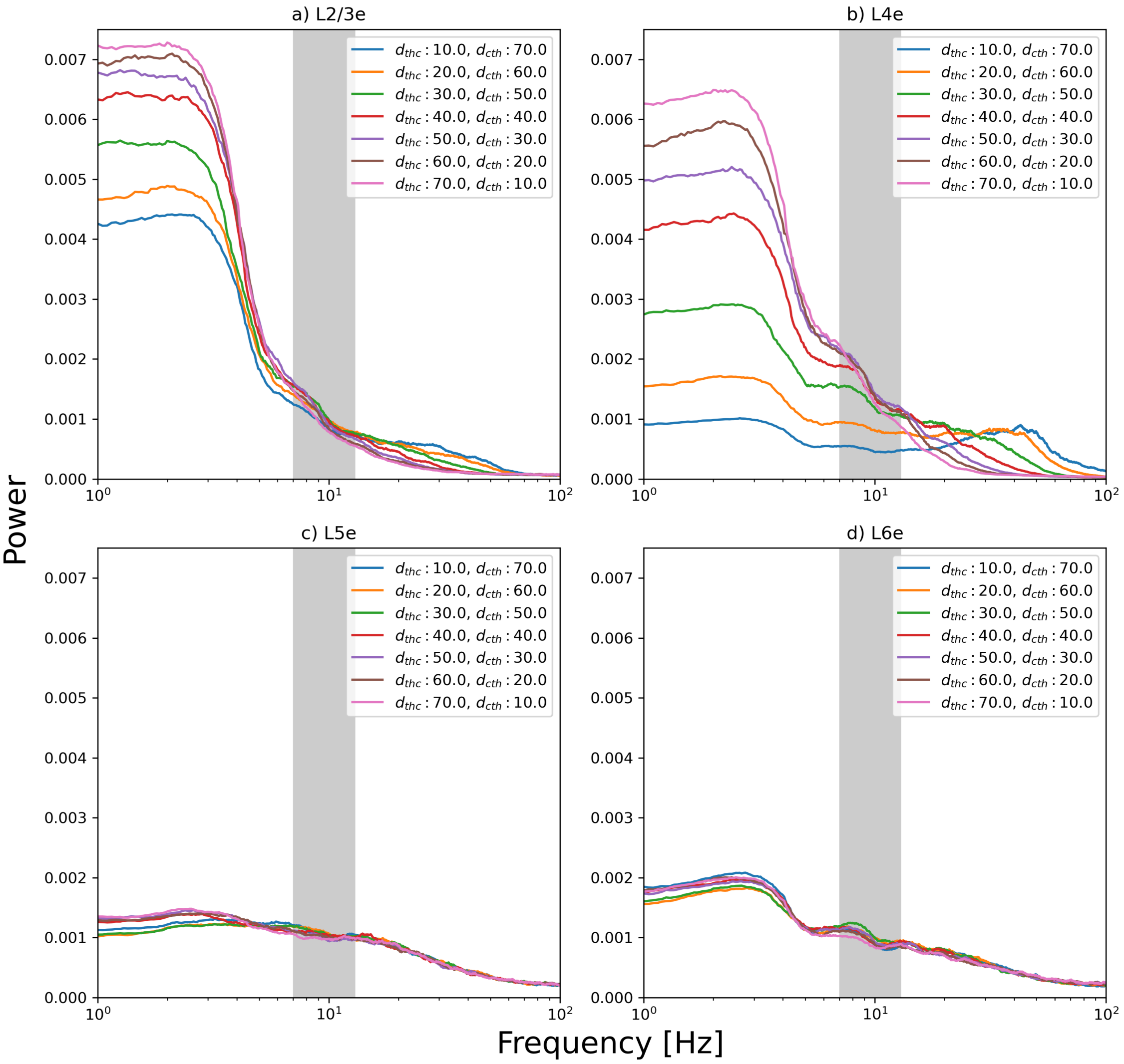

Figura 5.13: ***Cortical population activity power spectra when thalamocortical input is stronger in the inhibitory neurons.*** *Power spectra of the averaged cortical activity by layer when synaptic weights from thalamus to cortical inhibitory neurons are twice the value of synaptic weight to cortical excitatory ones.*

It is possible to observe in Figures 5.12 and 5.13 a dependence of V1 activity due to this balance of thalamocortical connections. Stronger thalamocortical inputs to excitatory neurons increased slow and fast cortical oscillations. In contrast, increasing the synaptic strength from thalamic neurons to cortical inhibitory neurons flattened the curve, keeping small peaks of slow oscillations and decreasing fast oscillations.

5.3.3 Interplay of L5 IB neurons with thalamocortical loop delay

Finally, we put together the two hypothesis including the L5 IB neurons in the thalamocortical network to see the interaction between the two mechanism of alpha generation. As already mentioned, L5 IB neurons are capable to generate strong alpha but for the thalamocortical loop delay the peaks were not very clear. Nevertheless, still there is the question if the thalamocortical interactions are able to modulate or influence the alpha rhythm once it is generated by the L5 pacemakers.

Figure 5.14 shows the power spectra estimated from cortical network spiking activity following the same method as done for Figure 5.9 with the difference that it was introduced IB neurons on cortical L5. For all combinations of thalamocortical and corticothalamic loop delay it is possible to observe peaks at alpha range on power spectra from Figures 5.14 c and d. While in 5.14b the emergence of a peak in the alpha range occurs similarly when L5 IB neurons are absent but with a stronger power. Putting together both mechanisms resulted in a mix of the effects, the thalamocortical delay, as before, induced alpha peaks in L4e and L6e. The L5 IB neurons introduced an alpha peak at L5 and, in general, induced a stronger power where the peaks appeared. Differently on what happened to the other cases, L2/3e presented no peaks in the power spectrum of any combinations of thalamocortical delays with the presence of IB neurons in L5e.

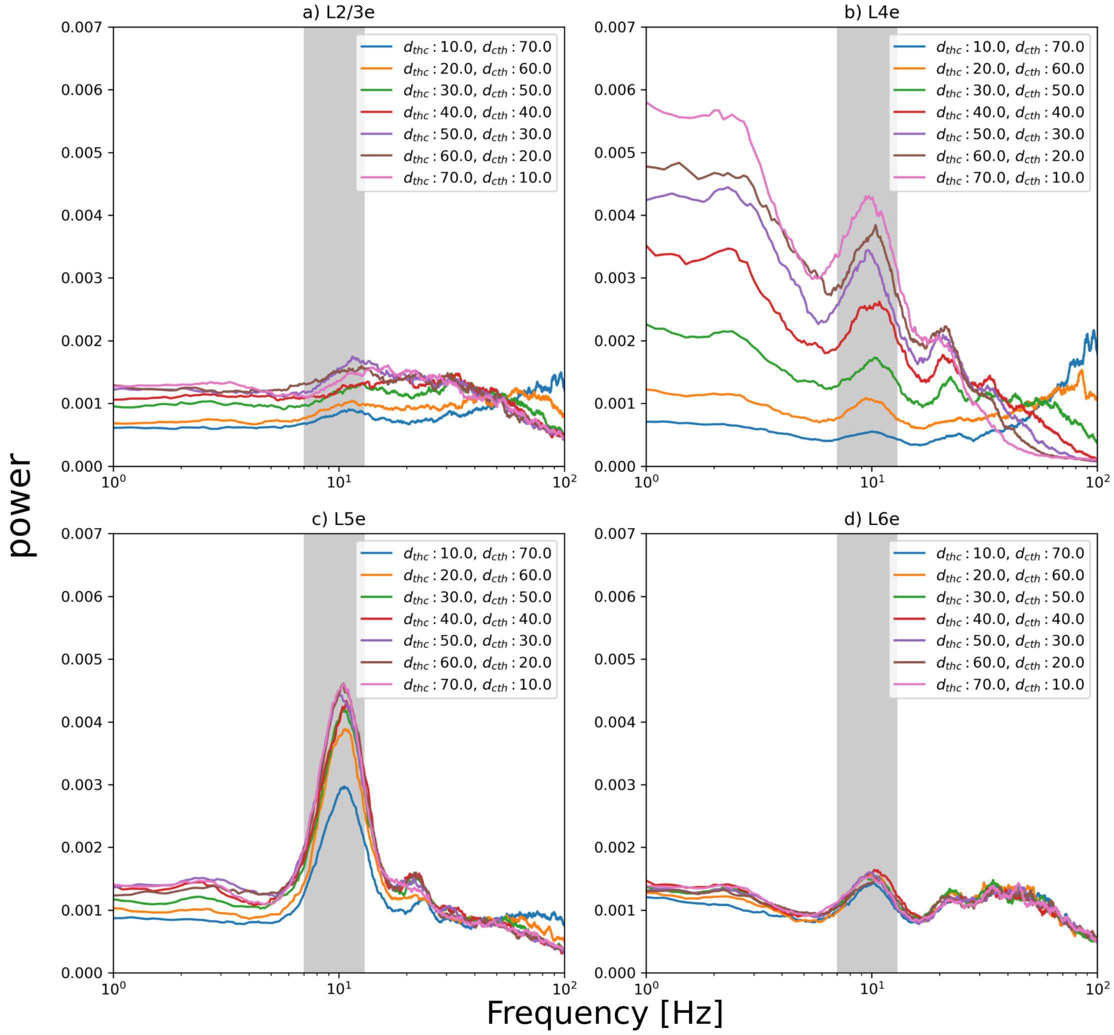

Figura 5.14: ***Cortical population activity power spectra under different thalamocortical loop delays when L5 IB neurons were added.*** *The power spectra were averaged from the cortical spiking activity of the excitatory neurons by layer for different combinations of thalamocortical loop delays when* 50% *of L5e neurons were replaced by IB neurons.*

We also checked the GC and Figure 5.15 shows an example for thalamocortical and corticothalamic delay fixed in 40 ms each. The results observed in Figure 5.15 shows a shift in the direction of the alpha range for the pairwise GC peak from L5e to L2/3e, L5e to L6e and L6e to L5e. However, when the cGC is estimated, only the influence at alpha range from L5e to L2/3e is preserved. Figure 5.16 shows a schematic representation considering only the clear peaks at the alpha range.

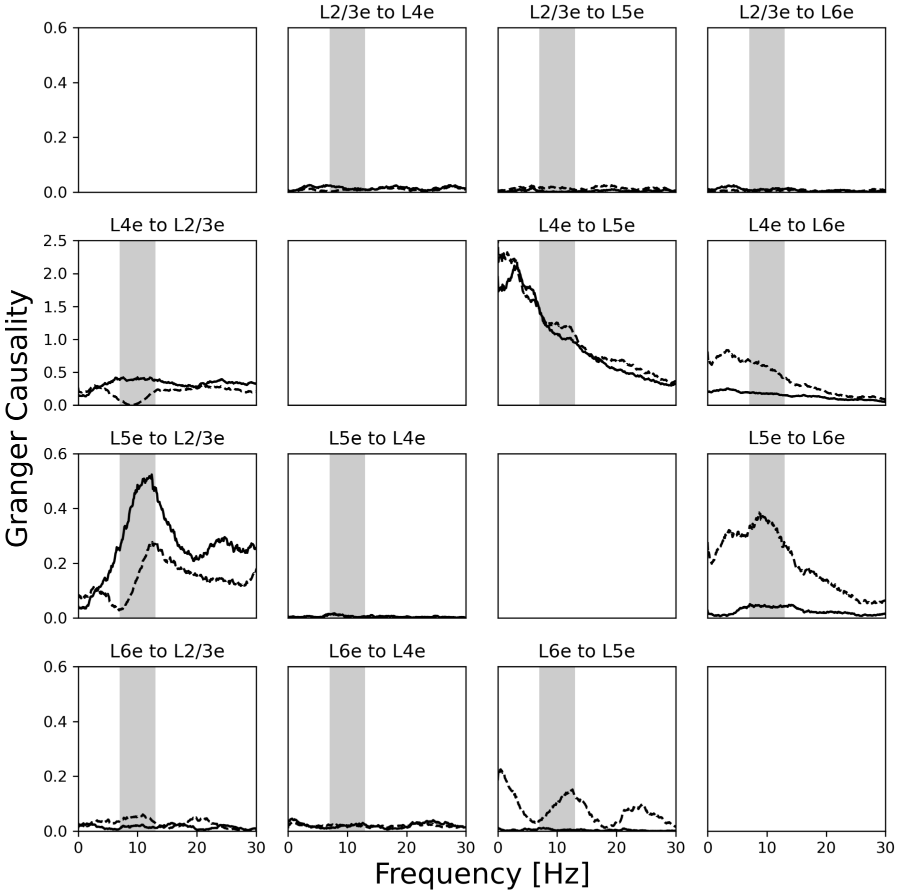

Figura 5.15: ***Granger causality analysis of V1 microcircuit with L5 IB neurons when connected to LGN***. *Granger causality (y-axis) in the frequency domain (x-axis) for the thalamocortical network with the replacement of 50% of layer 5 excitatory cells by IB neurons. Pairwise G-causalities are represented with dashed lines and conditional G-causalities with solid lines.*

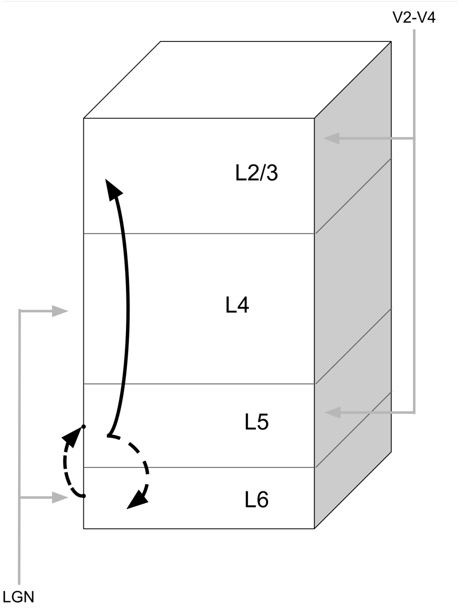

Figura 5.16: *Schematic draw of the GC analysis of V1 network with L5 IB neurons included and connected to LGN*. *Scheme representing the direction of the propagation of alpha rhythm through the cortical layers based on the GC measures. Pairwise GC are represented with dashed arrows while cGC with solid lines. Grey arrows represent the main inputs coming from LGN and other cortical (V2 and V4) areas. The V2 and V4 inputs are merely representative and show the main pathways coming from cortico-cortical connections into V1.*

Chapter 6

Conclusions and perspectives

6.1 Conclusion

The studies in this work can be divided into two parts: the first one is related to the adaptation and changes in the network structure and neuron dynamics simulating spontaneous activity; and the second one concerns protocols of alpha rhythm generation.

This thesis discusses the emergence of oscillatory activity in a multi-layered cortical network connected to the thalamus. Specifically, we looked through the hypothesis of alpha rhythm generation at neuronal and network level in a microcircuit structure of simplified spiking neurons. Our model considers important neurobiological features such as intrinsic neuronal dynamics (e.g. electrophysiological classes: Regular Spiking, Fast Spiking, Intrinsically Bursting, and Rebound Spiking) and multi-layered one-to-one mapping for the cortical structure. We first explored the set of conditions in which the model could present a coherent activity in matters of irregularity and oscillatory behavior when compared with spontaneous neuronal activity collected from experimental data. Then, we studied how two different possible alpha generators could affect the network activity and how they could be compared with experimental data.

The cortical microcircuit used here was extracted from the data-driven multi-area model described by Schmidt et al. (2018a,b), which by its turn, was originally adapted from Potjans and Diesmann (2014). In both versions, all neurons were simulated by the LIF model with the same parameters for excitatory and inhibitory neurons. Here, we used the same V1 structure which includes the number of neurons and connection probabilities, but we improved the neuronal intrinsic properties by including different electrophysiological classes. We used the AdEx model instead of LIF and, distinct parameters were set to excitatory and inhibitory populations. For simplicity, we kept only the most abundant classes, being the RS for excitatory and FS for inhibitory. Features like the emergence of gamma oscillation due to FS cells and the variation of SFA of RS neurons could be achieved in this model. By using this two-dimensional integrate-and-fire neuron model we show that it is possible to have transitions between oscillatory states, which could be used to explore in future studies of conditions commonly referred in the literature as up and down states during slow-wave sleep (Tomov et al., 2014b, 2016b; Pena et al., 2018a; Destexhe, 2009). For this work, we concentrated only on the awake spontaneous activity state.

In this scenario, we used our results of spontaneous activity to validate the V1 network as well as to identify in which conditions of excitation and inhibition balance and extra-cortical background noise firing rate it is possible to achieve "healthy" activity. In addition, this study was done under two different assumptions about background activity: first, considering a specific number of inputs by population with the same background firing rate, and secondly, by keeping the same background firing rate summed with the specific mean firing rates of each non-simulated cortical area at resting state (data from (Schmidt et al., 2018b)). The latter case showed lower power at the gamma range (> 30) than the former. Moreover, the region of parameters of "healthy" activity was wider in the latter case, showing a better fit when using more realistic background activity.

There is recent evidence that the variation of SFA of excitatory neurons mimicking the indirect effect of acetylcholine was enough to make the transition between awake to a slow-wave sleep state in a cortical network (Destexhe, 2009). Nevertheless, although fast oscillations decreased when SFA increased, the slow-wave activity was not observed in our V1 model. The neuron parameters used in our model are similar to the ones in Destexhe (2009), but while we always have a background activity generated by the Poisson distributed spike trains, Destexhe's work only uses an initial stimulus to evoke self-sustained activity. Furthermore, the V1 network structure is much more complex, which could lead to expected differences. Since our goal was not to achieve such sleep state transitions, we did not explore other conditions where this behavior could emerge.

After defining the model parameters, we studied the two hypotheses involved in the alpha rhythm generation. First, IB excitatory neurons at L5 that oscillate in the alpha range were introduced in the isolated V1 network. This resulted in the alpha rhythm pathway coming mainly from L5 and L2/3 similarly to observed pairwise GC measured elsewhere (Bastos et al., 2014; van Kerkoerle et al., 2014). However, when using conditional GC instead of pairwise GC, the only remaining alpha pathway was L5 to L2/3. Anyhow, although the oscillatory behavior was not strong enough to pave visible alpha transmission paths besides L5, it was transmitted to layer 2/3 as observed in the alpha peaks that emerged in their power spectrum (Fig. 5.5).

To study the second hypothesis about the thalamocortical loop delay we connected the V1 microcircuit to LGN and varied the thalamocortical and corticothalamic transmission delays keeping the total sum at 80 ms. While L5 IB neurons induced very clear peaks at the alpha range in the power spectra, the alpha peaks induced by varying the thalamocortical loop delay were smaller. Still, it was possible to identify changes in the power spectra around 10 Hz at layers 4, 5, and 6. Smaller values of thalamocortical transmission delay reduced these peaks and increased peaks at higher frequencies (around 100 Hz). We varied both thalamocortical and corticothalamic delays with the expectation of finding a tendency, even though the thalamocortical connections are usually faster than corticothalamic ones (see Table 2.2). In that way, we considered that the results with thalamocortical delay equal or smaller than the corticothalamic one are biological plausible. Taking the example where both delays are equal to 40 ms, we could get similar alpha transmission pathways as found in experimental references that indicate possible alpha origin from the thalamus (Bollimunta et al., 2011). Nevertheless, as the oscillatory behavior was not very strong, the power spectra and the pairwise GC showed only small peaks at the alpha frequency. Indeed, the strongest influence captured using GC and cGC was at a lower frequency range from L4e to L5e.

Additionally, we showed that stronger thalamocortical inputs to excitatory neurons increase slow and fast cortical oscillations while the increase of synaptic strength from thalamic neurons to cortical inhibitory neurons flattens the curve and keeps small peaks of slow oscillations and decreasing fast oscillations. One possible situation where these synaptic strengths could vary in similar ways is under the effect of synaptic plasticity rules. In our model, we did not apply any kind of synaptic plasticity, but it is known that these connections are dynamic. Thus, similar effects are expected depending on the type of plasticity rule that is applied.

Finally, we mixed both hypotheses and we observed through the power spectra at Figure 5.14 that, as expected, the L5 had the strongest alpha oscillations since IB neurons were included there. Moreover, L5 IB neurons not only helped the emergence of alpha rhythm at L5 but also potentiated this oscillation at L4 and L6. This result showed the possibility that two different alpha sources may coexist and future studies could clarify this relation by adding synaptic plasticity on thalamocortical/corticothalamic connections and/or activating L5 IB neurons in different ways. As explained above, the lack of very strong oscillatory behavior made it difficult to get very clear GC results, being the strongest influence coming from L5e to L2/3e.

In conclusion, we presented an improved version of the V1 microcircuit by adding intrinsic neuronal properties and connecting to a thalamic network. We showed that the model can keep a consistent awake spontaneous activity and is also able to oscillate and transit to different states by varying few parameters. Finally, we presented in this full-scale data-driven model two alpha oscillation generators and we showed how they contribute to the emergence of such rhythm.

6.2 Future perspectives

Improvements and extensions of our model can be done in future studies to explore different scenarios. The oscillatory activity propagation could be benefited from long-range connections as in the multi-area model (Schmidt et al., 2018a,b). Recent studies support the idea of long-range propagation of alpha through the human cortex (Halgren et al., 2019) and it could be implemented by including other cortical areas and adapting the model to human data.

At the microcircuit level, the actual model lacks of horizontal spatiality which can be added in future steps. This feature also improves the propagation of alpha waves and other oscillatory behaviors.

Such studies could be expanded to analyze other oscillations in a similar way by exploring potential mechanisms at different scales. Moreover, interactions among large scale phenomena like feedback and feedforward alpha/gamma oscillations (Michalareas et al., 2016; Bastos et al., 2014, 2015) could be explored since the model already presents oscillations at different ranges (e.g. gamma range, above 30 Hz).

Additionally, other mechanisms at neuronal level mentioned in Tables 1.1 and 1.2 involving cortical neurons (Traub et al., 2020) and/or thalamic neurons (Lorincz et al., 2009; Hughes et al., 2011, 2004) can be included in our network.

In short, the methods and the network model developed in this work provide tools for future improvements and the development of new projects.

References*

Agmon, A., Connors, B. W., Li, Y.-t., Huang, Z. J., Zhang, L. I., Tao, H. W., Ibrahim, L. A., Tao, H. W., and Zhang, L. I. (1992). Correlation between intrinsic firing patterns and thalamocortical synaptic responses of neurons in mouse barrel cortex. *J. Neurosci.*, 12(1):319–29.

Aiken, S. P., Lampe, B. J., Murphy, P. A., and Brown, B. S. (1995). Reduction of spike frequency adaptation and blockade of M-current in rat CA1 pyramidal neurones by linopirdine (DuP 996), a neurotransmitter release enhancer. *Br. J. Pharmacol.*, 115(7):1163–8.

Alivisatos, A. P., Chun, M., Church, G. M., Deisseroth, K., Donoghue, J. P., Greenspan, R. J., McEuen, P. L., Roukes, M. L., Sejnowski, T. J., Weiss, P. S., and Yuste, R. (2013). The brain activity map. *Science*, 339(6125):1284–1285.

Amit, D. J. and Brunel, N. (1997). Model of global spontaneous activity and local structured activity during delay periods in the cerebral cortex. *Cereb. Cortex*, 7(3):237–52.

Amitai, Y. (2001). Thalamocortical synaptic connections: efficacy, modulation, inhibition and plasticity. *Rev. Neurosci.*, 12(2):159–173.

Amunts, K., Knoll, A. C., Lippert, T., Pennartz, C. M. A., Ryvlin, P., Destexhe, A., Jirsa, V. K., D'Angelo, E., and Bjaalie, J. G. (2019). The Human Brain Project — synergy between neuroscience, computing, informatics, and brain-inspired technologies. *PLoS Biol.*, 17(e3000344).

Andersen, P., Morris, R., Amaral, D., Bliss, T., and O'Keefe, J. (2006). *The Hippocampus Book*. Oxford University Press.

---

*De acordo com a Associação Brasileira de Normas Técnicas. NBR 6023.

Arcelli, P., Frassoni, C., REGONDI, M. C., De Biasi, S., Spreafico, R., Biasi, S. D., and Spreafico, R. (1997). GABAergic neurons in mammalian thalamus: a marker of thalamic complexity? *Brain Res. Bull.*, 42(1):27–37.

Arnulfo, G., Wang, S. H., Myrov, V., Toselli, B., Hirvonen, J., Fato, M. M., Nobili, L., Cardinale, F., Rubino, A., Zhigalov, A., Palva, S., and Palva, J. M. (2020). Long-range phase synchronization of high-frequency oscillations in human cortex. *Nat. Commun.*, 11(1):1–15.

Augustinaite, S., Yanagawa, Y., and Heggelund, P. (2011). Cortical feedback regulation of input to visual cortex: Role of intrageniculate interneurons. *J. Physiol.*, 589(12):2963–2977.

Azevedo, F. A. C., Carvalho, L. R. B., Grinberg, L. T., Farfel, J. M., Ferretti, R. E. L., Leite, R. E. P., Jacob Filho, W., Lent, R., and Herculano-Houzel, S. (2009). Equal numbers of neuronal and nonneuronal cells make the human brain an isometrically scaled-up primate brain. *J. Comp. Neurol.*, 513(5):532–541.

Baghdoyan, H. A. and Lydic, R. (1999). M2 muscarinic receptor subtype in the feline medial pontine reticular formation modulates the amount of rapid eye movement sleep. *Sleep*, 22(7):835–47.

Barnett, L. and Seth, A. K. (2011). Behaviour of Granger causality under filtering: Theoretical invariance and practical application. *J. Neurosci. Methods*, 201(2):404–419.

Basser, P. J., Mattiello, J., and LeBihan, D. (1994). Mr diffusion tensor spectroscopy and imaging. *Biophys. J.*, 66(1):259–267.

Bassett, D. S. and Gazzaniga, M. S. (2011). Understanding complexity in the human brain. *Trends Cogn. Sci.*, 15(5):200–209.

Bastos, A. M., Briggs, F., Alitto, H. J., Mangun, G. R., and Usrey, W. M. (2014). Simultaneous Recordings from the Primary Visual Cortex and Lateral Geniculate Nucleus Reveal Rhythmic Interactions and a Cortical Source for Gamma-Band Oscillations. *J. Neurosci.*, 34(22):7639–7644.

Bastos, A. M., Vezoli, J., Bosman, C. A., Schoffelen, J.-M., Oostenveld, R., Dowdall, J. R., De Weerd, P., Kennedy, H., and Fries, P. (2015). Visual areas exert feedforward and feedback influences through distinct frequency channels. *Neuron*, 85(2):390–401.

Bazhenov, M., Timofeev, I., Steriade, M., and Sejnowski, T. J. (2002). Model of thalamocortical slow-wave sleep oscillations and transitions to activated States. *J. Neurosci.*, 22(19):8691–8704.

Bear, M. F., Connors, B. W., and Paradiso, M. A. (2016). *Neuroscience: Exploring the Brain 4th Edition by Mark F. Bear on Storenvy*. Wolters Kluwer Health, fourth edition.

Berkes, P., Orbán, G., Lengyel, M., and Fiser, J. (2011). Spontaneous Cortical Activity Reveals Hallmarks of an Optimal Internal Model of the Environment. *Science (80-.).*, 331(6013):83–87.

Betzel, R. (2020). Network neuroscience and the connectomics revolution. *arXiv preprint arXiv:2010.01591*.

Bezaire, M. J., Raikov, I., Burk, K., Vyas, D., and Soltesz, I. (2016). Interneuronal mechanisms of hippocampal theta oscillations in a full-scale model of the rodent CA1 circuit. *Elife*, 5(DECEMBER2016).

Bhalla, U. S. (2008). PyMOOSE: Interoperable scripting in Python for MOOSE. *Front. Neuroinform.*, 2(DEC):6–6.

Billeh, Y. N., Cai, B., Gratiy, S. L., Dai, K., Iyer, R., Gouwens, N. W., Abbasi-Asl, R., Jia, X., Siegle, J. H., Olsen, S. R., Koch, C., Mihalas, S., and Arkhipov, A. (2020). Systematic Integration of Structural and Functional Data into Multi-scale Models of Mouse Primary Visual Cortex. *Neuron*, 106(3):388–403.e18.

Binzegger, T. (2004). A Quantitative Map of the Circuit of Cat Primary Visual Cortex. *J. Neurosci.*, 24(39):8441–8453.

Blundell, I., Brette, R., Cleland, T. A., Close, T. G., Coca, D., Davison, A. P., Diaz-Pier, S., Fernandez Musoles, C., Gleeson, P., Goodman, D. F. M., Hines, M., Hopkins, M. W., Kumbhar, P., Lester, D. R., Marin, B., Morrison, A., Müller, E., Nowotny, T., Peyser, A., Plotnikov, D., Richmond, P., Rowley, A., Rumpe, B., Stimberg, M., Stokes, A. B., Tomkins, A., Trensch, G., Woodman, M., and Eppler, J. M. (2018). Code Generation in Computational Neuroscience: A Review of Tools and Techniques. *Front. Neuroinform.*, 12:68.

Bollimunta, A., Chen, Y., Schroeder, C. E., and Ding, M. (2008). Neuronal mechanisms of cortical alpha oscillations in awake-behaving macaques. *J. Neurosci.*, 28(40):9976–88.

Bollimunta, A., Mo, J., Schroeder, C. E., and Ding, M. (2011). Neuronal mechanisms and attentional modulation of corticothalamic α oscillations. *J. Neurosci.*, 31(13):4935–43.

Bonelli, R. M. and Cummings, J. L. (2007). Frontal-subcortical circuitry and behavior. *Dialogues Clin. Neurosci.*, 9(2):141–151.

Borges, F., Protachevicz, P., Lameu, E., Bonetti, R., Iarosz, K., Caldas, I., Baptista, M., and Batista, A. (2017). Synchronised firing patterns in a random network of adaptive exponential integrate-and-fire neuron model. *Neural Netw.*, 90:1–7.

Borges, F. S., Protachevicz, P. R., Pena, R. F., Lameu, E. L., Higa, G. S., Kihara, A. H., Matias, F. S., Antonopoulos, C. G., de Pasquale, R., Roque, A. C., Iarosz, K. C., Ji, P., and Batista, A. M. (2020). Self-sustained activity of low firing rate in balanced networks. *Physica A*, 537:122671.

Bortolotto, G. S., Girardi-Schappo, M., Gonsalves, J. J., Pinto, L. T., and Tragtenberg, M. H. R. (2016). Information processing occurs via critical avalanches in a model of the primary visual cortex. *J. Phys. Conf. Ser.*, 686(1):012008.

Bos, H., Diesmann, M., and Helias, M. (2016). Identifying Anatomical Origins of Coexisting Oscillations in the Cortical Microcircuit. *PLoS Comput. Biol.*, 12(10):e1005132.

Boudreau, C. E. (2005). Short-Term Depression in Thalamocortical Synapses of Cat Primary Visual Cortex. *J. Neurosci.*, 25(31):7179–7190.

Bower, J. M. and Beeman, D. (2012). *The Book of GENESIS: Exploring Realistic Neural Models with the GEneral NEural SImulation System*. Springer Science & Business Media.

Bragin, A., Engel, J., Wilson, C. L., Fried, I., and Buzsáki, G. (1999). High-Frequency Oscillations in Human Brain. *Hippocampus*, 9:137–142.

Braitenberg, V. (1974). Thoughts on the cerebral cortex. *J. Theor. Biol.*, 46(2):421–447.

Braitenberg, V. and Schüz, A. (1998). *Cortex: Statistics and Geometry of Neuronal Connectivity*. Springer, Berlin.

Brette, R. and Gerstner, W. (2005a). Adaptive exponential integrate-and-fire model as an effective description of neuronal activity. *J. Neurophysiol.*, 94:3637–3642.

Brette, R. and Gerstner, W. (2005b). Adaptive Exponential Integrate-and-Fire Model as an Effective Description of Neuronal Activity. *J. Neurophysiol.*, 94(5):3637–3642.

Briggs, F. and Usrey, W. M. (2005). Temporal properties of feedforward and feedback pathways between the thalamus and visual cortex in the ferret. *Thalamus Relat. Syst.*, 3(2):133–139.

Briggs, F. and Usrey, W. M. (2009). Parallel Processing in the Corticogeniculate Pathway of the Macaque Monkey. *Neuron*, 62(1):135–146.

Brunel, N. (2000). Dynamics of sparsely connected networks of excitatory and inhibitory spiking neurons. *J. Comput. Neurosci.*, 8(3):183–208.

Brunton, B. W. and Beyeler, M. (2019). Data-driven models in human neuroscience and neuroengineering. *Curr. Opin. Neurobiol.*, 58:21–29.

Bullmore, E. T. and Bassett, D. S. (2011). Brain graphs: graphical models of the human brain connectome. *Annu. Rev. Clin. Psycho.*, 7:113–140.

Buzsáki, G. (2010). Neural syntax: cell assemblies, synapsembles, and readers. *Neuron*, 68(3):362–385.

Buzsáki, G., Anastassiou, C. A., and Koch, C. (2012). The origin of extracellular fields and currents — EEG, ECoG, LFP and spikes. *Nat. Rev. Neurosci.*, 13(6):407–420.

Buzsaki, G. and Draguhn, A. (2004). Neuronal Oscillations in Cortical Networks. *Science (80-.).*, 304(5679):1–4.

Cannon, R. C., O'Donnell, C., and Nolan, M. F. (2010). Stochastic ion channel gating in dendritic neurons: morphology dependence and probabilistic synaptic activation of dendritic spikes. *PLoS Comput. Biol.*, 6:e1000886.

Carvalho, T. T. A., Fontenele, A. J., Girardi-Schappo, M., Feliciano, T., Aguiar, L. A. A., Silva, T. P. L., de Vasconcelos, N. A. P., Carelli, P. V., and Copelli, M. (2021). Subsampled directed-percolation models explain scaling relations experimentally observed in the brain. *Front. Neural Circuits*, 14:576727.

Castellani, G. C., Quinlan, E. M., Cooper, L. N., and Shouval, H. Z. (2001). A biophysical model of bidirectional synaptic plasticity: dependence on AMPA and NMDA receptors. *Proc. Natl. Acad. Sci. USA*, 98:12772–12777.

Castro-Alamancos, M. A. and Connors, B. W. (1997). Thalamocortical synapses. *Prog. Neurobiol.*, 51(6):581–606.

Çavdar, S., Bay, H. H., Yıldız, S. D., Akakın, D., Şirvancı, S., and Onat, F. (2014). Comparison of numbers of interneurons in three thalamic nuclei of normal and epileptic rats. *Neurosci. Bull.*, 30(3):451–460.

Chen, Y., Bressler, S. L., and Ding, M. (2006). Frequency decomposition of conditional Granger causality and application to multivariate neural field potential data. *J. Neurosci. Methods*, 150(2):228–237.

Clayton, M. S., Yeung, N., and Cohen Kadosh, R. (2017). The many characters of visual alpha oscillations. *Eur. J. Neurosci.*

Cleland, B. G., Levick, W. R., Morstyn, R., and Wagner, H. G. (1976). Lateral geniculate relay of slowly conducting retinal afferents to cat visual cortex. *J. Physiol.*, 255(1):299–320.

Clopath, C., Busing, L., Vasilaki, E., and Gerstner, W. (2010). Connectivity reflects coding: a model of voltage-based spike-timing-dependent-plasticity with homeostasis. *Nat. Neurosci.*, 13:344–352.

Compte, A., Sanchez-Vives, M. V., McCormick, D. A., and Wang, X.-J. (2003). Cellular and network mechanisms of slow oscillatory activity (<1 Hz) and wave propagations in a cortical network model. *J. Neurophysiol.*, 89(5):2707–25.

Connors, B. W. and Amitai, Y. (1997). Making waves in the neocortex. *Neuron*, 18(3):347–9.

Connors, B. W. and Gutnick, M. J. (1990). Intrinsic firing patterns of diverse neocortical neurons. *Trends Neurosci.*, 13(3):99–104.

Contreras, D. (2004). Electrophysiological classes of neocortical neurons. *Neural Networks*, 17(5-6):633–646.

Cossart, R., Aronov, D., and Yuste, R. (2003). Attractor dynamics of network UP states in the neocortex. *Nat. 2003 4236937*, 423(6937):283–288.

Cowan, J. D., Neuman, J., and van Drongelen, W. (2016). Wilson–Cowan Equations for Neocortical Dynamics. *J. Math. Neurosci.*, 6(1):1–24.

Crandall, S. R., Cruikshank, S. J., and Connors, B. W. (2015). A Corticothalamic Switch: Controlling the Thalamus with Dynamic Synapses. *Neuron*, 86(3):768–782.

Crone, J. C., Vindiola, M. M., Yu, A. B., Boothe, D. L., Beeman, D., Oie, K. S., and Franaszczuk, P. J. (2019). Enabling Large-Scale Simulations With the GENESIS Neuronal Simulator. *Front. Neuroinform.*, 13:15.

Crook, S., Gleeson, P., Howell, F., Svitak, J., and Silver, R. A. (2007). Morphml: Level 1 of the neuroml standards for neuronal morphology data and model specification. *Neuroinformatics*, 5(2):96–104.

Crook, S. M., Davison, A. P., McDougal, R. A., and Plesser, H. E. (2020). Reproducibility and rigour in computational neuroscience. *Front. Neuroinf.*, 14:23.

Cruikshank, S. J., Lewis, T. J., and Connors, B. W. (2007). Synaptic basis for intense thalamocortical activation of feedforward inhibitory cells in neocortex. *Nat. Neurosci.*, 10(4):462–468.

Dai, K., Gratiy, S. L., Billeh, Y. N., Xu, R., Cai, B., Cain, N., Rimehaug, A. E., Stasik, A. J., Einevoll, G. T., Mihalas, S., Koch, C., and Arkhipov, A. (2020). Brain Modeling ToolKit: An open source software suite for multiscale modeling of brain circuits. *PLOS Comput. Biol.*, 16(11):e1008386.

Davison, A. P., Brüderle, D., Eppler, J., Kremkow, J., Muller, E., Pecevski, D., Perrinet, L., and Yger, P. (2009). PyNN: a common interface for neuronal network simulators. *Front. Neuroinf.*, 2:11.

Dayan, P. and Abbott, L. F. (2001). *Theoretical Neuroscience: Computational and Mathematical Modeling of Neural Systems.* The MIT Press, Cambridge, Massachussetts, USA.

de Gennes, P. G. and Prost, J. (1993). *The Physics of the Liquid Crystals.* Oxford University Press, Oxford, UK.

de Sousa, A. A., Sherwood, C. C., Hof, P. R., and Zilles, K. (2013). Lamination of the lateral geniculate nucleus of catarrhine primates. *Brain. Behav. Evol.*, 81(2):93–108.

Deco, G. and Jirsa, V. K. (2012). Ongoing Cortical Activity at Rest: Criticality, Multistability, and Ghost Attractors. *J. Neurosci.*, 32(10):3366–3375.

Denk, W. and Horstmann, H. (2004). Serial block-face scanning electron microscopy to reconstruct three-dimensional tissue nanostructure. *PLoS Biol.*, 2(11).

Destexhe, A. (2009). Self-sustained asynchronous irregular states and Up-Down states in thalamic, cortical and thalamocortical networks of nonlinear integrate-and-fire neurons. *J. Comput. Neurosci.*, 27(3):493–506.

Destexhe, A., Rudolph, M., Fellous, J.-M., and Sejnowski, T. J. (2001). Fluctuating synaptic conductances recreate in vivo-like activity in neocortical neurons. *Neuroscience*, 107:13–24.

Dhamala, M., Rangarajan, G., and Ding, M. (2008). Estimating Granger Causality from Fourier and Wavelet Transforms of Time Series Data. *Phys. Rev. Lett.*, 100(1):018701.

Ding, M., Chen, Y., and Bressler, S. L. (2006). Granger Causality: Basic Theory and Application to Neuroscience. pages 437–460. Wiley-VCH Verlag GmbH & Co. KGaA, Weinheim, Germany.

Dura-Bernal, S., Neymotin, S., Suter, B., Shepherd, G., and Lytton, W. (2017). Multiscale dynamics and information flow in a data-driven model of the primary motor cortex microcircuit. *bioRxiv*, page 201707.

Dura-Bernal, S., Suter, B. A., Gleeson, P., Cantarelli, M., Quintana, A., Rodriguez, F., Kedziora, D. J., Chadderdon, G. L., Kerr, C. C., Neymotin, S. A., McDougal, R. A., Hines, M., Shepherd, G. M., and Lytton, W. W. (2019). Netpyne, a tool for data-driven multiscale modeling of brain circuits. *Elife*, 8:e44494.

Eckenstein, F., Baughman, R., and Quinn, J. (1988). An anatomical study of cholinergic innervation in rat cerebral cortex. *Neuroscience*, 25(2):457–474.

El Boustani, S., Pospischil, M., Rudolph-Lilith, M., and Destexhe, A. (2007). Activated cortical states: Experiments, analyses and models. *J. Physiol. Paris*, 101(1-3):99–109.

Eppler, J. M., Helias, M., Muller, E., Diesmann, M., and Gewaltig, M.-O. (2009). Pynest: a convenient interface to the nest simulator. *Front. Neuroinform.*, 2:12.

Erisir, A., Van Horn, S. C., and Sherman, S. M. (1997). Relative numbers of cortical and brainstem inputs to the lateral geniculate nucleus. *Proc. Natl. Acad. Sci.*, 94(4):1517–1520.

Essink, S., Senk, J., Plesser, H. E., Helin, R., Diesmann, M., Helias, M., Grün, S., van Albada, S., Tetzlaff, T., and Shimoura, R. (2020). Ultra-high frequency spectrum of neuronal activity. *Bernstein Konf. 2020.*

Ferster, D. and Lindström, S. (1983). An intracellular analysis of geniculo-cortical connectivity in area 17 of the cat. *J. Physiol.*, 342(1):181–215.

Fetz, E., Toyama, K., and Smith, W. (1991). Synaptic Interactions between Cortical Neurons. pages 1–47.

Fitzpatrick, D., Penny, G. R., and Schmechel, D. E. (1984). Glutamic acid decarboxylase-immunoreactive neurons and terminals in the lateral geniculate nucleus of the cat. *J. Neurosci.*, 4(7):1809–1829.

Gabernet, L., Jadhav, S. P., Feldman, D. E., Carandini, M., and Scanziani, M. (2005). Somatosensory Integration Controlled by Dynamic Thalamocortical Feed-Forward Inhibition. *Neuron*, 48(2):315–327.

Garcia-Marin, V., Kelly, J. G., and Hawken, M. J. (2017). Major Feedforward Thalamic Input Into Layer 4C of Primary Visual Cortex in Primate. *Cereb. Cortex*, 29(1):1–16.

Gentet, L. J. and Ulrich, D. (2004). Electrophysiological characterization of synaptic connections between layer VI cortical cells and neurons of the nucleus reticularis thalami in juvenile rats. *Eur. J. Neurosci.*, 19(3):625–633.

Gerstner, W. and Brette, R. (2009). Adaptive exponential integrate-and-fire model. *Scholarpedia*, 4(6):8427.

Gerstner, W., Kistler, W. M., Naud, R., and Paninski, L. (2014). *Neuronal dynamics : from single neurons to networks and models of cognition.*

Gewaltig, M.-O. and Diesmann, M. (2007). NEST (NEural Simulation Tool). *Scholarpedia*, 2(4):1430.

Geweke, J. (1982). Measurement of Linear Dependence and Feedback between Multiple Time Series. *J. Am. Stat. Assoc.*, 77(378):304–313.

Geweke, J. F. (1984). Measures of Conditional Linear Dependence and Feedback Between Time Series. *J. Am. Stat. Assoc.*, 79(388):907.

Gibson, J. R., Beierlein, M., and Connors, B. W. (1999). Two networks of electrically coupled inhibitory neurons in neocortex. *Nature*, 402(6757):75–79.

Girardi-Schappo, M., Bortolotto, G. S., Gonsalves, J. J., Pinto, L. T., and Tragtenberg, M. H. R. (2016). Griffiths phase and long-range correlations in a biologically motivated visual cortex model. *Sci. Rep.*, 6:29561.

Girardi-Schappo, M., Bortolotto, G. S., Stenzinger, R. V., Gonsalves, J. J., and Tragtenberg, M. H. R. (2017). Phase diagrams and dynamics of a computationally efficient map-based neuron model. *PLoS ONE*, 12:e0174621.

Girardi-Schappo, M. and de Andrade Costa, A. (2020). Hints from statistical physics and graph theory to build synthetic connectomes: Comment on "what would a synthetic connectome look like?" by i. rabinowitch. *Phys. Life Rev.*, 33:19–21.

Girardi-Schappo, M. and Tragtenberg, M. H. R. (2018). Measuring neuronal avalanches in disordered systems with absorbing states. *Phys. Rev. E*, 97:042415.

Girardi-Schappo, M., Tragtenberg, M. H. R., and Kinouchi, O. (2013). A brief history of excitable map-based neurons and neural networks. *J. Neurosci. Meth.*, 220:116–130.

Glaser, J. R. and Glaser, E. M. (1990). Neuron imaging with neurolucida—a pc-based system for image combining microscopy. *Comput. Med. Imag. Grap.*, 14(5):307–317.

Gleeson, P., Steuber, V., and Silver, R. A. (2007). neuroconstruct: a tool for modeling networks of neurons in 3d space. *Neuron*, 54(2):219–235.

Goldman, J. S., Tort-Colet, N., di Volo, M., Susin, E., Bouté, J., Dali, M., Carlu, M., Nghiem, T.-A., Górski, T., and Destexhe, A. (2019). Bridging Single Neuron Dynamics to Global Brain States. *Front. Syst. Neurosci.*, 0:75.

Gramfort, A., Luessi, M., Larson, E., Engemann, D. A., Strohmeier, D., Brodbeck, C., Goj, R., Jas, M., Brooks, T., Parkkonen, L., and Hämäläinen, M. S. (2013). MEG and EEG data analysis with MNE-Python. *Frontiers in Neuroscience*, 7(267):1–13.

Granger, C. W. J. (1969). Investigating Causal Relations by Econometric Models and Cross-spectral Methods. *Econometrica*, 37(3):424.

Granseth, B. and Lindström, S. (2003). Unitary EPSCs of Corticogeniculate Fibers in the Rat Dorsal Lateral Geniculate Nucleus In Vitro. *J. Neurophysiol.*, 89(6):2952–2960.

Gratiy, S. L., Billeh, Y. N., Dai, K., Mitelut, C., Feng, D., Gouwens, N. W., Cain, N., Koch, C., Anastassiou, C. A., and Arkhipov, A. (2018). Bionet: A python interface to neuron for modeling large-scale networks. *PLoS ONE*, 13(8):e0201630.

Guido, W., Lu, S. M., and Sherman, S. M. (1992). Relative contributions of burst and tonic responses to the receptive field properties of lateral geniculate neurons in the cat. *J. Neurophysiol.*, 68(6):2199–2211.

Guido, W., Lu, S. M., Vaughan, J. W., Godwin, D. W., and Sherman, S. M. (1995). Receiver operating characteristic (ROC) analysis of neurons in the cat's lateral geniculate nucleus during tonic and burst response mode. *Vis. Neurosci.*, 12(4):723–741.

Gutzen, R., von Papen, M., Trensch, G., Quaglio, P., Grün, S., and Denker, M. (2018). Reproducible Neural Network Simulations: Statistical Methods for Model Validation on the Level of Network Activity Data. *Front. Neuroinform.*, 12:90.

Haegens, S., Barczak, A., Musacchia, G., Lipton, M. L., Mehta, A. D., Lakatos, P., and Schroeder, C. E. (2015). Laminar Profile and Physiology of the α Rhythm in Primary Visual, Auditory, and Somatosensory Regions of Neocortex. *J. Neurosci.*, 35(42):14341–52.

Hagberg, A. A., Schult, D. A., and Swart, P. J. (2008). Exploring network structure, dynamics, and function using NetworkX. In Varoquaux, G., Vaught, T., and Millman, J., editors, *Proceedings of the 7th Python in Science Conference*, Pasadena, CA USA.

Halgren, M., Ulbert, I., Bastuji, H., Fabó, D., Eross, L., Rey, M., Devinsky, O., Doyle, W. K., Mak-McCully, R., Halgren, E., Wittner, L., Chauvel, P., Heit, G., Eskandar, E., Mandell, A., and Cash, S. S. (2019). The generation and propagation of the human alpha rhythm. *Proc. Natl. Acad. Sci. U. S. A.*, 116(47):23772–23782.

Harris, K. D. and Thiele, A. (2011). Cortical state and attention. *Nat. Rev. Neurosci. 2011 129*, 12(9):509–523.

Heitmann, S., Aburn, M. J., and Breakspear, M. (2018). The brain dynamics toolbox for matlab. *Neurocomput.*, 315:82–88.

Helin, R., Essink, S., Bos, H., Hagen, E., Helias, M., Senk, J., Tetzlaff, T., van Albada, S. J., Diesmann, M., Grün, S., and Plesser, H. E. (2019). Conditions for and detectability of extremely fast oscillations in neuronal activity. In *2019 Neurosci. Meet. Plan.*, Chicago, IL. Society for Neuroscience, 2019.

Henny, P. and Jones, B. E. (2008). Projections from basal forebrain to prefrontal cortex comprise cholinergic, GABAergic and glutamatergic inputs to pyramidal cells or interneurons. *Eur. J. Neurosci.*, 27(3):654–70.

Herz, A. V., Gollisch, T., Machens, C. K., and Jaeger, D. (2006). Modeling single-neuron dynamics and computations: A balance of detail and abstraction.

Hesse, J. and Gross, T. (2014). Self-organized criticality as a fundamental property of neural systems. *Front. Syst. Neurosci.*, 8:166.

Hickey, T. L. and Guillery, R. W. (1979). Variability of laminar patterns in the human lateral geniculate nucleus. *J. Comp. Neurol.*, 183(2):221–246.

Hill, S. and Tononi, G. (2004). Modeling Sleep and Wakefulness in the Thalamocortical System. *J. Neurophysiol.*, 93(3):1671–1698.

Hill, S. and Tononi, G. (2005). {M}odeling sleep and wakefulness in the thalamocortical system. *J. Neurophysiol.*, 93(3):1671–1698.

Hines, M., Davison, A. P., and Muller, E. (2009). Neuron and python. *Front. Neuroinform.*, 3:1.

Hines, M. L. and Carnevale, N. T. (1997). The NEURON Simulation Environment.

Hines, M. L., Morse, T., Migliore, M., Carnevale, N. T., and Shepherd, G. M. (2004). Modeldb: a database to support computational neuroscience. *J. Comput. Neurosci.*, 17(1):7–11.

Hodgkin, A. L. and Huxley, A. F. (1952). A quantitative description of membrane current and its application to conduction and excitation in nerve. *J. Physiol.*, 117(4):500.

Holcman, D. and Tsodyks, M. (2006). The Emergence of Up and Down States in Cortical Networks. *PLOS Comput. Biol.*, 2(3):e23.

Howe, W. M., Gritton, H. J., Lusk, N. A., Roberts, E. A., Hetrick, V. L., Berke, J. D., and Sarter, M. (2017). Acetylcholine Release in Prefrontal Cortex Promotes Gamma Oscillations and Theta-Gamma Coupling during Cue Detection. *J. Neurosci.*, 37(12):3215–3230.

Hughes, S., Lőrincz, M., Turmaine, M., and Crunelli, V. (2011). Thalamic gap junctions control local neuronal synchrony and influence macroscopic oscillation amplitude during EEG alpha rhythms. *Front. Psychol.*, 2:193.

Hughes, S. W., Cope, D. W., Blethyn, K. L., and Crunelli, V. (2002). Cellular mechanisms of the slow (<1 Hz) oscillation in thalamocortical neurons in vitro. *Neuron*, 33(6):947–958.

Hughes, S. W., Lörincz, M., Cope, D. W., Blethyn, K. L., Kékesi, K. A., Parri, H., Juhász, G., and Crunelli, V. (2004). Synchronized Oscillations at α and θ Frequencies in the Lateral Geniculate Nucleus. *Neuron*, 42(2):253–268.

Inoue, T. and Imoto, K. (2006). Feedforward Inhibitory Connections From Multiple Thalamic Cells to Multiple Regular-Spiking Cells in Layer 4 of the Somatosensory Cortex. *J. Neurophysiol.*, 96(4):1746–1754.

Izhikevich, E. M. (2003). Simple model of spiking neurons. *IEEE Trans. Neural Networks*, 14(6):1569–1572.

Izhikevich, E. M. (2007). *Dynamical Systems in Neuroscience*. The MIT Press, Cambridge, Massachussetts, USA.

Izhikevich, E. M. and Edelman, G. M. (2008). Large-scale model of mammalian thalamocortical systems. *Proc. Natl. Acad. Sci. U. S. A.*, 105(9):3593–3598.

Jercog, D., Roxin, A., Barthó, P., Luczak, A., Compte, A., and de la Rocha, J. (2017). UP-DOWN cortical dynamics reflect state transitions in a bistable network. *Elife*, 6:1–33.

Johnston, D. and Wu, S. M. S. (1995). *Foundations of Cellular Neurophysiology*. The MIT Press, Cambridge, MA.

Jones, M. S., MacDonald, K. D., Choi, B., Dudek, F. E., and Barth, D. S. (2000). Intracellular Correlates of Fast (>200 Hz) Electrical Oscillations in Rat Somatosensory Cortex. *https://doi.org/10.1152/jn.2000.84.3.1505*, 84(3):1505–1518.

Jones, S. R., Pritchett, D. L., Sikora, M. A., Stufflebeam, S. M., Hämäläinen, M., and Moore, C. I. (2009). Quantitative Analysis and Biophysically Realistic Neural Modeling of the MEG Mu Rhythm: Rhythmogenesis and Modulation of Sensory-Evoked Responses. *J. Neurophysiol.*, 102(6):3554–3572.

Jordan, J., Mørk, H., Vennemo, S. B., Terhorst, D., Peyser, A., Ippen, T., Deepu, R., Eppler, J. M., van Meegen, A., Kunkel, S., Sinha, A., Fardet, T., Diaz, S., Morrison, A., Schenck, W., Dahmen, D., Pronold, J., Stapmanns, J., Trensch, G., Spreizer, S., Mitchell, J., Graber, S., Senk, J., Linssen, C., Hahne, J., Serenko, A., Naoumenko, D., Thomson, E., Kitayama, I., Berns, S., and Plesser, H. E. (2019). NEST 2.18.0.

Kaas, J. H., Huerta, M. F., Weber, J. T., and Harting, J. K. (1978). Patterns of retinal terminations and laminar organization of the lateral geniculate nucleus of primates. *J. Comp. Neurol.*, 182(3):517–553.

Kaiser, M., Görner, M., and Hilgetag, C. C. (2007). Criticality of spreading dynamics in hierarchical cluster networks without inhibition. *New J. Phys.*, 9(5):110–110.

Kaiser, M. and Hilgetag, C. C. (2010). Optimal hierarchical modular topologies for producing limited sustained activation of neural networks. *Front. Neuroinform.*, 4:8.

Kajiwara, R., Wouterlood, F. G., Sah, A., Boekel, A. J., Baks-te Bulte, L. T., and Witter, M. P. (2008). Convergence of entorhinal and ca3 inputs onto pyramidal neurons and interneurons in hippocampal area ca1—an anatomical study in the rat. *Hippocampus*, 18(3):266–280.

Kalmbach, A., Hedrick, T., and Waters, J. (2012). Selective optogenetic stimulation of cholinergic axons in neocortex. *J. Neurophysiol.*, 107(7):2008–19.

Kamiński, M. and Liang, H. (2005). Causal influence: Advances in neurosignal analysis.

Kandel, A. and Buzsáki, G. (1997). Cellular–Synaptic Generation of Sleep Spindles, Spike-and-Wave Discharges, and Evoked Thalamocortical Responses in the Neocortex of the Rat. *J. Neurosci.*, 17(17):6783–6797.

Kandel, E., Schwartz, J., Jessell, T., Siegelbaum, S., and Hudspeth, A. (2014). *Princípios de Neurociências - 5.ed.* AMGH Editora.

Kandel, E. R., Markram, H., Matthews, P. M., Yuste, R., and Koch, C. (2013). Neuroscience thinks big (and collaboratively). *Nat. Rev. Neurosci.*, 14(9):659–664.

Kawaguchi, Y. and Kubota, Y. (1997). Gabaergic cell subtypes and their synaptic connections in rat frontal cortex. *Cereb. Cortex*, 7(6):476–486.

Kepecs, A., van Rossum, M. C., Song, S., and Tegner, J. (2002). Spike-timing-dependent plasticity: common themes and divergent vistas. *Biol. Cybern.*, 87(5-6):446–458.

Kleberg, F. I., Fukai, T., and Gilson, M. (2014). Excitatory and inhibitory stdp jointly tune feedforward neural circuits to selectively propagate correlated spiking activity. *Front. Comput. Neurosci.*, 8:53.

Kloc, M. and Maffei, A. (2014). Target-Specific Properties of Thalamocortical Synapses onto Layer 4 of Mouse Primary Visual Cortex. *J. Neurosci.*, 34(46):15455–15465.

Koch, C. and Laurent, G. (1999). Complexity and the nervous system.

Kopell, N., Ermentrout, G. B., Whittington, M. A., and Traub, R. D. (2000). Gamma rhythms and beta rhythms have different synchronization properties. *Proc. Natl. Acad. Sci. U. S. A.*, 97(4):1867–1872.

Kriener, B., Enger, H., Tetzlaff, T., Plesser, H. E., Gewaltig, M.-O., and Einevoll, G. T. (2014). Dynamics of self-sustained asynchronous-irregular activity in random networks of spiking neurons with strong synapses. *Front. Comput. Neurosci.*, 0(October):136.

Kumar, A., Schrader, S., Aertsen, A., and Rotter, S. (2008). The high-conductance state of cortical networks. *Neural Comput.*, 20(1):1–43.

Kunkel, S., Schmidt, M., Eppler, J. M., Plesser, H. E., Masumoto, G., Igarashi, J., Ishii, S., Fukai, T., Morrison, A., Diesmann, M., and Helias, M. (2014). Spiking network simulation code for petascale computers. *Front. Neuroinform.*, 8:78.

Kuypers, H. and Ugolini, G. (1990). Viruses as transneuronal tracers. *Trends Neurosci.*, 13(2):71–75.

Lameu, E. L., Batista, C., Batista, A., Iarosz, K., Viana, R., Lopes, S., and Kurths, J. (2012). Suppression of bursting synchronization in clustered scale-free (rich-club) neuronal networks. *Chaos*, 22:043149.

Lameu, E. L., Borges, F. S., Iarosz, K. C., Protachevicz, P. R., Batista, A. M., Antonopoulos, C. G., and Macau, E. E. N. (2019). Short-term and spike-timing-dependent plasticities facilitate the formation of modular neural networks. *arXiv*, pages 1911.00052 [q–bio.NC].

Landau, I. D., Egger, R., Dercksen, V. J., Oberlaender, M., and Sompolinsky, H. (2016). The Impact of Structural Heterogeneity on Excitation-Inhibition Balance in Cortical Networks. *Neuron*, 92(5):1106–1121.

Landhuis, E. (2017). Neuroscience: big brain, big data. *Nature*, 541:559–561.

Latham, P. E., Richmond, B. J., Nelson, P. G., and Nirenberg, S. (2000). Intrinsic dynamics in neuronal networks. I. Theory. *J. Neurophysiol.*, 83(2):808–827.

Lemieux, M., Chen, J.-Y., Lonjers, P., Bazhenov, M., and Timofeev, I. (2014). The impact of cortical deafferentation on the neocortical slow oscillation. *J. Neurosci.*, 34(16):5689–703.

Leske, S., Tse, A., Oosterhof, N. N., Hartmann, T., Müller, N., Keil, J., and Weisz, N. (2014). The strength of alpha and beta oscillations parametrically scale with the strength of an illusory auditory percept. *Neuroimage*, 88:69–78.

LeVay, S. and Ferster, D. (1979). Proportion of interneurons in the cat's lateral geniculate nucleus. *Brain Res.*, 164(1):304–308.

Levenstein, D., Buzsáki, G., and Rinzel, J. (2019). NREM sleep in the rodent neocortex and hippocampus reflects excitable dynamics. *Nat. Commun.*, 10(1):1–12.

Leão, R. N., Mikulovic, S., Leão, K. E., Munguba, H., Gezelius, H., Enjin, A., Patra, K., Eriksson, A., Loew, L. M., Tort, A. B., and Kullander, K. (2012). OLM interneurons differentially modulate CA3 and entorhinal inputs to hippocampal CA1 neurons. *Nat. Neurosci.*, 15:1524—-1530.

Li, Y. T., Zhou, M., Tao, H. W., and Zhang, L. I. (2013). Intracortical multiplication of thalamocortical signals in mouse auditory cortex. *Nat. Neurosci.*, 16:1179–1181.

Lien, A. D. and Scanziani, M. (2013). Tuned thalamic excitation is amplified by visual cortical circuits. *Nat. Neurosci.*, 16:1315–1323.

Liley, D. T. J. (2015). Neural population model. In Jaeger, D. and Jung, R., editors, *Encyclopedia of Computational Neuroscience*, pages 1898–1912. Springer, New York, NY.

Lima, V., Dellajustina, F. J., Shimoura, R. O., Girardi-Schappo, M., Kamiji, N. L., Pena, R. F., Roque, A. C., Jaiara Dellajustina, F., Shimoura, R. O., Girardi-Schappo, M., Kamiji, N. L., O Pena, R. F., and Roque, A. C. (2020). Granger causality in the frequency domain: derivation and applications. *Rev. Bras. Ensino Física*, 42:20200007.

Lin, M. and Chen, T. (2005). Self-organized criticality in a simple model of neurons based on small-world networks. *Phys. Rev. E*, 71:016133.

Litwin-Kumar, A. and Doiron, B. (2012). Slow dynamics and high variability in balanced cortical networks with clustered connections. *Nat. Neurosci. 2012 1511*, 15(11):1498–1505.

Livingstone, M. and Hubel, D. (1988). Segregation of form, color, movement, and depth: anatomy, physiology, and perception. *Science*, 240(4853):740–9.

Llinás, R. R. and Steriade, M. (2006). Bursting of thalamic neurons and states of vigilance. *J. Neurophysiol.*, 95(6):3297–308.

Lopes da Silva, F. (1991). Neural mechanisms underlying brain waves: from neural membranes to networks. *Electroencephalogr. Clin. Neurophysiol.*, 79(2):81–93.

Lorincz, M. L., Kékesi, K. A., Juhász, G., Crunelli, V., and Hughes, S. W. (2009). Temporal framing of thalamic relay-mode firing by phasic inhibition during the alpha rhythm. *Neuron*, 63(5):683–96.

Luczak, A., Barthó, P., Marguet, S. L., Buzsáki, G., and Harris, K. D. (2007). Sequential structure of neocortical spontaneous activity in vivo. *Proc. Natl. Acad. Sci.*, 104(1):347–352.

MacLean, J. N., Fenstermaker, V., Watson, B. O., and Yuste, R. (2006). A visual thalamocortical slice. *Nat. Methods*, 3(2):129–134.

Madarász, M., Somogyi, G., Somogyi, J., and Hámori, J. (1985). Numerical estimation of γ-aminobutyric acid (GABA)-containing neurons in three thalamic nuclei of the cat: Direct GABA immunocytochemistry. *Neurosci. Lett.*, 61(1-2):73–78.

Maksimov, A., Diesmann, M., and van Albada, S. J. (2018). Criteria on Balance, Stability, and Excitability in Cortical Networks for Constraining Computational Models. *Front. Comput. Neurosci.*, 12:44.

Malekpour, S. and Sethares, W. A. (2015). Conditional Granger causality and partitioned Granger causality: differences and similarities. *Biol. Cybern.*, 109(6):627–637.

Maller, J. J., Welton, T., Middione, M., Callaghan, F. M., Rosenfeld, J. V., and Grieve, S. M. (2019). Revealing the hippocampal connectome through super-resolution 1150-direction diffusion mri. *Sci. Rep.*, 9(1):1–13.

Mallinson, J. B., Shirai, S., Acharya, S. K., Bose, S. K., Galli, E., and Brown, S. A. (2019). Avalanches and criticality in self-organized nanoscale networks. *Sci. Adv.*, 5:eaaw8438.

Malpeli, J. G., Lee, D., and Baker, F. H. (1996). Laminar and retinotopic organization of the macaque lateral geniculate nucleus: Magnocellular and parvocellular magnification functions. *J. Comp. Neurol.*, 375(3):363–377.

Mao, B.-Q., Hamzei-Sichani, F., Aronov, D., Froemke, R. C., and Yuste, R. (2001). Dynamics of Spontaneous Activity in Neocortical Slices. *Neuron*, 32(5):883–898.

Markram, H. (2006). The Blue Brain Project. *Nat. Rev. Neurosci.*, 7(153–160).

Markram, H., Lübke, J., Frotscher, M., and Sakmann, B. (1997). Regulation of synaptic efficacy by coincidence of postsynaptic aps and epsps. *Science*, 275(5297):213–215.

Markram, H., Muller, E., Ramaswamy, S., Reimann, M. W., Abdellah, M., Sanchez, C. A., Ailamaki, A., Alonso-Nanclares, L., Antille, N., Arsever, S., Kahou, G. A. A., Berger, T. K., Bilgili, A., Buncic, N., Chalimourda, A., Chindemi, G., Courcol, J.-D. D., Delalondre, F., Delattre, V., Druckmann, S., Dumusc, R., Dynes, J., Eilemann, S., Gal, E., Gevaert, M. E., Ghobril, J.-P. P., Gidon, A., Graham, J. W., Gupta, A., Haenel, V., Hay, E., Heinis, T., Hernando, J. B., Hines, M., Kanari, L., Keller, D., Kenyon, J., Khazen, G., Kim, Y., King, J. G., Kisvarday, Z., Kumbhar, P., Lasserre, S., Le Bé, J.-V., Magalhães, B. R., Merchán-Pérez, A., Meystre, J., Morrice, B. R., Muller, J., Muñoz-Céspedes, A., Muralidhar, S., Muthurasa, K., Nachbaur, D., Newton, T. H., Nolte, M., Ovcharenko, A., Palacios, J., Pastor, L., Perin, R., Ranjan, R., Riachi, I., Rodríguez, J.-R. R., Riquelme, J. L., Rössert, C., Sfyrakis, K., Shi, Y., Shillcock, J. C., Silberberg, G., Silva, R., Tauheed, F., Telefont, M., Toledo-Rodriguez, M., Tränkler, T., Van Geit, W., Díaz, J. V., Walker, R., Wang, Y., Zaninetta, S. M., Defelipe, J., Hill, S. L., Segev, I., Schürmann, F., Le Bé, J. V., Magalhães, B. R., Merchán-Pérez, A., Meystre, J., Morrice, B. R., Muller, J., Muñoz-Céspedes, A., Muralidhar, S., Muthurasa, K., Nachbaur, D., Newton, T. H., Nolte, M., Ovcharenko, A., Palacios, J., Pastor, L., Perin, R., Ranjan, R., Riachi, I., Rodríguez, J.-R. R., Riquelme, J. L., Rössert, C., Sfyrakis, K., Shi, Y., Shillcock, J. C., Silberberg, G., Silva, R., Tauheed, F., Telefont, M., Toledo-Rodriguez, M., Tränkler, T., Van Geit, W., Díaz, J. V., Walker, R., Wang, Y., Zaninetta, S. M., Defelipe, J., Hill, S. L., Segev, I., and Schürmann, F. (2015). Reconstruction and Simulation of Neocortical Microcircuitry. *Cell*, 163(2):456–492.

Mattia, M. and Sanchez-Vives, M. V. (2012). Exploring the spectrum of dynamical regimes and timescales in spontaneous cortical activity. *Cogn. Neurodyn.*, 6(3):239–250.

McCormick, D. A., Connors, B. W., Lighthall, J. W., and Prince, D. A. (1985). Comparative electrophysiology of pyramidal and sparsely spiny stellate neurons of the neocortex. *J. Neurophysiol.*, 54(4):782–806.

McDougal, R. A., Bulanova, A. S., and Lytton, W. W. (2016). Reproducibility in Computational Neuroscience Models and Simulations. *IEEE Trans. Biomed. Eng.*, 63(10):2021–2035.

McDougal, R. A., Morse, T. M., Carnevale, T., Marenco, L., Wang, R., Migliore, M., Miller, P. L., Shepherd, G. M., and Hines, M. L. (2017). Twenty years of modeldb and beyond: building essential modeling tools for the future of neuroscience. *J. Comput. Neurosci.*, 42(1):1–10.

Meunier, D., Lambiotte, R., and Bullmore, E. T. (2010). Modular and hierarchically modular organization of brain networks. *Front. Neurosci.*, 4.

Michalareas, G., Vezoli, J., van Pelt, S., Schoffelen, J.-M., Kennedy, H., and Fries, P. (2016). Alpha-Beta and Gamma Rhythms Subserve Feedback and Feedforward Influences among Human Visual Cortical Areas. *Neuron*, 89(2):384–397.

Miłkowski, M., Hensel, W. M., and Hohol, M. (2018). Replicability or reproducibility? On the replication crisis in computational neuroscience and sharing only relevant detail. *J. Comput. Neurosci.*, 45(3):163–172.

Mitra, P. P. and Pesaran, B. (1999). Analysis of dynamic brain imaging data. *Biophys. J.*, 76(2):691–708.

Morrison, A., Diesmann, M., and Gerstner, W. (2008). Phenomenological models of synaptic plasticity based on spike timing. *Biol. Cybern.*, 98(6):459–478.

Mountcastle, V. B. (1997). The columnar organization of the neocortex. *Brain*, 120(4):701–722.

Mukherjee, P. and Kaplan, E. (1995). Dynamics of neurons in the cat lateral geniculate nucleus: In vivo electrophysiology and computational modeling. *J. Neurophysiol.*, 74(3):1222–1243.

Muller, E., Bednar, J. A., Diesmann, M., Gewaltig, M.-O., Hines, M., and Davison, A. P. (2015). Python in neuroscience. *Front. Neuroinform.*, 9:11.

Muller, L., Chavane, F., Reynolds, J., and Sejnowski, T. J. (2018). Cortical travelling waves: mechanisms and computational principles. *Nat. Rev. Neurosci.*, 19(5):255.

Naud, R., Marcille, N., Clopath, C., and Gerstner, W. (2008). Firing patterns in the adaptive exponential integrate-and-fire model. *Biol. Cybern.*, 99(4-5):335–347.

Newman, M. E. J. (2010). *Networks: An Introduction.* Oxford University Press, New York, UK.

Newman, M. E. J. and Barkema, G. T. (1999). *Monte Carlo Methods in Statistical Physics.* Oxford University Press, New York, UK.

Nieuwenhuys, R. (1994). The neocortex - An overview of its evolutionary development, structural organization and synaptology. *Anat. Embryol. (Berl).*, 190(4):307–337.

Nordlie, E., Gewaltig, M. O., and Plesser, H. E. (2009). Towards reproducible descriptions of neuronal network models. *PLoS Comput. Biol.*, 5:e1000456.

Nowak, L. G., Azouz, R., Sanchez-vives, M. V., Gray, C. M., Cormick, D. A. M. C., Lionel, G., Electrophysiolog, D. A. M., and McCormick, D. A. (2003). Electrophysiological Classes of Cat Primary Visual Cortical Neurons In Vivo as Revealed by Quantitative Analyses. *J. Neurophysiol.*, 89(3):1541–1566.

Ódor, G. (2004). Universality classes in nonequilibrium lattice systems. *Rev. Mod. Phys.*, 76(3):663–724.

Ostojic, S. (2014). Two types of asynchronous activity in networks of excitatory and inhibitory spiking neurons. *Nat. Neurosci. 2014 174*, 17(4):594–600.

Papadimitriou, C. H., Vempala, S. S., Mitropolsky, D., Collins, M., and Maass, W. (2020). Brain computation by assemblies of neurons. *P. Natl. Acad. Sci. USA.*

Pape, H.-C. and McCormick, D. (1995). Electrophysiological and pharmacological properties of interneurons in the cat dorsal lateral geniculate nucleus. *Neuroscience*, 68(4):1105–1125.

Parga, N. and Abbott, L. F. (2007). Network Model of Spontaneous Activity Exhibiting Synchronous Transitions Between Up and Down States. *Front. Neurosci.*, 1(1):57.

Paszke, A., Gross, S., Massa, F., Lerer, A., Bradbury Google, J., Chanan, G., Killeen, T., Lin, Z., Gimelshein, N., Antiga, L., Desmaison, A., Xamla, A. K., Yang, E., Devito, Z., Raison Nabla, M., Tejani, A., Chilamkurthy, S., Ai, Q., Steiner, B., Facebook, L. F., Facebook, J. B., and Chintala, S. (2019). Pytorch: An imperative style, high-performance deep learning library. In *Advances in Neural Information Processing Systems*, pages 8026–8037.

Paxinos, G., Huang, X.-F., and Toga, A. W. (2000). *The Rhesus Monkey Brain in Stereotaxic Coordinates.* Academic Press, San Diego, CA.

Pedregosa Gael Varoquaux Alexandre Gramfort Vincent Michel Bertrand Thirion, F., Grisel, O., Blondel Mathieu, Prettenhofer, P., Weiss, R., Dubourg, V., Vanderplas, J., Passos, A., Cournapeau, D., Brucher, M., and Perrot Edouard Duchesnay, M. (2011). Scikit-learn: Machine learning in python. *J. Mach. Learn. Res.*, 12:2825–2830.

Pena, R. F., Ceballos, C. C., Lima, V., and Roque, A. C. (2018a). Interplay of activation kinetics and the derivative conductance determines resonance properties of neurons. *Phys. Rev. E*, 97(4):042408.

Pena, R. F. O., Lima, V., O. Shimoura, R., Paulo Novato, J., and Roque, A. C. (2020). Optimal Interplay between Synaptic Strengths and Network Structure Enhances Activity Fluctuations and Information Propagation in Hierarchical Modular Networks. *Brain Sci.*, 10(4):228.

Pena, R. F. O., Zaks, M. A., and Roque, A. C. (2018b). Dynamics of spontaneous activity in random networks with multiple neuron subtypes and synaptic noise. *J. Comput. Neurosci.*, 45(1):1–28.

Percival, D. B. and Walden, A. T. (1993). *Spectral Analysis for Physical Applications.* Cambridge University Press.

Peyser, A. and Schenck, W. (2015). The nest neuronal network simulator: Performance optimization techniques for high performance computing platforms. In *Posters Presented at the Society for Neuroscience Annual Meeting.*

Peyser, A., Sinha, A., Vennemo, S. B., Ippen, T., Jordan, J., Graber, S., Morrison, A., Trensch, G., Fardet, T., Mørk, H., Hahne, J., Schuecker, J., Schmidt, M., Kunkel, S., Dahmen, D., Eppler, J. M., Diaz, S., Terhorst, D., Deepu, R., Weidel, P., Kitayama, I., Mahmoudian, S., Kappel, D., Schulze, M., Appukuttan, S., Schumann, T., Tunç, H. C., Mitchell, J., Hoff, M., Müller, E., Carvalho, M. M., Zajzon, B., and Plesser, H. E. (2017). NEST 2.14.0.

Plenz, D. and Aertsen, A. (1996). Neural dynamics in cortex-striatum co-cultures—II. Spatiotemporal characteristics of neuronal activity. *Neuroscience*, 70(4):893–924.

Plesser, H. E., Eppler, J. M., Morrison, A., Diesmann, M., and Gewaltig, M.-O. (2007). Efficient parallel simulation of large-scale neuronal networks on clusters of multiprocessor computers. In *European Conference on Parallel Processing*, pages 672–681. Springer.

Plotnikov, D., Rumpe, B., Blundell, I., Ippen, T., Eppler, J. M., and Morrison, A. (2016). Nestml: a modeling language for spiking neurons. *arXiv preprint arXiv:1606.02882*.

Potjans, T. C. and Diesmann, M. (2014). The cell-type specific cortical microcircuit: Relating structure and activity in a full-scale spiking network model. *Cereb. Cortex*, 24(3):785–806.

Rabinowitch, I. (2019). What would a synthetic connectome look like? *Phys. Life Rev.*

Radnikow, G. and Feldmeyer, D. (2018). Layer- and Cell Type-Specific Modulation of Excitatory Neuronal Activity in the Neocortex. *Front. Neuroanat.*, 12:1.

Ray, S., Deshpande, R., Dudani, N., and Bhalla, U. S. (2008). A general biological simulator: the multiscale object oriented simulation environment, MOOSE. *BMC Neurosci.*, 9(Suppl 1):P93.

Renart, A., de la Rocha, J., Bartho, P., Hollender, L., Parga, N., Reyes, A., and Harris, K. D. (2010). The Asynchronous State in Cortical Circuits. *Science (80-.)*., 327(5965):587–590.

Rennie, C. J., Robinson, P. A., and Wright, J. J. (2002). Unified neurophysical model of EEG spectra and evoked potentials. *Biol. Cybern.*, 86(6):457–471.

Ringach, D. L. (2009). Spontaneous and driven cortical activity: implications for computation. *Curr. Opin. Neurobiol.*, 19(4):439–444.

Roberts, J. A. and Robinson, P. A. (2008). Modeling absence seizure dynamics: implications for basic mechanisms and measurement of thalamocortical and corticothalamic latencies. *J. Theor. Biol.*, 253(1):189–201.

Robinson, P. A., Loxley, P. N., O'Connor, S. C., and Rennie, C. J. (2001a). Modal analysis of corticothalamic dynamics, electroencephalographic spectra, and evoked potentials. *Phys. Rev. E*, 63(4):041909.

Robinson, P. A., Rennie, C. J., and Rowe, D. L. (2002). Dynamics of large-scale brain activity in normal arousal states and epileptic seizures. *Phys. Rev. E*, 65(4):41924.

Robinson, P. A., Rennie, C. J., Wright, J. J., Bahramali, H., Gordon, E., and Rowe, D. L. (2001b). Prediction of electroencephalographic spectra from neurophysiology. *Phys. Rev. E*, 63(021903):021903.

Robitaille, T. P., Tollerud, E. J., Greenfield, P., Droettboom, M., Bray, E., Aldcroft, T., Davis, M., Ginsburg, A., Price-Whelan, A. M., Kerzendorf, W. E., Conley, A., Crighton, N., Barbary, K., Muna, D., Ferguson, H., Grollier, F., Parikh, M. M., Nair, P. H., Günther, H. M., Deil, C., Woillez, J., Conseil, S., Kramer, R., Turner, J. E., Singer, L., Fox, R., Weaver, B. A., Zabalza, V., Edwards, Z. I., Azalee Bostroem, K., Burke, D. J., Casey, A. R., Crawford, S. M., Dencheva, N., Ely, J., Jenness, T., Labrie, K., Lim, P. L., Pierfederici, F., Pontzen, A., Ptak, A., Refsdal, B., Servillat, M., and Streicher, O. (2013). Astropy: A community python package for astronomy. *Astron. Astrophys.*, 558:A33.

Rodriguez, R., Kallenbach, U., Singer, W., and Munk, M. H. J. (2004). Short- and long-term effects of cholinergic modulation on gamma oscillations and response synchronization in the visual cortex. *J. Neurosci.*, 24(46):10369–78.

Roth, A. and van Rossum, C. W. (2010). Modeling synapses. In De Schutter, E., editor, *Computational Modeling Methods for Neuroscientists*, pages 139–159. The MIT Press, Cambridge, MA.

Rougier, N. P., Hinsen, K., Alexandre, F., Arildsen, T., Barba, L. A., C.Y.Benureau, A., Brown, C. T., DeBuy, P., Caglayan, O., Davison, A. P., Delsuc, M. A., Detorakis, G., Diem, A. K., Drix, D., Enel, P., Girard, B., Guest, O., Hall, M. G., Henriques, R. N., Hinaut, X., Jaron, K. S., Khamassi, M., Klein, A., Manninen, T., Marchesi, P., McGlinn, D., Metzner, C., Petchey, O., Plesser, H. E., Poisot, T., Ram, K., Ram, Y., Roesch, E., Rossant, C., Rostami, V., Shifman, A., Stachelek, J., Stimberg, M., Stollmeier, F., Vaggi, F., Viejo, G., Vitay, J., Vostinar, A. E., Yurchak, R., and Zito, T. (2017). Sustainable computational science: the rescience initiative. *PeerJ Comput. Sci.*, 3:e142.

Roxin, A., Riecke, H., and Solla, S. A. (2004). Self-sustained activity in a small-world network of excitable neurons. *Phys. Rev. Lett*, 92(19):198101.

Saalmann, Y. B., Pinsk, M. A., Wang, L., Li, X., and Kastner, S. (2012). The pulvinar regulates information transmission between cortical areas based on attention demands. *Science*, 337(6095):753–756.

Safari, M.-S., Mirnajafi-Zadeh, J., Hioki, H., and Tsumoto, T. (2017). Parvalbumin-expressing interneurons can act solo while somatostatin-expressing interneurons act in chorus in most cases on cortical pyramidal cells. *Sci. Rep.*, 7(1):1–14.

Saleeba, C., Dempsey, B., Le, S., Goodchild, A., and McMullan, S. (2019). A student's guide to neural circuit tracing. *Front. Neurosci.*, 13:897.

Sanchez-Vives, M. V. and McCormick, D. A. (2000). Cellular and network mechanisms of rhythmic recurrent activity in neocortex. *Nat. Neurosci. 2000 310*, 3(10):1027–1034.

Schiff, M. L. and Reyes, A. D. (2012). Characterization of thalamocortical responses of regular-spiking and fast-spiking neurons of the mouse auditory cortex in vitro and in silico. *J. Neurophysiol.*, 107(5):1476–1488.

Schmidt, M., Bakker, R., Hilgetag, C. C., Diesmann, M., and van Albada, S. J. (2018a). Multi-scale account of the network structure of macaque visual cortex. *Brain Struct. Funct.*, 223(3):1409–1435.

Schmidt, M., Bakker, R., Shen, K., Bezgin, G., Diesmann, M., and van Albada, S. J. (2018b). A multi-scale layer-resolved spiking network model of resting-state dynamics in macaque visual cortical areas. *PLOS Comput. Biol.*, 14(10):e1006359.

Schurger, A., Sitt, J. D., and Dehaene, S. (2012). An accumulator model for spontaneous neural activity prior to self-initiated movement. *Proc. Natl. Acad. Sci.*, 109(42):E2904–E2913.

Sedigh-Sarvestani, M., Vigeland, L., Fernandez-Lamo, I., Taylor, M. M., Palmer, L. A., and Contreras, D. (2017). Intracellular, In Vivo, Dynamics of Thalamocortical Synapses in Visual Cortex. *J. Neurosci.*, 37(21):5250–5262.

Segev, I. and Burke, R. E. (1998). Compartmental models of complex neurons. In Koch, C. and Segev, I., editors, *Methods in Neuronal Modeling: From Ions to Networks, 2nd. Edition*, pages 93–136. The MIT Press Press, Cambridge, MA.

Serkov, F. N. and Gonchar, Y. A. (1995). Quantitative parameters of synaptic apparatus in the ventral nucleus of the medial geniculate body of the cat. *Neurophysiology*, 27(3):164–174.

Seth, A. (2007). Granger causality. *Scholarpedia*, 2(7):1667.

Shen, F. Y., Harrington, M. M., Walker, L. A., Cheng, H. P. J., Boyden, E. S., and Cai, D. (2020). Light microscopy based approach for mapping connectivity with molecular specificity. *Nat. Commun.*, 11:4632.

Shepherd, G. M. and Grillner, S., editors (2018). *Handbook of Brain Microcircuits, Second edition.* Oxford University Press, New York, NY, USA.

Shepherd, G. M. and Rowe, T. B. (2017). Neocortical lamination: insights from neuron types and evolutionary precursors. *Front. Neuroanat.*, 11:100.

Sherman, S. (2006). Thalamus. *Scholarpedia*, 1(9):1583.

Sherman, S. M. and Guillery, R. W. (2011). Distinct functions for direct and transthalamic corticocortical connections. *J. Neurophysiol.*, 106(3):1068–1077.

Shimoura, R. O., Kamiji, N. L., Pena, R. F. O., Cordeiro, V. L., Ceballos, C. C., Cecilia, R., and Roque, A. C. (2018). [Re] The cell-type specific cortical microcircuit: relating structure and activity in a full-scale spiking network model. *Zenodo*.

Shimoura, R. O., Pena, R. F. O., Kamiji, N. L., Lima, V., and Roque, A. C. (2021). Modelos de redes de neurônios para o neocórtex e fenômenos emergentes observados. *Rev. Bras. Ensino Física*, 43(suppl 1).

Shimoura, R. O., Pena, R. F. O., and Roque, A. C. (2015). Effect of synaptic plasticity on functional connectivity and global activity of a neocortical network model. *BMC Neurosci.*

Shinomoto, S., Miura, K., and Koyama, S. (2005). A measure of local variation of inter-spike intervals. In *BioSystems*, volume 79, pages 67–72.

Shinomoto, S., Shima, K., and Tanji, J. (2003). Differences in Spiking Patterns among Cortical Neurons. *Neural Comput.*, 15(12):2823–2842.

Shu, Y., Hasenstaub, A., and McCormick, D. A. (2003). Turning on and off recurrent balanced cortical activity. *Nat. 2003 4236937*, 423(6937):288–293.

Silva, L., Amitai, Y., and Connors, B. (1991). Intrinsic oscillations of neocortex generated by layer 5 pyramidal neurons. *Science (80-.).*, 251(4992):432–435.

Sitt, J. D., King, J. R., El Karoui, I., Rohaut, B., Faugeras, F., Gramfort, A., Cohen, L., Sigman, M., Dehaene, S., and Naccache, L. (2014). Large scale screening of neural signatures of consciousness in patients in a vegetative or minimally conscious state. *Brain*, 137(8):2258–2270.

Sjöström, J. and Gerstner, W. (2010). Spike-timing dependent plasticity. *Scholarpedia*, 5:1362.

Sjöström, P. J., Turrigiano, G. G., and Nelson, S. B. (2001). Rate, timing, and cooperativity jointly determine cortical synaptic plasticity. *Neuron*, 32(6):1149–1164.

Slepian, D. (1978). Prolate Spheroidal Wave Functions, Fourier Analysis, and Uncertainty—V: The Discrete Case. *Bell Syst. Tech. J.*, 57(5):1371–1430.

Slepian, D. and Pollak, H. O. (1961). Prolate Spheroidal Wave Functions, Fourier Analysis and Uncertainty — I. *Bell Syst. Tech. J.*, 40(1):43–63.

Spaak, E., Zeitler, M., and Gielen, S. (2012). Hippocampal Theta Modulation of Neocortical Spike Times and Gamma Rhythm: A Biophysical Model Study. *PLoS One*, 7(10):e45688.

Sporns, O. (2010). *Networks of the Brain.* MIT press, Cambridge, MA.

Sporns, O. (2011). The human connectome: a complex network. *Ann. NY Acad. Sci.*, 1224(1):109–125.

Sporns, O., Tononi, G., and Kötter, R. (2005). The human connectome: a structural description of the human brain. *PLoS Comput. Biol.*, 1(4):e42.

Staba, R. J. and Bragin, A. (2011). High-frequency oscillations and other electrophysiological biomarkers of epilepsy: underlying mechanisms. *Biomark. Med.*, 5(5):545–556.

Stephan, K. E. (2013). The history of cocomac. *NeuroImage*, 80:46–52.

Steriade, M., Amzica, F., and Nuñez, A. (1993). Cholinergic and noradrenergic modulation of the slow (approximately 0.3 Hz) oscillation in neocortical cells. *J. Neurophysiol.*, 70(4):1385–400.

Steriade, M., Gloor, P., Llinás, R., Lopes da Silva, F., and Mesulam, M.-M. (1990). Basic mechanisms of cerebral rhythmic activities. *Electroencephalogr. Clin. Neurophysiol.*, 76(6):481–508.

Steriade, M., Timofeev, I., and Grenier, F. (2001). Natural Waking and Sleep States: A View From Inside Neocortical Neurons. *J. Neurophysiol.*, 85(5):1969–1985.

Sterratt, D., Graham, B., Gillies, A., and Willshaw, D. (2012). *Principles of Computational Modelling in Neuroscience.* Cambridge University Press.

Stimberg, M., Brette, R., and Goodman, D. F. (2019). Brian 2, an intuitive and efficient neural simulator. *Elife*, 8:e47314.

Stockley, E., Cole, H., Brown, A., and Wheal, H. (1993). A system for quantitative morphological measurement and electrotonic modelling of neurons: three-dimensional reconstruction. *J. Neurosci. Meth.*, 47(1-2):39–51.

Stoelzel, C. R., Bereshpolova, Y., Gusev, A. G., and Swadlow, H. A. (2008). The impact of an LGNd impulse on the awake visual cortex: synaptic dynamics and the sustained/transient distinction. *J. Neurosci.*, 28(19):5018–28.

Stratford, K. J., Tarczy-Hornoch, K., Martin, K. A. C., Bannister, N. J., and Jack, J. J. B. (1996). Excitatory synaptic inputs to spiny stellate cells in cat visual cortex. *Nature*, 382(6588):258–261.

Stringer, C., Pachitariu, M., Steinmetz, N., Reddy, C. B., Carandini, M., and Harris, K. D. (2019). Spontaneous behaviors drive multidimensional, brainwide activity. *Science (80-.).*, 364(6437).

Sun, W. and Dan, Y. (2009). Layer-specific network oscillation and spatiotemporal receptive field in the visual cortex. *Proc. Natl. Acad. Sci. U. S. A.*, 106(42):17986–91.

Supp, G. G., Siegel, M., Hipp, J. F., and Engel, A. K. (2011). Cortical hypersynchrony predicts breakdown of sensory processing during loss of consciousness. *Curr. Biol.*, 21(23):1988–1993.

Swadlow, H. A. and Weyand, T. G. (1985). Receptive-field and axonal properties of neurons in the dorsal lateral geniculate nucleus of awake unparalyzed rabbits. *J. Neurophysiol.*, 54(1):168–83.

Swadlow, H. A. and Weyand, T. G. (1987). Corticogeniculate neurons, corticotectal neurons, and suspected interneurons in visual cortex of awake rabbits:

receptive-field properties, axonal properties, and effects of EEG arousal. *J. Neurophysiol.*, 57(4):977–1001.

Thomson, A. M., West, D. C., Wang, Y., and Bannister, A. P. (2002). Synaptic connections and small circuits involving excitatory and inhibitory neurons in layers 2–5 of adult rat and cat neocortex: triple intracellular recordings and biocytin labelling in vitro. *Cereb. Cortex*, 12(9):936–953.

Thomson, D. (1982). Spectrum estimation and harmonic analysis. *Proc. IEEE*, 70(9):1055–1096.

Tibau, E., Bendiksen, C., Teller, S., Amigó, N., and Soriano, J. (2013). Interplay activity-connectivity: Dynamics in patterned neuronal cultures. *AIP Conf. Proc.*, 1510(1):54–63.

Tikidji-Hamburyan, R. A., Narayana, V., Bozkus, Z., and El-Ghazawi, T. A. (2017). Software for brain network simulations: a comparative study. *Front. Neuroinform.*, 11:46.

Timofeev, I., Grenier, F., Bazhenov, M., Sejnowski, T. J., and Steriade, M. (2000). Origin of slow cortical oscillations in deafferented cortical slabs. *Cereb. Cortex*, 10(12):1185–99.

Tomov, P., Pena, R. F., Roque, A. C., and Zaks, M. A. (2016a). Mechanisms of self-sustained oscillatory states in hierarchical modular networks with mixtures of electrophysiological cell types. *Front. Comput. Neurosci.*, 10:23.

Tomov, P., Pena, R. F., Zaks, M. A., and Roque, A. C. (2014a). Sustained oscillations, irregular firing, and chaotic dynamics in hierarchical modular networks with mixtures of electrophysiological cell types. *Front. Comput. Neurosci.*, 8:103.

Tomov, P., Pena, R. F. O., Roque, A. C., and Zaks, M. A. (2016b). Mechanisms of Self-Sustained Oscillatory States in Hierarchical Modular Networks with Mixtures of Electrophysiological Cell Types. *Front. Comput. Neurosci.*, 10:23.

Tomov, P., Pena, R. F. O., Zaks, M. A., and Roque, A. C. (2014b). Sustained oscillations, irregular firing, and chaotic dynamics in hierarchical modular networks with mixtures of electrophysiological cell types. *Front. Comput. Neurosci.*, 8:103.

Tononi, G., Edelman, G. M., and Sporns, O. (1998). Complexity and coherency: Integrating information in the brain.

Tononi, G., Sporns, O., and Edelman, G. M. (1994). A measure for brain complexity: Relating functional segregation and integration in the nervous system. *Proc. Natl. Acad. Sci. U. S. A.*, 91(11):5033–5037.

Traub, R. D., Contreras, D., Cunningham, M. O., Murray, H., LeBeau, F. E., Roopun, A., Bibbig, A., Wilent, W. B., Higley, M. J., and Whittington, M. A. (2004). Single-Column Thalamocortical Network Model Exhibiting Gamma Oscillations, Sleep Spindles, and Epileptogenic Bursts. *J. Neurophysiol.*, 93(4):2194–2232.

Traub, R. D., Hawkins, K., Adams, N. E., Hall, S. P., Simon, A., and Whittington, M. A. (2020). Layer 4 pyramidal neuron dendritic bursting underlies a post-stimulus visual cortical alpha rhythm. *Commun. Biol.*, 3(1):1–13.

Tremblay, R., Lee, S., and Rudy, B. (2016). GABAergic Interneurons in the Neocortex: From Cellular Properties to Circuits. *Neuron*, 91(2):260–292.

Tsodyks, M. (2005). Course 7 - activity-dependent transmission in neocortical synapses. In Chow, C., Gutkin, B., Hansel, D., Meunier, C., and Dalibard, J., editors, *Methods and Models in Neurophysics*, volume 80 of *Les Houches*, pages 245 – 265. Elsevier.

Tsodyks, M., Pawelzik, K., and Markram, H. (1998). Neural networks with dynamic synapses. *Neural Comput.*, 10:821.

Tsuno, Y., Schultheiss, N. W., and Hasselmo, M. E. (2013). In vivo cholinergic modulation of the cellular properties of medial entorhinal cortex neurons. *J. Physiol.*, 591(10):2611–2627.

Uenke, M. h. l. S., Schulte, E., and Umacher, U. S. h. (2010). *THIEME Atlas of Anatomy. Head and Neuroanatomy.* Thieme.

van Albada, S., Kerr, C., Chiang, A., Rennie, C., and Robinson, P. (2010). Neurophysiological changes with age probed by inverse modeling of EEG spectra. *Clin. Neurophysiol.*, 121(1):21–38.

van Albada, S. J., Helias, M., and Diesmann, M. (2015). Scalability of Asynchronous Networks Is Limited by One-to-One Mapping between Effective Connectivity and Correlations. *PLOS Comput. Biol.*, 11(9):e1004490.

van Albada, S. J., Morales-Gregorio, A., Dickscheid, T., Goulas, A., Bakker, R., Bludau, S., Palm, G., Hilgetag, C.-C., and Diesmann, M. (2020). Bringing Anatomical Information into Neuronal Network Models.

van Albada, S. J. and Robinson, P. A. (2009). Mean-field modeling of the basal ganglia-thalamocortical system. I. Firing rates in healthy and parkinsonian states. *J. Theor. Biol.*, 257(4):642–663.

van Albada, S. J. and Robinson, P. A. (2013). Relationships between electroencephalographic spectral peaks across frequency bands. *Front. Hum. Neurosci.*, 7(56):56.

van Kerkoerle, T., Self, M. W., Dagnino, B., Gariel-Mathis, M.-A., Poort, J., van der Togt, C., and Roelfsema, P. R. (2014). Alpha and gamma oscillations characterize feedback and feedforward processing in monkey visual cortex. *Proc. Natl. Acad. Sci. U. S. A.*, 111(40):14332–41.

Van Strien, N., Cappaert, N., and Witter, M. (2009). The anatomy of memory: an interactive overview of the parahippocampal–hippocampal network. *Nat. Rev. Neurosci.*, 10(4):272–282.

Van Vreeswijk, C. and Sompolinsky, H. (1996). Chaos in neuronal networks with balanced excitatory and inhibitory activity. *Science (80-.).*, 274(5293):1724–1726.

Van Vreeswijk, C. and Sompolinsky, H. (1998). Chaotic Balanced State in a Model of Cortical Circuits. *Neural Comput.*, 10(6):1321–1371.

Vogels, T. P. and Abbott, L. F. (2005). Signal propagation and logic gating in networks of integrate-and-fire neurons. *J. Neurosci.*, 25(46):10786–10795.

Vogels, T. P., Rajan, K., and Abbott, L. (2005). NEURAL NETWORK DYNAMICS. *Annu. Rev. Neurosci.*, 28(1):357–376.

Wagenaar, D. A., Pine, J., and Potter, S. M. (2006). An extremely rich repertoire of bursting patterns during the development of cortical cultures. *BMC Neurosci. 2006 71*, 7(1):1–18.

Walter, W. G. (1963). *The living brain.* W. W. Norton.

Wang (2011). Sustained activity in hierarchical modular neural networks: self-organized criticality and oscillations. *Front. Comput. Neurosci.*, 5.

Wang, Q., Ding, S. L., Li, Y., Royall, J., Feng, D., Lesnar, P., Graddis, N., Naeemi, M., Facer, B., Ho, A., Dolbeare, T., Blanchard, B., Dee, N., Wakeman, W., Hirokawa, K. E., Szafer, A., Sunkin, S. M., Oh, S. W., Bernard, A., Phillips, J. W., Hawrylycz, M., Koch, C., Zeng, H., Harris, J. A., and Ng, L. (2020). The Allen mouse brain common coordinate framework: a 3D reference atlas. *Cell*, 181:936–953.e20.

Watts, D. J. and Strogatz, S. H. (1998). Collective dynamics of ‘small-world’networks. *Nature*, 393(6684):440–442.

Whittington, M. A., Traub, R. D., Kopell, N., Ermentrout, B., and Buhl, E. H. (2000). Inhibition-based rhythms: Experimental and mathematical observations on network dynamics. In *Int. J. Psychophysiol.*, volume 38, pages 315–336. Elsevier.

Wilson, G. (1978). A convergence theorem for spectral factorization. *J. Multivar. Anal.*, 8(2):222–232.

Wilson, G. T. (1972). The Factorization of Matricial Spectral Densities. *SIAM J. Appl. Math.*, 23(4):420–426.

Witter, M. P. (2010). Connectivity of the hippocampus. In *Hippocampal Microcircuits*, pages 5–26. Springer.

Wolfart, J., Debay, D., Le Masson, G., Destexhe, A., and Bal, T. (2005). Synaptic background activity controls spike transfer from thalamus to cortex. *Nat. Neurosci.*, 8(12):1760–1767.

Worrell, G. and Gotman, J. (2011). High-frequency oscillations and other electrophysiological biomarkers of epilepsy: clinical studies. *Biomark. Med.*, 5(5):557–566.

Yamaguchi, I., Kishi, A., Togo, F., Nakamura, T., and Yamamoto, Y. (2018). A Robust Method with High Time Resolution for Estimating the Cortico-Thalamo-Cortical Loop Strength and the Delay when Using a Scalp Electroencephalography Applied to the Wake-Sleep Transition. *Methods Inf. Med.*, 57(03):122–128.

Yamamoto, H., Moriya, S., Ide, K., Hayakawa, T., Akima, H., Sato, S., Kubota, S., Tanii, T., Niwano, M., Teller, S., Soriano, J., and Hirano-Iwata, A. (2018). Impact of modular organization on dynamical richness in cortical networks. *Sci. Adv.*, 4(11):eaau4914.